Studies on ZnS & TiO_2 nanomaterials for high reflective coatings

A THESIS

Submitted to the

FACULTY OF SCIENCE

THAPAR UNIVERSITY, PATIALA

for the degree of

Doctor of Philosophy

By

SANJEEV KUMAR

Regn. No. 90712005

School of Physics & Materials Science

Thapar University

Patiala - 147 004

INDIA

October 2011

DECLARATION

It is certified that the thesis is entirely my own and that the ideas and references cited herein have been duly acknowledged.

Sanjeev Kumar

Attestation by supervisors

(Dr. N. K. Verma)
Senior Professor
School of Physics and Materials Science,
Thapar University,
Patiala – 147 004
INDIA

(Dr. M. L. Singla)
Ex. Scientist-G
Materials Research Division,
Central Scientific Instruments Organisation,
Chandigarh – 160 030
INDIA

CERTIFICATE

This is to certify that the thesis entitled, "**Studies on ZnS & TiO_2 nanomaterials for high reflective coatings**", submitted by Mr. Sanjeev Kumar in the fulfillment of the requirement for the award of the degree of Doctor of Philosophy in the School of Physics and Materials Science, Thapar University, Patiala, is a record of candidate's own work carried out by him under my supervision and guidance. The matter presented in this thesis has not been submitted in part or full for the award of any degree in any other University or Institute.

Attestation by supervisors

(Dr. N. K. Verma)
Senior Professor
School of Physics and Materials Science,
Thapar University,
Patiala – 147 004
INDIA

(Dr. M. L. Singla)
Ex. Scientist-G
Materials Research Division,
Central Scientific Instruments Organisation,
Chandigarh – 160 030
INDIA

To

My Beloved

Parents

Pals

And

Supervisors

ACKNOWLEDGMENTS

First and foremost, I would like to express my great appreciation to my Supervisor, **Dr. N. K. Verma,** Senior Professor, School of Physics and Materials Science, Thapar University, Patiala, for his outstanding scientific expertise, encouragement and patient hours spent in reviewing my papers and this thesis. I am also greatly indebted to my co-supervisor, **Dr. M. L. Singla,** Ex. Scientist-G, Materials Research Division, Central Scientific Instruments Organisation, Chandigarh, for his kind guidance and technical advice in every aspect of this thesis. My gratitude to them for their invaluable support and guidance during my research work can never be fully expressed.

I, gratefully acknowledge the financial support provided by University Grants Commission **(UGC),** Department of Science and Technology **(DST),** Government of India, respectively for awarding me **JRF** and **INSPIRE** Fellowship. I am also extremely grateful to Thapar University **(TU)**, Patiala, for awarding me **Teaching Associateship** during my research work.

I wish to express my sincere gratitude to **Dr. S. S. Sekhon**, Professor, Guru Nanak Dev University (GNDU), Amritsar, who introduced me to this fascinating world of research and for invaluable guidance.

I am thankful to my PhD committee members**, Dr. Rajeev Mehta**, Associate Professor and Head, Chemical Engineering Department, Thapar University, Patiala and **Dr. S. D. Tiwari**, Assistant Professor, School of Physics and Materials Science, Thapar University, Patiala, for their constructive comments and regularly ensuring the progress of my research work.

I am profoundly obliged to **Dr. K. K. Raina**, Deputy Director, Thapar University, Patiala, **Dr. Kulbir Singh**, Head, School of Physics and Materials

Science, Thapar University, Patiala, **Dr. O. P. Pandey**, Professor, School of Physics and Materials Science, Thapar University, Patiala, and **Dr. Susheel Mittal**, Senior Professor, School of Chemistry and Biochemistry, Thapar University, Patiala, **Dr Bonamali Pal,** School of Chemistry and Biochemistry, Associate Professor, Thapar University, Patiala, for their whole-hearted support, motivation and ever available guidance, which facilitated me for successful completion of this research work. I am also thankful to all the faculty members of School of Physics and Materials for their support.

I also acknowledge the wholehearted support of the technical and secretarial staff of the Department.

I deeply admire the help and support rendered by **Dr. Sunil Kumar**, **Dr. Zinki Jindal, Dr. Karamjit Singh**, and **Dr. Sanjeev Kumar.**

During my research work, I had technical and scientific discussions with my research mates. For which, I am thankful to **Mr. Gurmeet Singh, Miss Lavanya Khanna,** and **Miss Manveen Kaur**, in particular, and **Jaspal Singh, Miss Kamaldeep Kaur Billing** and **Miss Gitanjali Dhir**, in general.

I would like to thank all my well wishers, whose names may not be mentioned here but are deeply acknowledged.

I would like to individually thank my best pals, **Mr. Vineet Kumar, Mr. Rohin Verma, Mr. Anoop Kumar, Mr. Vinod Kumar, Mr. Sunil Kumar, Mr. Yashu Jethi, Miss Mopsy Dhiman, Miss Shivangi** and **Mr. Sandeep Bachan** who have been an indispensable part of my life's journey, providing unmatched support and motivation.

I dedicate this thesis to my loving parents **Sh. Raj Kumar** and **Smt. Roshini Devi**, to whom I owe my life and if it wasn't for their constant support, unconditional love and encouragement, I would not have been what I am today.

Special acknowledgement to my brother **Mr. Pawan Kumar** and my sister in law **Mrs. Anita** for their blessings as well as inspiring me to have greater academic pursuits.

Words cannot express the gratitude to my beloved friend **Miss Rekha Thakur** for her unceasing support, advice and encouragement in all my academic endeavors. She is so completely involved in every part of my life that I do not consider any achievement of mine as personal.

Finally and most importantly, I would like to thank Almighty for His blessings and kindness, a boundless and an endless source of inspiration for me always.

Skumar

Sanjeev Kumar

List of Publications

(a) Papers in refereed journals

1. Kumar S, Verma NK, Singla ML, "Reflective properties of ZnS nanoparticle coatings", Journal of Coating Technology and Research, 8 (2) 223-228 (2011).

2. Kumar S, Verma NK, Singla ML, "Reflective characteristics of Ni doped ZnS nanoparticle-pigment and their coatings", Chalcogenide Letters, 8(9) 561-569 (2011).

3. Kumar S, Verma NK, Singla ML, "Highly reflective titania nanoparticle-based coating", Pigments and Resin Technology, Emerland, 42(3) 2012.

4. Kumar S, Verma NK, Singla ML, "Size dependent reflective properties of TiO_2 nanoparticles and reflectors made thereof", Digest Journal of nanomaterials and biostructures (Accepted).

5. Kumar S, Verma NK, Singla ML, "Effect of visible light on the photostability of Al doped TiO_2 nanoparticles", Bulletin of Materials Science, Indian Academy of Sciences (Communicated).

6. Kumar S, Verma NK, Singla ML, "Diffuse reflectance and reflective flexible coatings of capped ZnS nanoparticles", Materials Chemistry and Physics, Elsevier (Communicated).

(C) Papers in conference proceedings

1. Synthesis of ZnS nanoparticles with Enhanced Diffuse Reflectance, Sanjeev Kumar, N.K. Verma, Proceedings of the **National Conference** on Smart, Electronic & Engineering Materials, organized by Baba Farid College of Engineering & Technology, Bathinda, on March 5-6, 2010, p.56.
2. Synthesis of zinc sulphide nanoparticles pigment and their reflective characteristics, Sanjeev Kumar, M.L. Singla, N.K. Verma, Proceedings of the **International Conference** on Emerging Trends in Mechanical Engineering, organized by Department of Mechanical Engineering, Thapar University, Patiala, on February 24-26, 2011, p.100.
3. Study on reflective characteristics of Titania nanoparticles, Sanjeev Kumar, N.K. Verma M.L. Singla, Proceedings of the **National Seminar** on Advanced Materials and Devices, organized by Department of Physics, GVM Girls College, Sonepat, on July 3-4, 2011, p.38.
4. Reflective coatings incorporating ZnS nanoparticle pigments, Sanjeev Kumar, M.L. Singla, N.K. Verma, Proceedings of the **International Conference** on Advances in Materials & Manufacturing Technology, organized by Department of Mechanical Engineering, Chitkara University, Rajpura, on July 20, 2011, pp.179-182.
5. Synthesis of titania nanoparticles and their application in reflectors, Sanjeev Kumar, Meenu Menon, M.L. Singla, N.K. Verma, Proceedings of the **National Conference** on Nanoscience Fundamentals and Applications, organized by Department of Applied Sciences, Chitkara University, Rajpura, on July 23-24, 2011, p.39.

CONTENTS

List of Tables

List of Figures

Abstract

ZnS and TiO_2 bulk particles are widely employed as reflective pigments. Nanocrystalline materials are very promising materials due to their unique properties such as larger surface to volume ratio and quantum confinement effect, as compared to their bulk counterparts, and are potential candidates for technological application. Therefore we are interested to investigate the properties of ZnS and TiO_2 nanoparticles. In this work, synthesized ZnS and TiO_2 nanoparticles have been explored to develop highly reflecting coatings.

For the syntheses of ZnS and TiO_2 nanoparticles, respectively the chemical precipitation and sol-gel techniques have been used. The structural, morphological and optical properties of the synthesized nanoparticles have been investigated. The techniques used for their characterization include: X-ray diffraction (XRD), Scanning electron microscopy (SEM), Transmission electron microscopy (TEM), Fourier transform infrared (FTIR) spectroscopy, Photoluminescence (PL), UV-visible absorption spectroscopy and UV-visible diffuse reflectance spectroscopy (DRS).

The effect of the molar ratio of the precursors (L), calcination temperature, nature of capping agent and its concentration on the reflective properties of ZnS and TiO_2 nanoparticles have been investigated. Attempts have been made to correlate the reflective characteristics of synthesized nanoparticles with their size, size distribution and morphology.

Highly reflective coatings were developed employing these nanoparticles. Coating materials were prepared using these nanoparticles by optimizing various parameters such as pigment to binder ratio, pH, and pigment to solvent ratio. Reflectors have been developed by applying these coating materials separately to aluminium and plastic substrates with different coating thicknesses and different pigment to binder ratios.

The reflectors were also exposed to different light illuminations and temperatures to check their durability.

Chapter 1

Introduction

The ever-increasing need for more specialized materials continuously pushes the envelope of modern technology, equipment and human intellect. Precise control on the size, physical, chemical, and electronic properties of materials can allow us to harness their applications in diverse fields. This chapter deals with brief and selective history of the nanomaterials and their applications. It is also imperative to introduce one of the applications of nanomaterials, i.e., reflective coatings, on which the whole thesis work is based.

1.1 Nanotechnology

Nanotechnology is the study, design, creation, synthesis, manipulation, and application of functional materials, devices, and systems through control of matter at the nanometer scale (1-100 nm) [1]. It also includes the fundamental understanding of the relationships between physical properties and material's dimension. It is an emerging interdisciplinary technology that has been booming in many areas during the recent decade, including materials science, mechanics, electronics, optics, biology, electronics, aerospace etc. Upon its complete realization, it's going to change the way we see things. It is an enabling technology that offers the potential for unprecedented advances in many diverse fields [2-5]. This technology makes it possible to manipulate matter at the atomic or molecular scale to form new materials, structures and devices that exploit the unique physical and chemical properties associated with nanometer-scale structures. The promise

of nanotechnology goes far beyond extending the use of current materials. New materials and devices with intricate and closely engineered structures will allow for new directions in optics, electronics, and optoelectronics [6-8], development of new medical imaging and treatment technologies [9, 10], and production of advanced materials with unique properties and high-efficiency energy storage and generation [11, 12].

1.2 Nanometer and nanoscale

A nanometer equals to one billionth (10^{-9}) of a meter, approximately 80,000 times smaller than the diameter of an average human hair and ten times the diameter of the hydrogen atom. The prefix 'nano' is derived from the Greek word nannos, meaning "very short man" but means something broader [13]. Nanoscale refers to anything which has the characteristic size from 1 to 100 nm. This range corresponds to the atomic or molecular domain. This is the scale at which nanotechnologists work.

1.3 Nanomaterials

Nanomaterials are the materials that possess structured components with one, two or three dimensions in the nanoscale region (1 – 100 nm). Nanomaterials are the simplest type of nanoproduct. Nanomaterials are at the leading edge of the rapidly developing field of nanotechnology. Their unique size-dependent properties make these materials superior and indispensable in many areas of human activity. Nanomaterials are of great interest due to their extremely small size and large surface-to-volume ratio, which lead to both chemical and physical differences in their properties as compared to the bulk material of same chemical composition. Nanomaterials include nanopowders, nanotubes, nanowires, nanocoatings, and so on.

Nanomaterials can be characterized, on the basis of the number of dimensions confined to the nanoscale (1 -100 nm) as follows:

1. In 2-D nanostructures, one of the three dimensions lies in the nanoscale, examples include: interfaces, membranes, thin films, multi-layers.
2. In 1-D nanostructures, two of the three dimensions lie in the nanoscale, examples include, nanowires, nanotubes, DNA.
3. In 0-D nanostructures, all the three dimensions lie in the nanoscale, examples include, nanoparticles, quantum dots.

1.4 Fabrication of nanomaterials

Fabrication techniques fall into two categories:

1. **Top down** - Essentially, one starts with a larger piece of material and etches, mills or machines a structure from it by removing the material. Examples include: lithography, milling.
2. **Bottom up -** This involves building up of structures atom-by-atom or molecule-by molecule. Examples include: chemical synthesis, self-assembly, positional assembly.

1.5 Applications of nanotechnology

Research and applications in the field of nanotechnology have been growing rapidly worldwide for the past decade, with an increasing number of nanotechnology products becoming commercially available. These include nanoscale materials, powders, composite materials, nanostructured devices, paints, reflective coatings, solutions and suspensions of nanoscale materials [14-16]. Nanotechnology is being used to reduce the cost of catalysts used in fuel cells to produce hydrogen ions from fuel such as methanol [17]. Researchers are developing customized nanoparticles which can deliver drugs directly to diseased cells in the body [17]. Nanotechnology can enable sensors to detect very small amounts of chemical vapors, biological entities, gases [18]. Companies have developed nanotech solar cells that can be manufactured at significantly lower cost than

conventional solar cells. Nanotechnology can improve the performance of catalysts used to transform vapors escaping from cars or industrial plants into harmless gasses [17]. The products that are profiled above are merely illustrative of nanomaterials that will soon be available commercially. Similarly, one of the applications of nanotechnology, in the field of reflective coatings is to increase their reflectivity by using reflective inorganic pigments. Highly reflective materials are required in the lighting products, which comprise of coatings on covers and panels, diffuse reflective surfaces, light detectors and integrating spheres, etc.

1.6 Reflective coatings, applications and problems with coatings

The purpose of reflective coatings is to provide maximum reflectance of the incident radiation. In general, a coating is applied to the substrate to beautify its surface appearance or to provide protection against any deterioration. The basic composition of reflective coating comprises of reflective pigment and binder. Reflective coatings find applications in commercial optical products such as: reflective panels, scintillators, integrating spheres, calibrating spectrophotometers, window blinds, and luminaries. Figure 1 shows some of the basic luminaries.

Figure 1.1 Basic luminaries

In general, a luminaire contains a light source and a reflector. Light source can be compact fluorescent lamp (CFL), incandescent lamp or filament, depending on how intense light radiation is required. The reflector comprises of substrate (plastic or aluminium) which is coated with reflective material [19]. This coating protects the substrate from degradation as well as serves as light reflector. Coatings available in the market, have suffered from inadequate reflectivity and excessive sensitivity to temperature [20]. For instance, if the reflectance of a coating is insufficient, the lamp within the luminaire has to emit more light in order to achieve the desired illumination performance characteristics and if it is too sensitive to temperature, it will not be able to withstand heat of the lamp. On overheating, the coating turns brown and its reflective properties deteriorate. To avoid these consequences in the existing coatings, luminaries are often designed to provide relatively large spacing of the reflectors from the lamps, to allow for heat dissipation. This approach, however, increases the overall size, weight and complexity of the luminaire.

Virtually any desired property can be developed into the coating, if the need exists. Ultraviolet light resistance, chemical resistance, impact resistance, glossy appearance, smoothness, and many more characteristics can be achieved by different coatings.

1.7 Coating material

A coating material may be defined as a product in liquid, paste or powder form, which when applied to a substrate, forms a coating which has protective, decorative, or other specific properties such as reflective. A coating material is an engineered formulation of different components that mix to create a specific product with its own reflective characteristics. The following main components are found in coating materials:

1. Pigment

2. Binder

3. Extender

4. Solvent

5. Additive

1.7.1 Pigment – Pigment is insoluble solid particulates of the coatings which are fixed in the binder matrix [21]. The pigment not only determines the color, but is also largely responsible for other properties such as reflectivity, opacity, durability, mechanical strength and corrosion resistance of the coating materials. Pigment can be classified according to a variety of criteria; here we generally follow the standard two classes:

- Inorganic
- Organic

The other classification is done according to their origin:

- Natural pigments
- Synthetic pigments

Industrially, synthetic white reflective pigments are more significant than the natural pigments. Therefore, they are our exclusive focus in the present thesis. Example of synthetic reflective pigment includes titanium dioxide, zinc sulfide, lithopone, zinc oxide, antimony, lead white [22]. These pigments have very little absorbing power in comparison to scattering power for the visible region (400-700 nm).

1.7.2 Binder – Binder binds the pigment to the substrate, film-forming component in which all other components can be incorporated [23]. It determines most of the primary properties of the dried coating, such as adhesion, various optical and mechanical properties, as well as the resistance against specific exposure conditions. Binders may be referred to as convertible and nonconvertible types [24]. Convertible binders use unpolymerized or partially polymerized state of polymers that undergoes polymerization to form a solid film after application to the substrate. Convertible binders include oils, oleoresinous varnishes, alkyds, amino resins, epoxy resins, phenolic resins, polyurethane

resins, and thermosetting acrylics. Nonconvertible binders are polymerized binders dispersed or dissolved in a medium that evaporates after the coating has been applied to leave a coherent film on the substrate surface. Nonconvertible resins include cellulose, nitrocellulose, acrylic, chlorinated rubber, and vinyl resins [25].

1.7.3 Solvent – Solvent is pure or mixed liquid that is used to make the coating material flowable prior to its application [26]. Solvents are chemical substances that can dissolve, suspend, or extract other materials, usually without chemically changing either the solvents or the other materials. It enables the processing of the solid or highly viscous components of the coating materials during manufacture, application, and film formation. Proper solvent for a given task depends on the required properties of the formula, safety and cost. Some of the most common used solvents are water, ethyl alcohol, acetone, ethyl acetate, butyl acetate [23].

1.7.4 Additive – Additive is added to the coating material, usually in small quantities, to achieve special effects [27]. Additives can affect the coating material characteristics and finishing of the coating. Properties that can be adjusted with additives include viscosity, foaming, skinning, pigment dispersion, stability, flexibility/hardness, gloss, UV resistance, fire resistance, bacteria resistance, and many more [28].

1.7.5 Extender – Extender is coating material additives that are insoluble in the binder and solvents of the formula, and have little or no opacity or color effect on the film [23, 29]. They are added to modify the flow and mechanical properties of the coating material as well as for permeability, gloss and leveling characteristics of the coating, rendering the coating material formulation cost effective.

Coating materials are engineered products that include a variety of ingredients to produce the desired results. The coating that works best for a given application is a balance between the needs of the finish and the cost of the coating. The specific

requirements for coating appearance and performance are very important to the selection process. Before moving further on the topic of reflective coatings, it is necessary to first discuss briefly about the reflectance and types of reflectance.

1.8 Basics of reflectance

1.8.1 Reflectance

It is purely a physical phenomenon which describes the interaction of the material with the incident radiation. Reflection is the change in direction of the wavefront at an interface between two different media [30]. In the reflective materials, more fraction of light is reflected than absorbed therefore, the material's surface reflectance, surely is the most important attribute. Also, when the light is reflected from a surface, it is generally scattered in many directions, producing a pattern that is characteristic of the material. In certain fields, percent reflectance is distinguished from reflectance by the fact that percent reflectance is a value that applies to thick reflecting objects. When reflection occurs from thin layers of material, internal reflections cause the reflectance to vary with surface thickness. The percent reflectance is the limit value of reflectance as the surface becomes thick. The reflectance spectrum or spectral reflectance curve is the plot of the percent reflectance as a function of wavelength [31].

1.8.2 Types of reflectance

The amount of light reflected by an object and its direction are highly dependent upon the smoothness or texture of the surface. Depending upon surface, following are the two types of reflections:

1. **Specular reflectance or Regular reflectance -** It is the perfect mirror-like reflectance of light. The angle of incidence (i) equals the angle of reflection (r) as shown in Fig. 1.2(a) [32]. Reflectance from a mirror, a water surface, and highly polished floors are examples of regular reflectance.

2. **Diffuse reflectance or Irregular reflectance -** It has no directional dependence for the viewer. It takes place when a ray of light is incident on matt or rough surface. It is the reflectance in which the light is scattered in various directions (Fig. 1.2(b)). Diffuse reflectance originates from a combination of internal scattering of light, i.e. the light is absorbed and then re-emitted, and also due to external scattering from the rough surface of the object [33]. Reflectance from walls or woods, are examples of irregular reflectance.

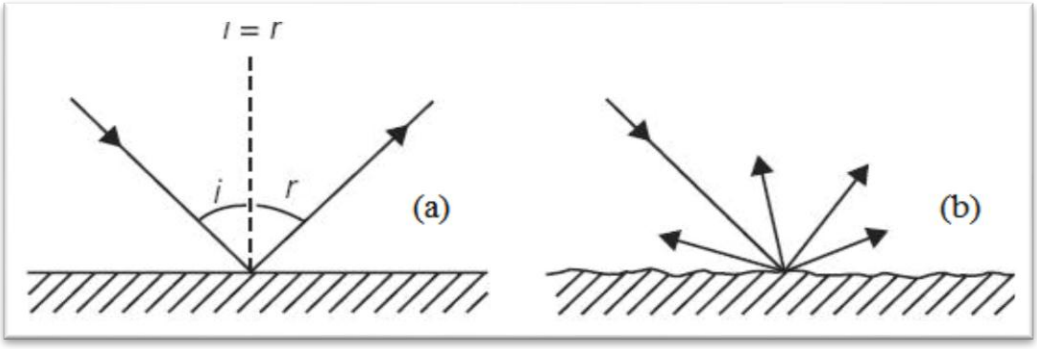

Figure 1.2 (a) Specular reflectance (b) Diffuse reflectance [32]

1.9 Conventional reflective coatings

As of today, the reflective coatings used are of polymeric types [34, 35]. The two most important components of these coatings are reflective pigment and binder. These coatings employ bulk particles of about 0.1 μm size as reflective pigment [36, 37] These pigments are prepared by crushing the minerals obtained from their respective ores; after crushing, aggregated crystals are shattered into small granules. This results in particles of irregular shapes and sizes. Not only do the particles vary in shape and size, but also in their composition [38]. The mineral may contain inclusions in small amounts which act as impurities. As a result, materials absorb certain wavelengths of visible light and their reflective properties deteriorate. The conventional reflective pigments include titanium dioxide, barium sulfate, zinc sulfide, lithopone, zinc oxide, antimony, lead white, etc.

1.10 Parameters that affect the coating reflectance

There are number of parameters on which the reflectance of coating depends. The main constituents of the reflective coating as explained earlier are pigment and binder. For the selection of reflective pigment and binder, in case of a particular application, several points have to be considered. The properties of these two materials are important in determining reflectance efficiency and hence economics. The following properties are important in determining the reflectance of the coatings:

1. Shape, size and distribution of particles
2. Refractive indices of particles and medium
3. Thickness of the applied film
4. Band gap of the materials

1.10.1 Shape, size and distribution of particles

Primary particles (uniform shape and size such as sphere, cube, rod), agglomerates and aggregates (non-uniform shape and size) are used as pigment in industry. Primary particles are those which are recognizable by appropriate physical methods (e.g., by optical or electron microscope). Agglomerates are assembly of primary particles (e.g., joined together at the corners and edges), whose total surface area does not differ appreciably from the sum of the individual surface areas. Aggregates are assembly of primary particles that have grown together and are aligned side by side; the total surface area is less than the sum of the surface areas of the primary particles [39]. Particles corresponding to uniform shape and high surface area result in high reflectivity, high opacifying power and brightness.

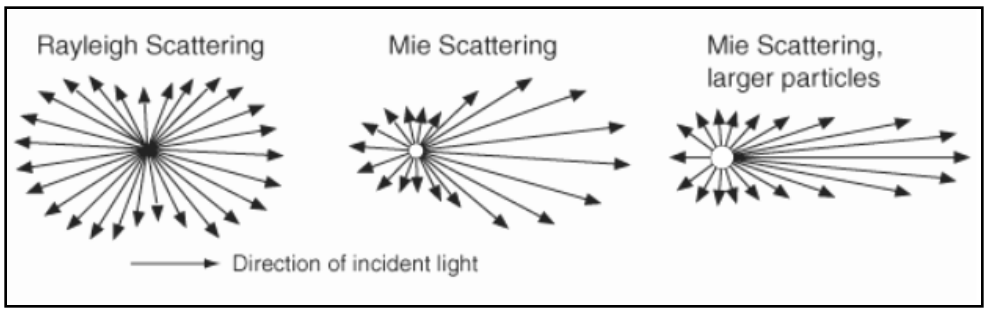

Figure 1.3 Effect of particle size on the reflectance [40]

Fig. 1.3 shows the effect of particle size on the reflectance. According to Rayleigh scattering, if the size of the particles is up to one tenth of the incident wavelength then they scatter the light uniformly in all directions [40]. Therefore, the scattering of visible light (400 – 700 nm) is the maximum if the particle size is less than 70 nm. For particle size larger than incident wavelength, Mie scattering predominates. This scattering produces an antenna lobe pattern, with a sharper and more intense lobe for larger particles (Fig. 1.3).

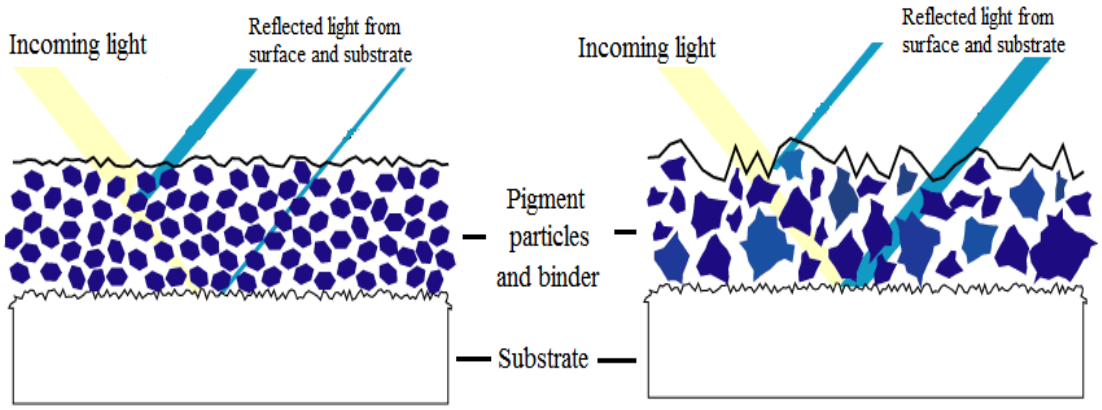

Figure 1.4 Effect of shape and distribution of particles on reflectivity of coatings [38]

Fig. 1.4 shows the dependence of particle shape and distribution on the reflectivity of coating. It reveals that the uniformly shaped, sized and distributed particles in the coating provide more reflectance as compared to the substrate, unlike in the case of

non-uniform shaped, sized and distributed particles, where the reflectance observed from the particles is less as compared to the substrate [38].

An optimal shape, size and distribution of the particles are important because they influence gloss, hiding power, tinting strength and lightening power [41]. Coatings must not be too thick. Therefore, pigments with high hiding power combined with optimum dispersing properties are needed. Industrially, the mean particle size of inorganic pigments lies in the range between 0.1 and 1 μm [37]. For practical applications, it is very desirable to determine not only the mean particle size but also the whole distribution. Measuring and counting the particles shown on a suitable electron micrograph is the most straightforward means of determination of the particle size distribution of inorganic pigments [39].

1.10.2 Refractive indices of particles and medium

Although shape, size and distribution of particles are important in order to determine the reflectivity of coatings but these parameters are not well enough to get maximum reflectance from the coating. It is well known that for the same coating thickness, not all the coatings exhibit similar reflective properties. A key factor in the high reflectivity of coatings is the refractive index of the pigment, which measures the ability of a substance to bend light. The particles with low refractive index give rise to insufficient reflectance from coating. In this case, the light is mainly reflected from the substrate leading to lower reflectivity and hiding power of the coatings [42]. It is believed that pigment with high refractive index is only responsible for the high reflectance of the coatings. But the fact is that the reflectivity of a coating is largely influenced by the relative refractive indices of the pigment and the medium (binder) surrounding the pigment [43]. Using a medium of high refractive index, it can be shown that the most opaque pigments, even lead white, appear transparent. This demonstrates that the hiding strength and reflectivity of a pigment can be lost through a change in the conditions that surround the pigment, or in the case of paint, a change in the binder [38]. Higher the

difference between the refractive indices of pigment and binder, maximum is the reflectance. Therefore, pigment with higher refractive index and binder with lower refractive index is the preferred choice for the reflective coatings.

1.10.3 Thickness of the coating

Thickness of the coating has been found to influence its reflectance, hiding capability and overall cost. Depending on the distribution of particles in the coating, a coating can be characterized as high gloss, semi gloss, flat and over pigmented. With increasing thickness, coating reflectance increases as large thickness will have more number of pigments on the substrate, which contributes to higher reflectance. But, there is a particular limit of the coating thickness above or below which there is no increase in the reflectance. This limit is decided by critical pigment volume concentration (CPVC). CPVC has been defined as: the transition point above or below which substantial differences in the behavior and appearance of coatings are encountered [44, 45]. It is that point in a coating system, at which the binder ratio is sufficient enough to completely fill the voids left between the pigment particles, formed after volatilization of thinner or water. It represents the compact degree of packing of the pigment particles commensurable with degree of dispersion. Below CPVC, the coating is coherent and relatively impermeable. Above CPVC, the coating becomes progressively more porous. Thus, most of the desirable properties of coatings deteriorate very rapidly above the critical point. Almost all the properties of the coatings such as protective qualities, gloss, blistering, rusting, surface roughness, hiding, tensile strength radically change at this point [46].

1.10.4 Band gap of the materials

Band gap plays an important role in determining the reflective properties of any material. The mechanism behind the white color and high reflectance in many materials

can be explained by the band theory [47]. According to band theory, a specific minimum energy is required to excite electrons across the energy gap from the valence band to the conduction band which decides the color of the materials. If a substance has a large band gap (>3 eV), no light in the visible spectrum (400 - 700 nm) is absorbed [48]. Such substances transmit the entire incident light and are, therefore, colorless in their pure forms whereas when they are in powdered form, the light is reflected back and they appear white. So, it can be concluded that "large band gap materials" are excellent reflectors of light.

1.11 Need of nanomaterials based coatings

As aforementioned, the materials used in the industry are in the bulk form, which are non uniform in shape, size and composition. Also, these materials are not free from defects and impurities. These problems can be solved by creating novel materials with unique crystal structure, morphology and surface chemistry using the concept of nanotechnology. Nanomaterials have attracted a great deal of interest due to their unique characteristics as compared to their bulk counterpart. This increasing interest in the nanomaterials has led to the development of a variety of chemical routes to prepare nanoparticles. Synthesis of nanoparticles can be carried out by various methods such as microemulsion, solvolthermal/hydrothermal, sol-gel, chemical vapor deposition, chemical precipitation, combustion [49]. By optimizing the reaction parameters such as molar concentration of precursors, pH, reaction temperature, surfactant type and its concentration, dopant type and its concentration, it is possible to synthesis a variety of nanoparticles with different shape, size and composition keeping intact the monodispersity [50].

There are number of materials, such as Titanium dioxide (TiO_2), Zinc sulfide (ZnS), Zinc oxide (ZnO), Barium sulfate ($BaSO_4$), lithopone ($ZnS+BaSO_4$), lead (Pb), which have high diffuse reflectance and can be employed in reflective coatings as pigments [43]. These materials at nanoscale are most promising pigments in the reflective coatings.

Among these, TiO_2 and ZnS are effective opacifier in the powder form because of their large band gap energy and high index of refraction [51-53]. These are exploited as reflective pigment to provide whiteness and opacity to products such as paints, coatings, plastics, papers, inks, foods, medicines (i.e., pills and tablets) as well as most of the toothpastes. TiO_2 and ZnS are user friendly and non toxic materials in nature.

1.12 Nanocoating - A coating containing nanoparticles. Nanocoating may substantially enhance the reflectivity of coating and it can replace many of today's industrial paints and coatings [47]. Nanocoating, "liquid-solid", is composed of extremely tiny particles possessing unique characteristics like:

- High flexibility
- Easy adhesion
- Resistance to corrosion

Nanosized particles can be easily incorporated into the substrate pores, which enhance the resistance to corrosion of the substrate. Also this provides easy adhesion and high flexibility of the coating. Bulk particles cannot be incorporated into the substrate as well as adhesion with substrate is difficult, thereby reducing the resistance to corrosion and flexibility of the coating.

1.13 Structure of thesis

This thesis presents the synthesis and investigation of structural, morphological and optical properties of ZnS and TiO_2 nanoparticles. Also, employing these nanoparticles as reflective pigments, coating materials have been prepared and their coatings applied on different substrates to develop reflectors. Diffuse reflectance of the coatings has been investigated.

The present thesis has been divided into six main chapters, as follows:

Chapter-1: Introduction

The ever-increasing need for more specialized materials continuously pushes the envelope of modern technology, equipment and human intellect. Precise control on the size, physical, chemical, and electronic properties of materials can allow us to harness their applications in diverse fields. This chapter deals with brief and selective history of the nanomaterials and their applications. It is also imperative to introduce one of the applications of nanomaterials, i.e., reflective coatings, on which the whole thesis work is based.

Chapter-2: Materials and Characterization

Understanding of the properties of the materials used for reflective coatings is essential for their characterization selection. Material characterization is the process of determining structural, morphological, electronic and optical properties of a material, which plays an important role for the development of advanced materials and their use in diverse applications. In this Chapter, the basic structural properties of ZnS and TiO_2 have been explained briefly along with characterization techniques, which include X-ray diffraction (XRD), Scanning electron microscopy (SEM), Transmission electron microscopy (TEM), Fourier transform infrared (FTIR) spectroscopy, Photoluminescence (PL), UV-visible absorption spectroscopy and UV-visible diffuse reflectance spectroscopy (DRS).

Chapter-3: Experimental

The performance of a material depends on its properties. The properties in turn, depend on the atomic structure, microstructure, defects and interfaces, which are further controlled by thermodynamics and kinetics of the synthesis. New strategies for the synthesis of materials are of fundamental importance in the advancement of science and technology. A unified approach has been presented here for the synthesis of ZnS and

TiO_2 nanoparticles, which enable control over structural, morphological and optical properties. This chapter deals with the synthesis of ZnS nanoparticles by chemical precipitation technique and TiO_2 nanoparticles by sol-gel technique. Also, coating materials have been prepared by dispersing synthesized ZnS/TiO_2 nanoparticles and acrylic binder in de-ionized water by adjusting various parameters such as pigment to binder ratio and solvent ratio. The prepared coating materials have been applied on plastic/aluminium substrates with different binder weight ratio as well as different coating thicknesses to develop reflectors.

Chapter-4: Results and discussion

Proper analysis of the results is the most important factor for their successful discussion. For the proper analysis, the results must be supported by the physics behind them. It is equally important to see that the results are supported or refuted by the hypothesis/phenomena This chapter deals with structural, morphological and optical characterization of synthesized ZnS and TiO2 nanoparticles using XRD, SEM, TEM, FTIR, PL, UV-Vis, DRS along with optical characterization of their reflective coatings using DRS. To check the durability of the reflective coatings, the reflectors have been exposed to different temperatures as well as illuminations and their diffuse reflectance has been investigated.

Chapter-5: Conclusions

This Chapter deals with the overall views and winding up of the output of the research works

Chapter-6: Future work

This chapter deals with the future scope of the presented research work.

Chapter 2

Materials and characterization

Understanding of the materials' properties is essential for their characterization selection. Material characterization is the process of determining structural, morphological, electronic and optical properties of a material, which play an important role for the development of advanced materials and their use in diverse applications. In the present chapter, the properties of ZnS and TiO_2 have been explained briefly along with the characterization techniques employed, which include X-ray diffraction (XRD), Scanning electron microscopy (SEM), Transmission electron microscopy (TEM), Fourier transform infrared (FTIR) spectroscopy, Photoluminescence (PL), UV-visible absorption spectroscopy and UV-visible diffuse reflectance spectroscopy (DRS).

2.1 Zinc sulfide (ZnS)

Zinc sulfide is a II- IV semiconductor material having formula ZnS. It has wide band-gap energy of 3.68 eV for bulk cubic phase and 3.80 eV for bulk hexagonal phase [51] Due to large band gap, ZnS is an essential phosphor host lattice material for electroluminescent devices. It is one of the most important materials in photonics owing to its high transmittance in visible region and high index of refraction (Table1) [52]. It

has been used as a reference material to test several theoretical models in condensed matter physics [54].

2.1.1 Zinc sulfide crystal structures

ZnS is a white to yellow colored powder, which crystallizes in two different forms: zinc blende (sphalerite) and wurtzite [51]. The zinc blende and wurtzite ZnS (MX) compound have a diamond-like crystal structure with tetrahedrally coordinated atoms comprising of metal M and nonmetal X, placed in alternating layers [55]. The two types of structures have the following features in common:

- 1:1 stoichiometry of Zn:S
- Coordination of 4 for each ion (4:4 coordination)
- Tetrahedral coordination

Zinc blende (sphalerite) is based on FCC lattice of anions whereas wurtzite is derived from HCP array of anions. In both structures, the cations occupy one of the two types of tetrahedral holes present. In either structure, the nearest neighbor connections are similar, but the distances and angles to consecutive neighbors are different. Zinc blende has 4 asymmetric units in its unit cell whereas wurtzite has 2. The ionic radius of the zinc ion is 0.74 Å and that of the sulfide ion is 1.70 Å. The ratio of radii for the cation and anion is thus r+/r- = 0.74/1.70 = 0.44. With a radius ratio of 0.44, one might expect the zinc ions to occupy octahedral holes; however, the value of 0.44 is only slightly larger than rhole/r = 0.414 for an octahedral hole. If the sulfide ions originally adopt a hexagonal closest-packed structure, the ZnS crystal is wurtzite. If the sulfide ions originally adopt a cubic closest-packed structure, the ZnS crystal is zinc blende [56].The transition from the sphalerite form to the wurtzite form occurs at around 1020^{o}C [57].

2.1.1.1 Zinc blende crystal structure

Fig. 2.1(a) shows a ball-and-stick model of the zinc blende structure. It is best thought of as an FCC array of anions and cations occupying one half of the tetrahedral holes. There are two such FCC lattices, which are separated by one quarter of the body diagonal of the unit cube. One lattice is occupied by Zn atoms, the other by S atoms. Each ion is 4-coordinate and has local tetrahedral geometry. Zinc blende has its own antitype; one can switch the anion and cation positions in the cell [58].

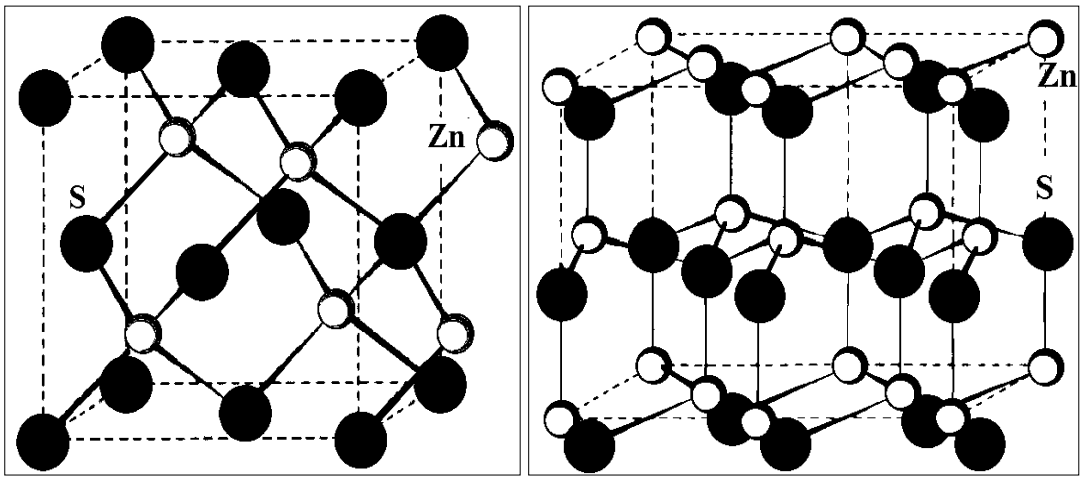

Figure 2.1 Unit cell structure of (a) zinc blende lattice (b) wurtzite lattice

2.1.1.2 Wurtzite crystal structure

This is another structure adopted by zinc sulfide. Fig. 2.1(b) shows a ball-and-stick model of the wurtzite structure (ZnS). This is a hexagonal form of the zinc sulfide. It is built from two interpenetrating HCP lattices. In this form, HCP array of sulfide anions and zinc cations occupy half the tetrahedral holes. There are two tetrahedral holes for each atom in the HCP array, so the stoichiometry of the compound dictates that only half of them are occupied. All the atoms in wurtzite structure are 4-coordinateand has local tetrahedral geometry [59].

2.2 ZnS as a reflective pigment

Due to wide band gap and high refractive index of ZnS, it is used as a reflective pigment in the reflective coatings [60]. Zinc sulfide was introduced as a synthetic white pigment in 1852, although it was not widely used due to the grey hue imparted by trace iron; a purer form was introduced in 1927 [61]. Heaton reported that when synthetic zinc sulfide was prepared by precipitation it gave a white substance of great opacity [62]. The co-precipitation of zinc sulfide with barium sulfate gives the widely used pigment known as lithopone. Buxbaum reported that although zinc sulfide pigments were of economic importance, they still had continually lost volume to titanium dioxide white pigments since 1950s [63].

2.3 Titanium dioxide (TiO_2)

Titania is an important n type semiconductor with a relatively wide band gap and high refractive index [53]. It is a very well-known and researched metal oxide material due to stability of its chemical structure, biocompatibility, physical, optical and chemical properties [49]. Titania has wide applications such as in heterogeneous catalysis, photocatalyst, gas sensor, white pigment, solar cell, corrosion protective coating, optical coatings, ceramics [64].

2.3.1 Titanium dioxide crystal structures

The naturally occurring oxide of titanium at atmospheric pressure exhibits three polymorphs: rutile, anatase, and brookite. All of three polymorphs i.e., anatase, rutile and brookite have been first identified mineralogically respectively in 1799, 1801 and 1852 [65]. While rutile is the stable phase, both anatase and brookite are metastable. Brookite is difficult to synthesize so it is seldom studied [66]. Anatase shares many of the rutile properties such as luster, hardness and density. However due to structural differences, anatase and rutile differ slightly in crystal habit and more distinctly in cleavage. Anatase

to rutile phase transformation for TiO_2 mainly occurs at 650°C to 800°C [67]. Another five high-pressure phases of TiO_2 have been reported [66]:

- TiO_2 II or srilankite; an orthorhombic polymorph of the lead oxide structure
- Cubic fluorite-type polymorph
- Pyrite-type polymorph
- Monoclinic baddeleyite-type polymorph
- Cotunnite-type polymorph

The stability of these phases has been discussed in several publications [68, 69]. However, these are of minor significance for research and development applications [66].

2.3.1.1 Anatase crystal structure

Anatase crystallizes in the tetragonal system with dipyramidal habit (Fig. 2.2 (a)) [70]. Crystals of anatase are very distinctive and are not easily confused with any other mineral. They form the eight faced tetragonal dipyramids with sharp elongated points (Fig. 2.2 (a)). The elongation is pronounced enough to distinguish this crystal form from octahedral crystals.

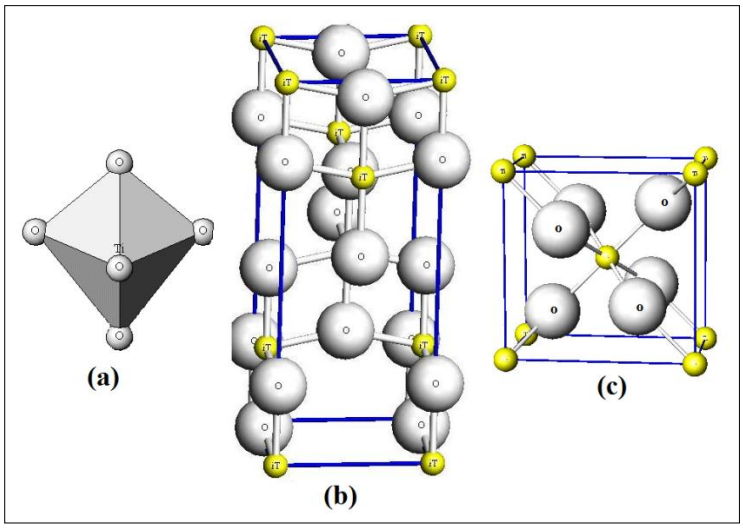

Figure 2.2 (a) Tetragonal unit cell structure (b) Unit cell structure of anatase crystal (c) Unit cell structure of rutile

Fig. 2.2(b) shows the unit cell structure of anatase crystal. Each titanium ion is surrounded by octahedra of six oxygen ions and each oxygen ion is surrounded by three titanium atoms in a trigonal arrangement. The octahedron is significantly distorted so that its symmetry is lower than the orthorhombic [50]. The titanium – titanium distance in anatase are larger, whereas the titanium – oxygen distances are shorter than those in rutile. In the anatase structure, each octahedron is in contact with eight neighbors (four sharing an edge and four sharing a corner). These differences in lattice structures cause different mass densities and electronic band structures between the two forms of TiO_2 [71].

2.3.1.2 Rutile Crystal Structure

Titanium dioxide occurs naturally as the mineral rutile. The ionic radius of the titanium (IV) ion is 0.745 Å and that of the oxide ion is 1.26 Å. The ratio of radii for the cation and anion is $r_+/r_- = 0.745/1.26 = 0.591$. With a radius ratio of 0.591, the cubic holes are too large ($r_{hole}/r = 0.732$) to occupy the tetragonal hole [72]. The titanium ions will prefer to occupy octahedral holes in a closest-packed structure. Nature chooses to pack the oxide ions in rutile in a hexagonal closest-packed structure. Rutile crystallizes in the tetragonal system with prismatic habit [70].

Fig. 2.2(c) shows unit cell structure of rutile crystal. The titanium ions, which are smaller than the oxide ions, are inserted into octahedral holes and push the oxide ions apart so that no two oxide ions are in contact with each other. The unit cell for rutile, however, is based upon the titanium ions, not the oxide ions. The unit cell contains two layers of oxide ions, with three ions in each layer.

If viewed down the (110) axis, rutile appears to have fourfold symmetry, but in fact contains a screw axis, located along the interstitial cavities [73]. Among hetero-cationic rutile structures, distortions of the octahedra are primarily from second order

Jahn-Teller distortion, where the axial bond lengths are slightly longer than the ones along the equatorial [74]. Octahedral twists or cationic displacements are minimal.

The general rutile structure takes the form AB2 and has tetragonal symmetry. It is composed of alternating TiO_6 octahedra unit. The octahedra link formed by sharing edges and corners that apparently becomes the outwardly extended boundaries of the unit cell. This makes the coordination number 6 for titanium and 3 for oxygen.

2.4 Titania as a reflective pigment

All the three forms of titania have high refractive indices and large band gaps as compared to other materials (Table 1) [48]. The anatase phase is used for photocatalysis due to its high photoreactivity [67]. Brookite phase is difficult to produce and, therefore, has no value in the pigment industry [61]. Rutile phase is thermodynamically the most stable and possesses the highest density with compact atomic structure [75]. Titania having rutile phase is largely employed as reflective pigment in the polymeric coatings [76, 77] owing to its effective light scattering properties. A coating containing even small amount of titania (rutile phase) reflects almost the entire visible light. The reflective coating of titania finds applications in commercial optical products, such as: optical fibers, scintillators, integrating spheres, calibrating spectrophotometers, window blinds, luminaries, and reflective panels [25, 20].

Titania has been explosively employed as white pigment in paints, food colors, cosmetics, toothpastes, polymers, and other instances in which white colorization is desired. The reason for this is the high refractive index of rutile phase, which results in high reflectivity from the surface. Consequently, titania of small particle size and correspondingly high surface area is used owing to the resultant opacifying power and brightness. Many of the applications depend not only on the properties of titania itself but also on the modifications of the titania host (e.g., with doping and functionlization) and on the interactions of titania with the environment.

Titania pigments are the products of twentieth century technology. Titanium is abundant in nature, while titania was not known until the late eighteenth century. The anatase phase (TiO_2) is not known to have been used in coating materials, essentially because it is rare, but rutile, on the other hand is abundant. Coatings made with bulk rutile are not brilliantly white as compared to the synthetic pigment; the natural product tends to range from yellow through red-brown to almost black. It was also difficult to grind them.

The use of this synthetic product in coatings subsequently took place during the commercial development of the pigment industry in 1950s. Before 1916, these pigments were produced in small experimental batches with limited and rare amount of field-testing by artists and researchers. Larger quantities became available after World War I and it was incorporated into ready-made paints; in Europe, the first paint formulation using titanium dioxide was registered in 1919 in Norway. The paint industry remained skeptical till 1920s regarding the claims made for these pigments and the general public seemed to be unaware of them, resulting in less exploration of titania in the color formulations. Even a company in Norway which introduced it to their commercial paints in 1919 did not add it to their line of artists' colors. After this period, the use of titania as a pigment in coating industry gained popularity, expediting its commercialization.

Commercial production of titania is carried out under several methods, primarily by (1) hydrolysis of aqueous solutions (sulfate process); (2) vapour phase oxidation of titanium tetrahalides (chloride process); (3) precipitation from aqueous solutions of tetrahalides by addition of a base [78]. Sulfate and chloride processes are generally used commercially. The sulfate process uses the ore ilmentite (iron titanium oxide, $FeTiO_3$) which is dissolved in sulfuric acid, whereby forming ferric iron and titanium sulfates. On adding scrap iron ferrous sulfates (copperas) is formed and removed. The titanium salts are hydrolysed in the presence of titania forming hydrated titanium dioxide. This is further washed, calcined and grinded to produce the pigment. The chloride process uses the ore rutile (TiO_2) as the starting raw material. This method was introduced in Germany

in 1950s. Rutile is mixed with coke and heated to 900°C, at this temperature chlorine is introduced, forming titanium tetrachloride gas. This is condensed and then reheated to 1500°C in the presence of oxygen, whereby titanium dioxide is formed [78].

Table 2.1 Properties of ZnS and TiO_2

Property	**ZnS**	**TiO_2**
Main polymorphs	Zinc Blende Wurtzite	Anatase Rutile
Crystal structures	Zinc Blende: Cubic Wurtzite: Hexagonal	Anatase: Tetragonal Rutile: Tetragonal
Atoms per unit cell	Zinc Blende: 2 Wurtzite: 4	Anatase: 4 Rutile: 2
Stable Phase at 27^{o}C	Zinc Blende	Rutile
Phase transformation temperature (^{o}C)	Zinc Blende to Wurtzite 1020	Anatase to Rutile 650 – 800
Density (Kg m^{-3})	Zinc Blende: 4096 Wurtzite: 4030	Anatase: 3894 Rutile: 4250
Refractive index	Zinc Blende: 2.37 Wurtzite: n_{ω} = 2.356, n_{ε} = 2.378	Anatase: 2.54 Rutile: 2.79
Band gap energy (eV)	Zinc Blende: 3.68 Wurtzite: 3.80	Anatase: 3.23–3.59 Rutile: 3.02–3.24

2.5 Characterization techniques

2.5.1 Structural characterization by XRD

2.5.1.1 Introduction

X-ray diffraction is a non-destructive technique widely applied for the characterization of crystalline materials. This technique has been used for phase identification, quantitative analysis, determination of structural imperfections and crystal structures. Various kinds of micro and nano-crystalline materials can be characterized by XRD, including inorganics, organics, drugs, minerals, zeolites, catalysts, metals ceramics etc., in the form of powder and thin/thick films.

2.5.1.2 Bragg's law

When a crystal is bombarded with X-rays of a fixed wavelength (equivalent to spacing of the atomic-scale crystal lattice planes) at certain incident angles, intense reflected X-rays are produced on constructive interference of the scattered X-rays (Fig. 2.5) [79].

In order for the waves to interfere constructively, the difference in the travel path must be an integral multiple of the incident wavelength and the diffracted beam of X-rays leaves the crystal at an angle equal to that of the incident.

The general relationship between the wavelength of the incident X-rays, angle of incidence and spacing between the crystal lattice planes of atoms is known as Bragg's law, expressed as [80]:

$$n\lambda = 2d \sin\theta \qquad (2.1)$$

where n (an integer) is the order of reflection; λ, wavelength of the incident X-rays; d, interplanar spacing of the crystal; θ, angle of incidence.

2.5.1.3 Instrumental and working of XRD

Fig. 2.3 shows the pictorial view of the X-ray diffractometer. In X-ray diffractometer, X-rays are generated within a sealed tube that is under vacuum. A current is applied that heats a filament within the tube, the higher the current the greater the number of electrons emitted from the filament. This generation of electrons is analogous to the production of electrons in a television picture tube.

Figure 2.3 Pictorial view of the X-ray diffractometer installed at Thapar Uni. Patiala

A high voltage, typically 15-60 kilovolts, is applied within the tube. This high voltage accelerates the electrons, which then hits a target (commonly made of copper), leading to generation of X-rays. The wavelength of these X-rays is characteristic to that of the target. These X-rays are collimated and directed onto the sample, which has been ground to a fine powder (typically to produce particle sizes of less than 10 microns).

Focused X-ray beam interacts with material atomic planes; part of the beam is transmitted, absorbed, refracted, scattered, and diffracted by these planes. X-rays are diffracted by each material differently, depending on what atoms make up the crystal lattice and how these atoms are arranged. A detector detects the X-ray signal; the signal is then processed either by a microprocessor or electronically, converting the signal to a count rate. Changing the angle between the X-ray source, the sample, and the detector at a controlled rate between preset limits is an X-ray scan [81].

2.5.1.4 Line profile parameters and related applications

The observed diffraction line profiles in a powder diffraction pattern are distributions of intensities (I) vs angle (2θ) and is defined by several parameters: (i) the reflection angle position, 2θ at the maximum intensity (related to the lattice spacing d of the diffracting hkl plane and the wavelength λ), (ii) the dispersion of the distribution, full-width at half-maximum and integral breadth, (iii) the line shape factor [82]. The specific applications derived from each of them have been listed in Table 2.2.

Table 2.2 Diffraction line parameters from X-ray diffractogram

Diffraction line parameter	**Applications**
Peak position	• Unit-cell parameter refinement • Pattern indexing • Space group determination • Anisotropic thermal expansion • Macrostress: $\sin^2\psi$ method • Phase identification

Intensity	• Phase abundance • Reaction kinetics • Crystal structure analysis (whole pattern) • Rietveld refinement (whole pattern) • Search/match, phase identification • Preferred orientation, texture analysis
Width/breadth and shape	• Instrumental resolution function • Microstructure: line profile analysis • Microstructure (crystallite size, size distribution, lattice distortion, structure mistakes, dislocations, composition gradient), crystallite growth kinetics • Three-dimensional microstructure (whole pattern)

2.5.1.5 Information from XRD

Following information can be extracted from XRD:

- **Phase identification and crystal structure analysis**: It is traditionally based on a comparison of observed data with interplanar spacing (d) and relative intensities (I) compiled for crystalline materials. The Powder Diffraction File, edited by the International Centre for Diffraction Data (ICDD), contains powder data for more than 1,30,000 substances. New search and match procedures are available, e.g. the software developed by Socabim (F) based on digitized patterns.

- **Scherrer crystallite Size:** The crystallite size as measured by the Scherrer formula is given by [83]:

$$d = \frac{K\lambda}{\beta_{1/2} cos\theta} \qquad (2.2)$$

where d is the crystallite size; λ, the wavelength of X-rays; θ, the Bragg's angle and K, unit cell geometry dependent constant whose value is typically between 0.85 and 0.99; $\beta_{1/2}$, the full width at half maximum (FWHM) of the diffraction peak. One way to represent $\beta_{1/2,}$ is [83]

$$\beta_{1/2}^2 = \beta_{obs}^2 - \beta_m^2 \qquad (2.3)$$

Where β_{obs} is the measured peak width and β_m is the beak broadening due to the machine.

In addition, the lines may be broadened as a result of lattice strain in the region of crystal diffraction. The broadening due to strain β_s, can be given as [84]:

$$\beta_s = \eta tan\theta \qquad (2.4)$$

where η is the strain distribution. Ignoring the crystal constant, the broadening due to particle-size, given by Scherrer formula, can be written as [85]:

$$\beta_p = \frac{\lambda}{t\ cos\theta} \qquad (2.5)$$

where t is the effective particle size. Equations 2.2, 2.3 and 2.4 can be used to plot a graph between:

$$\frac{\beta_{1/2} cos\theta}{\lambda} = \frac{\eta sin\theta}{\lambda} + \frac{1}{t} \qquad (2.6)$$

The intercept gives the measure of the effective particle size, t, and the slope gives the measure of strain distribution, η.

- **Phase transition:** X-ray diffraction gives a pattern characteristic of the phase of the material and hence the transformation from one phase to another can be differentiated. Thus, the technique can be used to analyze the phase transitions of the materials as a function of temperature. Near the phase transition, new diffraction peaks appear or the old ones disappear according to the symmetry of

the new phase. The transition is sharp and discontinuous for the first order phase transition, whereas it is broad and continuous for the second order. If the material melts, all sharp lines disappear and are replaced by abroad amorphous pattern. In some cases, the peaks may split or coalesce. In such cases the symmetry may change, due to the distortion of the existing structure rather than replacement by a completely different one.

- **Weight fraction of different phases:** The weight fraction (W_R) of particular phase content can be obtained from the following equation [86]:

$$W_R = \frac{1}{(1 + I_A / SI_B)} \qquad (2.7)$$

whereI_A and I_B are the intensities of most intense peaks of phase A and phase B respectively and S, the coefficient of the ratio of peak intensity of 100% wt. of phase A and phase B.

2.5.1.6 Sample preparation

The synthesized material is crushed using an agate mortar and pestle. In this way, particle size of 1-10 microns can be easily achieved within a few minutes by manual grinding [87]. The required sample holder (usually for 0.2 gm powder) for XRD is cleaned in a conventional way using sand paper or analytical ethanol. After the cleaning, the powdered sample is placed into it and then compressed tightly with glass plate.

In the present work, using PANanalytical X'Pert Pro X-ray diffractometer with CuKα (λ=1.542 Å) as a radiation source, phase purity, crystal structure, phase transition temperatures and weight fractions of different phases of the samples were determined.

2.5.2 Scanning electron microscope (SEM)

2.5.2.1 Introduction

The scanning electron microscope is one of the most versatile instruments available for the analysis of the material's morphology and chemical composition. After the discovery in 1890s, that the electrons can be deflected by the magnetic field [88], electron microscopes have been developed by replacing the light source with high energy electron beam. Electrons have much shorter wavelength ($0.5A^0$<) as compared to visible light photon (>$400A^0$) which results in higher-resolution information. Enhanced resolution in turn permits higher magnification without loss of detail [88].

Figure 2.4 Pictorial view of SEM at Thapar Uni. Patiala

2.5.2.2 Instrumental and working of SEM

Fig. 2.4 shows the pictorial view of SEM. The electron gun, on the top of the column, produces the electrons and accelerates them to an energy of 0.1–30 keV. The diameter of electron beam produced by hairpin tungsten gun is too large to form a high-resolution image. So, electromagnetic lenses and apertures are used to focus the electron beam and to form a small focused electron spot on the specimen. This process demagnifies the size of the electron source (~50 μm for a tungsten filament) down to the final required spot size (1–100 nm). A high-vacuum environment, which allows electron to travel without scattering by the air, is needed. The specimen stage, electron beam scanning coils, signal detection, and processing system provide real-time observation and image recording of the specimen surface. Before putting a sample in the SEM it is necessary to consider a few things. SEM has vacuum inside; therefore the samples need to be dry. Also, as the SEM works with electrons, the sample has to be coated with a thin film of usually gold, sometimes carbon, to conduct electricity. Once the sample has been prepared properly, it is placed on a stage inside the vacuum chamber. After the air is pumped out of the column, electron gun emits a beam of high energy electrons. This beam travels downward through a series of magnetic lenses designed to focus the electrons to a very fine spot. At the bottom end of the column, a set of scanning coils moves the focused beam back and forth across the specimen, row by row. Incident electron strikes the specimen surface, instead of being bounced off immediately; the energetic electrons penetrate some distance into the specimen before colliding with atoms. In doing so, the incident electron beam produces a region of primary excitation, from which a variety of signals are produced (Fig. 2.5). Secondary electrons are knocked from the specimen surface. A detector counts these electrons and sends the signals to an amplifier. The final image is built up from the number of secondary electrons emitted from each spot on the sample and is displayed on the screen. The newer SEMs are PC controlled and therefore the image is captured directly in a computer [89, 90].

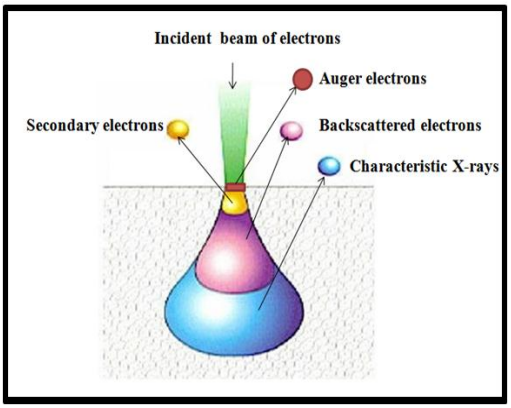

Figure 2.5 Illustration of the signals produced by an electron beam incident on the specimen

2.5.2.3 Information from SEM

The most important feature of SEM is the three-dimensional appearance of its images. The combination of high resolution, an extensive magnification range and high depth of field makes SEM uniquely suited for the study of various surface topographies.

2.5.2.4 Sample preparation

For powder: A small quantity of completely dried powder is sprinkled on carbon or copper tape; excess powder is blown off with compressed air. After that, sample is coated with thin film of gold. The small section of this tape is put into the jaw of sample holder of SEM for analysis [91].

In the present work, size and morphology of the synthesized nanoparticles were studied through JOEL JXA-8200 scanning electron microscope.

2.5.3 Transmission electron microscope (TEM)

2.5.3.1 Introduction

Material properties such as electrical conductivity, strength, magnetization, toughness, chemical reactivity, originate from the internal structural features (types of atoms, and arrangements of these atoms into microstructures) of materials. Locating and identifying individual atoms inside a material has been transformed from a dream of fifty years into experimental methods of today with the advent of TEM [92].

2.5.3.2 Instrumental and working of TEM

Fig. 2.6 shows the pictorial of TEM. It consists of an electron gun as the source of illumination at the top of the column containing a series of lenses, the specimen, and the imaging system. For the proper operation of TEM, the primary need is high vacuum, through which the electrons pass; secondly, a substantial electrical potential (voltage) is also needed to accelerate the electrons out of the source.

Figure 2.6 Pictorial view of TEM

Modern electronics have produced transformers which are reasonably small but capable of generating 60,000 volts. In TEM, condenser lens is used to focus the electron beam onto the sample and an objective lens to produce a focused and magnified image of the illuminated area. One or more projector lenses are then used to project a magnified image of the specimen onto the imaging system. In TEM, images are viewed on the screen that fluoresces when struck by electrons. Traditionally, grayscale still images are captured on silver halide film. Photographic capture of images is gradually being replaced with digital capture using electron-sensitive CCD camera [93].

Two factors complicate the imaging of samples in TEM. First, due to the limited penetration of electrons in matter, specimens for TEM must be extremely thin (approximately 0.1 micron). Second, since the specimens must be inserted into the electron microscope column which is under vacuum, they must be completely dry [94].

2.5.3.3 TEM imaging mode

In TEM, the intermediate lens focuses the electron beam on the image plane of the projector lens. All the transmitted and diffracted rays leaving the specimen are combined to form an image at the viewing screen. In this simple mode of imaging, the specimen shows little contrast. By tracing the individual rays one can ensure that each point in the back focal plane of the objective lens contains rays from all parts of the specimen, but not all the rays are required to form an image. An image can be formed with only those rays passing through one point in the back focal plane. What distinguishes the point located in the back focal plane is that all rays entering a given point have been scattered by the specimen into the same angle. By positioning an "objective aperture" at a specific location in the back focal plane, an image is made with only those electrons that have been diffracted at a specific angle. This defines two imaging modes, illustrated in Figs. 2.7 (a) and 2.7 (b) [92].

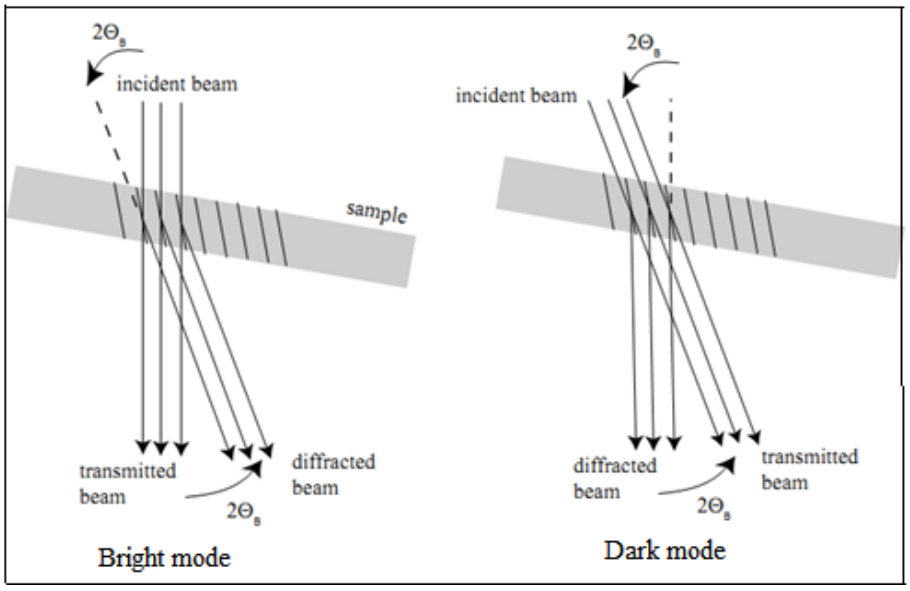

Figure 2.7(a) Bright (b) dark field modes for imaging

- **Bright field mode**: The aperture is positioned to pass only the transmitted (un-diffracted) electrons; a bright-field image is formed. In this mode, a dark image is produced against a brighter background. The contrast is formed directly by absorption of electrons in the sample. Thicker regions of the sample or regions with a higher atomic number appear dark, whilst regions with no sample in the beam path appear bright – hence the term "bright field".

- **Dark Field mode**: The aperture is positioned to pass only some diffracted electrons; a dark-field image is formed. Reflections that are selected do not include the unscattered beam (which appears at the focal point of the lens), the image appears to be dark where no sample scattering is present.

2.5.3.4 Information from TEM

- **Morphology**: The size, shape and arrangement of the particles which make up the specimen as well as their relationship to each other on the scale of atomic diameters.

- **Crystallographic information**: The arrangement of atoms in the specimen and their degree of order, detection of atomic-scale defects in areas of few nanometers in diameter.

2.5.3.5 Sample preparation

For powder: The powdered sample is dispersed in a solvent using ultrasonication. The solvent used (a) should be chemically inert, (b) should not result in agglomeration, (c) should not leave residues on carbon grid, and (d) should evaporate in a reasonable time frame (10-20 minutes) at room temperature. A simple method of examining whether the solution leaves carbon residues or not is to keep a couple of drops on a clean glass slide and observe after evaporation; if the glass slide is not clear, then the solution may not be useful. Hexane, methanol and ethanol are suitable medium. The suspended particles are lifted on a carbon-coated copper grid with the help of forceps or by dipping the grid in the beaker gently and withdrawing horizontally. The grid is dried on a filter paper under an infrared lamp, followed by inspection in the TEM [95, 94].

In the present work, size and morphology of the synthesized nanoparticles were studied through Hitachi H-7500 transmission electron microscope.

2.5.4 Fourier transform infrared (FTIR) spectroscope

2.5.4.1 Introduction

Infrared spectroscopy has been a workhorse technique for material analysis in the laboratories. An infrared spectrum represents a finger print of the sample with absorption peaks which correspond to the frequencies of vibrations between the bonds of the atoms making up the material. Each different material is a unique combination of atoms; no two compounds produce the exact same infrared spectrum. Therefore, infrared spectroscopy can result in a positive identification (qualitative analysis) for every kind of material. In addition, the size of the peaks in the spectrum is a direct indication of the amount of

material present. With modern software algorithms, infrared is an excellent tool for quantitative analysis.

The infrared portion of the electromagnetic spectrum is divided into three regions; near, mid and far infrared. The far-infrared, approximately 400-10 cm^{-1} lying adjacent to the microwave region, has low energy and may be used for rotational spectroscopy. The mid-infrared, approximately 4000-400 cm^{-1} may be used to study the fundamental vibrations and associated rotational-vibrational structure. The high energy of near-IR region, approximately 14000-4000 cm^{-1}, can excite overtone or harmonic vibrations [96].

2.5.4.2 Instrumental and working of FTIR

Fig. 2.8 shows the scheme of FTIR interferometer. Infrared energy is emitted from a glowing black-body source. This beam passes through an aperture which controls the amount of energy presented to the sample (ultimately to the detector). The beam enters the interferometer where the "spectral encoding" takes place. The resulting interferogram signal then exits the interferometer. The beam enters the sample compartment where it is transmitted through or reflected off of the surface of the sample, depending on the type of analysis being accomplished. This is where specific frequencies of energy, which are uniquely characteristic of the sample, are absorbed. Finally, the beam passes to the detector for measurement. The detectors used are specially designed to measure the special interferogram signal. The measured signal is digitized and sent to the computer where the Fourier transformation takes place. The resulting FTIR spectral pattern is then analyzed and matched with known signatures of identified materials in the FTIR library [97, 98].

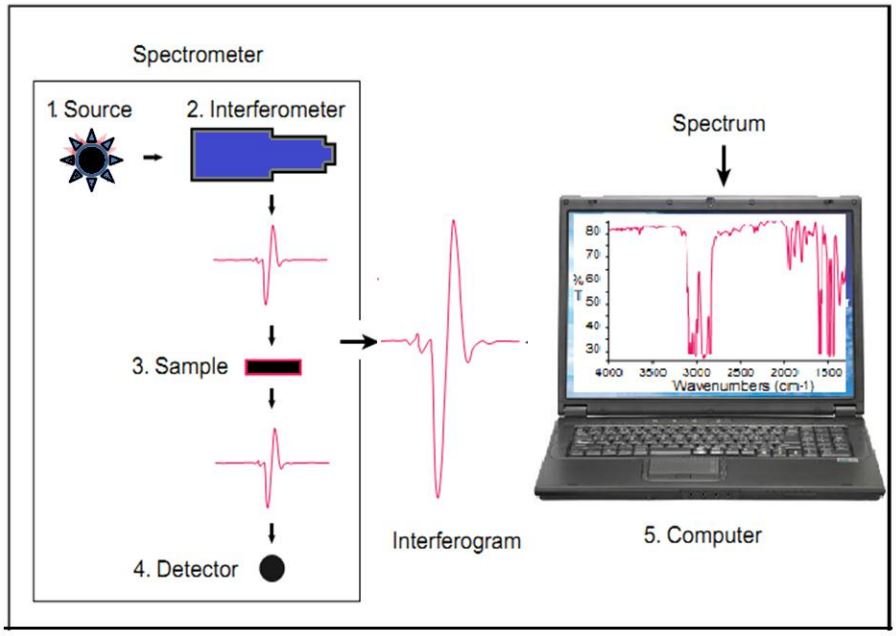

Figure 2.8 Scheme for the signal generation in the FTIR interferometer

Unlike SEM or TEM, FTIR spectroscope does not require a vacuum, since neither oxygen nor nitrogen absorbs infrared rays. FTIR analysis can be applied to minute quantities of materials, whether solid, liquid, or gaseous. When the library of FTIR spectral patterns does not provide an acceptable match, individual peaks in the FTIR plot may be used to yield partial information about the specimen [97].

2.5.4.3 Information from FTIR

- It can identify unknown materials
- It can identify surface passivation by surfactant molecule
- It can determine the quality or consistency of a sample
- It can determine the amount of components in a mixture

2.5.4.4 Sample preparation

For powder: Samples are milled with potassium bromide (KBr) to form a very fine powder. This powder is placed on the FTIR sample substrate which is then analyzed.

In the present work, surface passivation by surfactant molecules has been carried out with Perkin Elmer Spectrum BX II spectrometer.

2.5.5 Photoluminescence Spectroscope (PL)

2.5.5.1 Introduction

Photoluminescence spectroscopy is a contactless, nondestructive method of probing the electronic structure of materials. Light is directed onto a sample, where it is absorbed and imparts excess energy into the material in a process called photo-excitation. Photo-excitation causes electrons within the material to move into permissible excited states. When these electrons return to their equilibrium states, the excess energy is released and may include the emission of light (a radiative process) or may not (a nonradiative process) [99]. The electronic states of most of the molecules can be divided into *singlet* states and *triplet* states.

- **Singlet state**: All electrons in the molecule are spin-paired.
- **Triplet state**: One set of electron spins is unpaired.

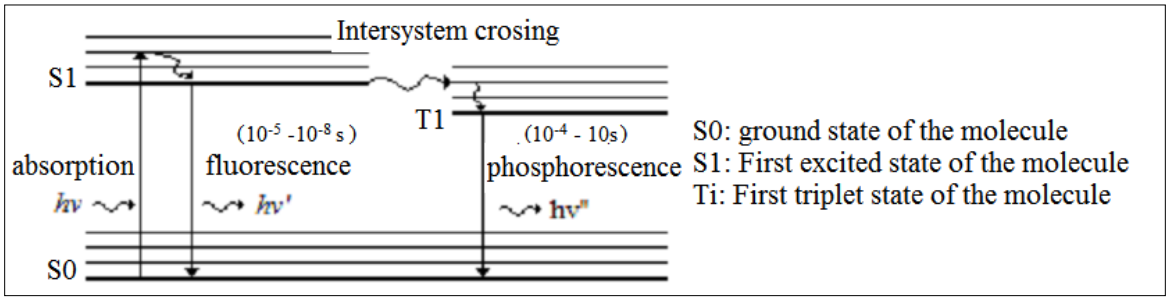

Figure 2.9 Fluorescence and phosphorescence mechanism

A molecule in the singlet state emits photons continuously when exposed to electromagnetic radiation and stops emitting when the source stops transmitting. This phenomenon is called fluorescence. Fluorescence requires that the spin state of the electron remains the same during the transition from the lowest excited singlet state, S1, to the singlet ground state, S0. But a molecule in the excited triplet state decays by using the process of intersystem crossing (Fig. 2.9). This means that it decays in steps, emitting photons of lower intensity each time it decays. This process continues after the source has stopped emitting. This phenomenon is called as phosphorescence. Phosphorescence requires that the spin state of the electron changes during the transition from the lowest excited triplet state, T1, to the singlet ground state, S0. The intensity and spectral content of these phenomenons are direct measure of various important material properties [100].

2.5.5.2 Instrumental and working

PL spectrum measurement setup is usually called spectrofluorimeter. Fig. 2.10 shows the schematic diagram of spectrofluorimeter. The sample is excited with a lamp, which is followed by a monochromator (the excitation monochromator) or a laser beam. The emitted radiation is collected by a focusing lens and dispersed by means of a second monochromator (the emission monochromator), followed by a suitable detector connected to a computer. Two kinds of spectra can be registered:

1. **Emission spectra:** The excitation wavelength is fixed and the emitted light intensity is measured at different wavelengths by scanning the emission monochromator.

2. **Excitation spectra:** The emission monochromator is fixed at an emission wavelength while the excitation length is scanned in a certain spectral range.

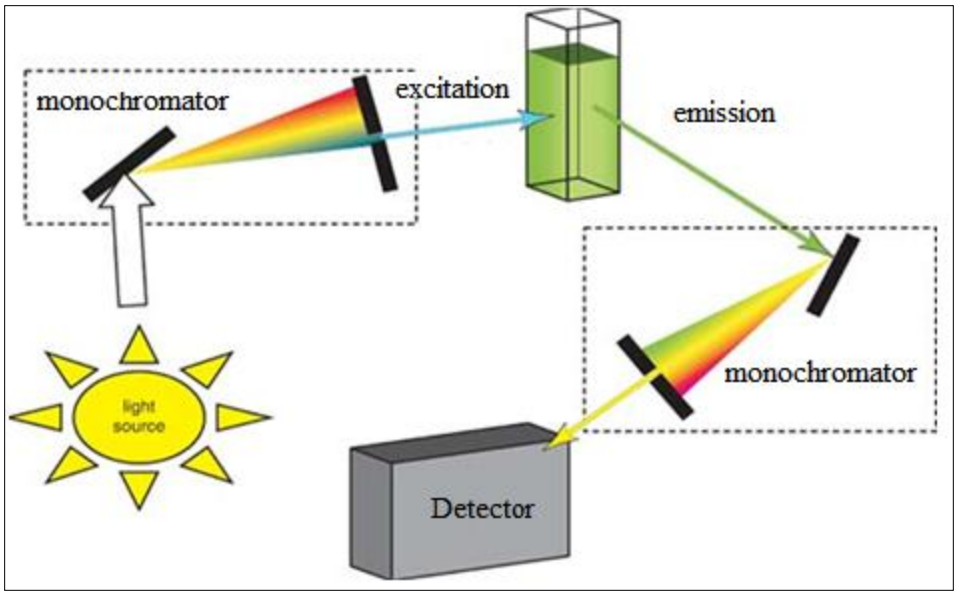

Figure 2.10 Schematic representation of a fluorescence spectrometer

2.5.5.3 Information from PL

- Impurity levels and defect detection
- Recombination mechanism
- Material quality
- Concentration (at low concentrations the fluorescence intensity is proportional to the concentration of the fluorophore)
- Emission and excitation spectra
- pH (some fluorophore are sensitive to pH variations)

2.5.5.4 Sample preparation

The majority of fluorescence assays are carried out in solution. The final measurement being made on the sample contained in a cuvette.

In the present study Cary Varian fluorospectrophotometer has been employed to measure photoluminescence.

2.5.6 UV-visible spectroscope (UV-Vis)

2.5.6.1 Introduction

UV-Vis spectroscopy is the measurement of the wavelength and intensity of absorption of near-ultraviolet and visible light of a sample. When a beam of light passes through a substance or a solution, some of the light may be absorbed and the remainder transmitted through the sample. The ratio of the intensity of the light entering the sample (I_0) to that exiting the sample (I_t) at a particular wavelength is defined as transmittance (T) [101]. This is often expressed as percentage transmittance (%T) as well:

$$\%T = \frac{I_0}{I_t} X\ 100 \qquad (2.8)$$

The absorbance (A) of a sample is the negative logarithm of transmittance (Eq. 2.8):

$$A = -\log T \qquad (2.9)$$

The most important principle in absorption analysis is the Beer – Lambert law. This law states that, for a given ideal solution, there is a linear relationship between concentration and absorbance provided that the path length is kept constant; the absorptivity is a constant for each molecule at each wavelength:

$$A = \varepsilon cl = \alpha l \qquad (2.10)$$

where ε is the absorptivity of the substance; c, concentration l; path length and α; absorption coefficient. The absorption coefficient (α) can be written as a product of molar absorptivity of the absorber, ε, and concentration, c, of absorbing species in the material.

2.5.6.2 Instrumental and working of UV-Vis

A schematic diagram of UV-Vis spectrometer is shown in Fig. 2.11. A beam of light from ultraviolet (UV) or visible light source is separated into its component wavelengths by a prism or diffraction grating. Each monochromatic beam is split into two equal intensity beams by a half-mirrored device.

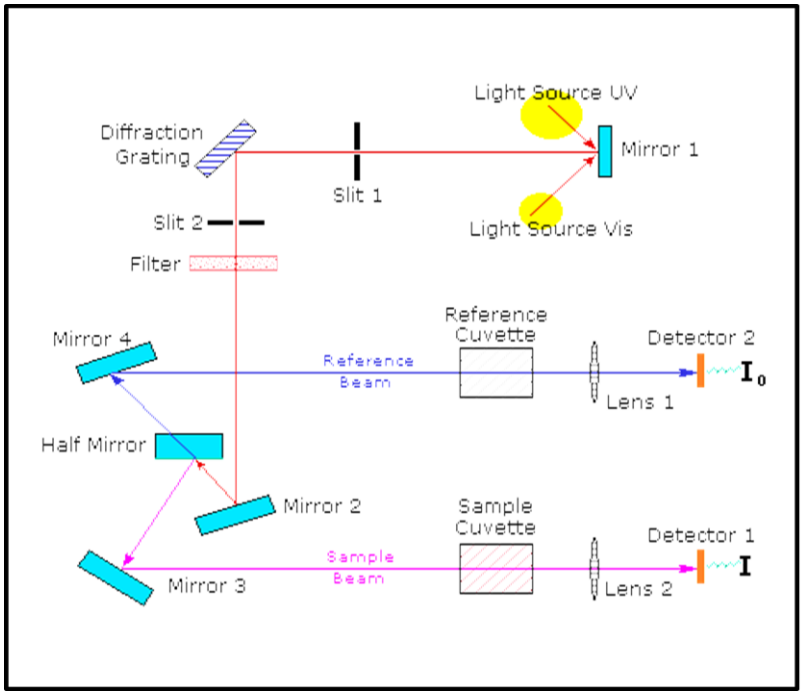

Figure 2.11 Schematic diagram of the dual-beam spectrophotometer

One beam, (sample beam) passes through a small transparent container (cuvette) containing solution of the compound being studied in a transparent solvent. The other beam (reference beam) passes through an identical cuvette containing only the solvent. The intensities of these light beams are then measured by electronic detectors and compared. The intensity of the reference beam, which should have suffered little or no light absorption, is defined as I_0. The intensity of the sample beam is defined as I. Over a short period of time, the spectrometer automatically scans all the component

wavelengths. The UV region scanned is normally from 200 to 400 nm, and the visible portion is from 400 to 800 nm [102, 103].

2.5.6.3 Information from UV-Vis

- **Band gap measurement:** UV-Vis spectrometer gives the sample's absorption/transmission spectrum i.e., a graph of absorbance/transmission against wavelength. The optical band gap can be determined from this absorbance/transmission spectrum. The variation of absorption coefficient (α) with the wavelength (λ) is obtained from the transmittance vs. wavelength plot. If *n* represents the nature of optical transition in a semiconducting material, the absorption coefficient (α) may be expressed as [104]:

$$\alpha = \frac{A}{h\nu}[h\nu - E_g]^n \qquad (2.11)$$

Where *A* is an optical constant; *h*, Planck's constant; *v*, frequency and E_g, the band gap of the semiconductor corresponding to the particular value of *n*. The parameter *n*, representing the nature of optical transition, may have certain specific values such as, 1/2, 2, 3/2 or 3 corresponding to the allowed direct, allowed indirect, forbidden direct and forbidden indirect transitions respectively [105]. For allowed direct transition $(\alpha h\nu)^2$ vs. $h\nu$ is plotted and the linear portion of it is extrapolated to zero value to obtain the corresponding band gap energy of the material.

- Detection of Impurities
- Structure elucidation of organic compounds
- Quantitative/Qualitative analysis

- Dissociation constants of acids and bases
- Chemical kinetics
- Molecular weight determination

2.5.6.4 Sample preparation

The sample (nanoparticles) is dispersed in a solvent using ultrasonicator. The solvent used is chemically inert and does not lead to any agglomeration of the particles. The final measurement is made on the sample contained in a cuvette. In order to obtain good absorption spectra with UV-Vis spectrophotometer, it is necessary to have the solution concentration such that the absorbance lies in between 0.05 to 1.0.

In the present study Perkin Elmer (350) UV-visible spectrophotometer was used to record optical absorption spectra.

2.5.7 UV –Visible diffuse reflectance spectroscope (DRS)

2.5.7.1 Introduction

Diffuse reflectance spectroscopy is an excellent sampling tool for powdered or crystalline materials in the near-ultraviolet and visible spectral ranges. It can also be used for analysis of intractable solid samples. DR spectrum is usually obtained by using a spectro-photometer equipped with DR accessory capable of collecting the reflected flux. This accessory has an internal surface, with a spherical ‘‘integrating sphere’’ or any other suitable geometry that is coated with a white standard intended to collect the light reflected by standard and sample. Modern double-beam spectrophotometers are equipped with holders where the powdered sample and the white standard are tightly packed. The standard is usually $BaSO_4$, MgO, or polytetrafluoroethylene (PTFE) which exhibit near-unit reflectance in the desired wavelength range [106].

2.5.7.2 Reflectance spectra

Reflectance spectra provide similar and complementary information to the absorption measurements. For instance, absorption coefficient corresponding to the fundamental absorption is as high as 105-106 cm^{-1}, so that it can only be measured by using very thin samples (thin films). In these cases, the reflectivity spectra R(v) can be very advantageous, as they manifest the singularities caused by the absorption process along with the possibility for bulk samples. In fact, the reflectivity, R(v), and the absorption spectra, α(v) , can be interrelated by using the so-called Kramers-Krönig relations [107].

The reflectivity at each frequency is defined by:

$$R = \frac{I_R}{I_0} \qquad (2.12)$$

Where I_R is the reflected intensity; I_0, the incident intensity

Reflectance spectra can be registered in two different modes: (i) direct reflectance and (ii) diffuse reflectance [108]. Direct reflectance measurements are made with well-polished samples at normal incidence. Diffusion reflectance is generally used for unpolished or powdered samples. For direct reflectance measurements, monochromatic light (produced by a lamp and monochromator) is passed through a semitransparent lamina (the beam splitter). This lamina deviates the light reflected from the sample towards a detector. For diffuse reflectance measurements, an integrating sphere (a sphere with a fully reflective inner surface) is used. Such a sphere has a pinhole through which the light enters and is transmitted towards the sample. The diffuse reflected light reaches the detector after suffering multiple reflections in the inner surface of the sphere. The integrating spheres can be incorporated as an additional instrumentation in conventional spectrophotometers.

2.5.7.3 Integrating sphere

The function of an integrating sphere is to spatially integrate radiant flux. Before one can optimize a sphere design for a particular application, it is important to understand how the integrating sphere works. Diffuse reflectance relies upon the focused projection of the spectrometer beam into the sample where it is reflected, scattered and transmitted through the sample material. The back reflected, diffusely scattered light (some of which is absorbed by the sample) is then collected by the accessory and directed to the detector optics. Only the part of the beam that is scattered within the sample is considered to be diffusely reflected. The light passing through the sphere is related to two parameters: the sphere multiplier and the average reflectance.

$$R = \frac{\phi_i}{\pi A_s} X \frac{\rho}{1-\rho(1-\rho)} \qquad (2.13)$$

Eq. 2.13 is used to predict integrating sphere radiance (R) for a given input flux (ϕ_i) as a function of sphere diameter (related to area: A_s), reflectance (ρ), and port fraction (1-ρ). The radiance decreases as sphere diameter increases. The second part of the equation is a unit-less quantity which can be referred to as the sphere multiplier. It accounts for the increase in radiance due to multiple reflections. The sphere multiplier in Eq. 2.13 is specific to the case where the incident flux impinges on the sphere wall, the wall reflectance is uniform and the reflectance of all port areas is zero. The general expression for sphere multiplier is:

$$M = \frac{\rho_0}{1-\rho_w\left(1-\Sigma_{i=0}^{n} f_i\right)-\Sigma_{i=0}^{n}\rho_i f_i} \qquad (2.14)$$

where; ρ_0, the initial reflectance for incident flux; ρ_w, the reflectance of the sphere wall; ρ_i, the reflectance of port opening I; f_i, the fractional port area of port opening I [109].

2.5.7.4 Instrumental and working of UV-Vis DRS

Fig. 2.12 shows the UV-Vis spectrometer attached with integrating sphere. A beam of light from ultraviolet (UV) or visible light source is separated into its component wavelengths by a prism or diffraction grating.

Figure 2.12 UV-Vis spectrometer with integrating sphere

Each monochromatic beam is split into two equal intensity beams by a half-mirrored device. One beam (sample beam) is scattered by the sample. The other beam (reference beam) passes through the standard reflective material. The scattered intensities of these light beams are then measured by electronic detectors and compared.

In reflectance measurements, the sample is placed at a port opening opposite the entrance port. The incident flux is reflected by the sample. The total hemispherical reflectance comprising of diffuse and specular components is collected by the integrating sphere (Fig. 2.13).

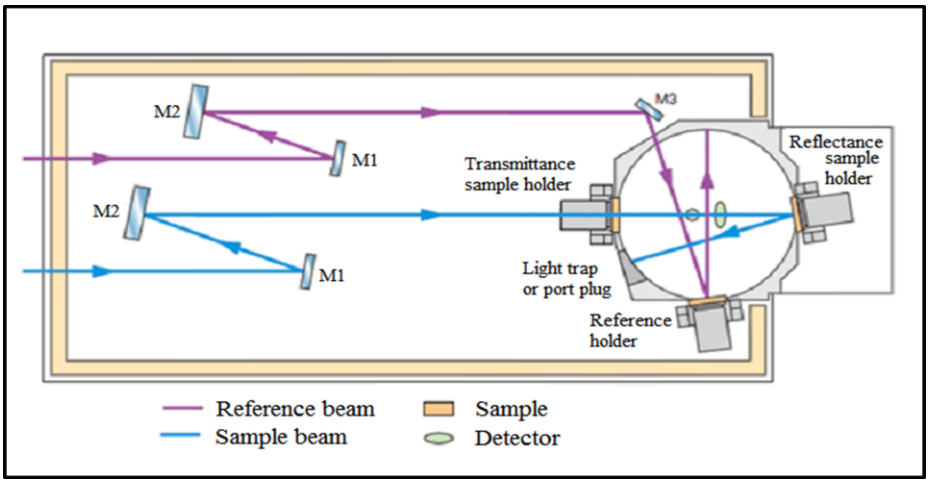

Figure 2.13 Optical design of integrating sphere

The angle of incidence in reflectance measurements usually deviates from the normal by 10°. The specular component can be excluded from the measurement by using normal (0°) incidence or by fitting another port in the specular path and using a black absorbing light trap to extinguish the specular flux.

2.5.7.5 Information from UV-Vis DRS

- **Measurement of diffuse reflectance**: The sphere as part of radiometer or photometer can directly measure the flux originating from lamps and lasers or the flux density produced from hemispherical illumination. Perhaps the largest application of integrating spheres is in the measurement of the total reflectance or transmittance from diffused or scattering materials.

2.5.7.6 Sample preparation

There is no standard method of sample preparation in DRS. Usually, finely grounded powder is carefully packed into a sample holder with a rectangular or circular hole with a surface of a few tens square millimeters to several square centimeters. No special care is exercised when the holder is placed horizontally at the bottom of the integrating sphere, but self-supporting powder mounts are required when the holder is

placed vertically. It is advisable in the latter case to strongly press the powder against unglazed white paper to prevent it from falling into the integrating sphere and avoid undesired particle orientations. Unfortunately, even with unglazed paper, particle orientation can occur and its reflective characteristics vary.

In the present work, the diffuse reflectance of nanoparticles as well coating has been recorded using Perkin Elmer350 UV-Vis spectrophotometer with integrating sphere as an additional component.

Chapter 3

Experimental

The performance of a material depends on its properties. The properties in turn, depend on the atomic structure, microstructure, defects and interfaces, which are further controlled by thermodynamics and kinetics of the synthesis. New strategies for the synthesis of materials are of fundamental importance in the advancement of science and technology. A unified approach has been presented here for the synthesis of ZnS and TiO_2 nanoparticles, which enable control over structural, morphological and optical properties. This chapter deals with the synthesis of ZnS nanoparticles by chemical precipitation technique and TiO_2 nanoparticles by sol-gel technique. Also, coating materials have been prepared by dispersing synthesized ZnS/TiO_2 nanoparticles and acrylic binder in de-ionized water by adjusting various parameters such as pigment to binder ratio and solvent ratio. The prepared coating materials have been applied on plastic/aluminium substrates with different binder weight ratio as well as different coating thicknesses to develop reflectors.

3.1 Synthesis of ZnS

Synthesis of nanometer-sized semiconductor materials using various synthetic methods has been an area of intense activity over the past decade. The emphasis has been mainly given on the synthesis of semiconductor particles belonging to II-IV and III-V groups. These particles exhibit an increase in their electronic band gap with decreasing particle size; a property which is attributed to a strong quantum confinement effect. The

ability to tune the physical properties of nanocrystallites makes them an important category of materials with potential use in a wide range of technological applications.

Among the II-IV semiconductor nanoparticles, ZnS has been extensively studied due to its novel properties which are determined by its size, shape and surface modifications. The high photoluminescence quantum efficiency of ZnS makes it an interesting material for applications in light emitting devices [110], photovoltaic devices, photo-electrochemical devices [111, 112] and biological labels [113] etc. Aqueous and organometallic routes have been the principal synthetic routes to functionalize ZnS, although synthesis of functionalized ZnS nanoparticles with various methods has been reported. ZnS nanoparticles capped with cetyltrimethylammonium bromide, thioglycerol, ethylene glycol, methacrylic acid, polyvinyl pyrrolidone have been prepared, respectively, using the following synthesis methods: microemulsion [114], hydrothermal [115], solvolthermal [116], sol-gel [117], chemical vapor deposition [118]. These methods have their own drawbacks such as low yield, time consuming, secondary phase formation, expensive etc. So, these methods cannot be used for bulk production of ZnS nanoparticles. However, the chemical precipitation method is cost effective, less time consuming and has high yield. Adaptation of this route therefore has been extensively used to synthesize ZnS nanoparticles for the study of their fundamental properties. The method allows for the kinetic control, where parameters such as reaction temperature and precursor molar concentration govern the final morphology and size of the particles.

Controlling the reaction parameters, like: molar concentration of precursors, nature of solvent, reaction temperature, nature and concentration of capping/stabilizing agent, nanoparticles of different structural, morphological and photophysical properties has been well reported [119]. Structural and optical characterization of chemically synthesized ZnS nanoparticles have been reported [120]. In this study, it has been observed that the particle size depends on molar concentration of reactant solutions. Successful synthesis of ZnS nanoparticles in alkaline medium without capping agent

have been reported [51]. Narrow size distributed ZnS nanospheres with controllable size and uniform morphology, fabricated successfully in the reverse microemulsion systems by optimizing the capping agent concentration and reaction temperature have been reported [50]. Effect of capping agent concentration, like: thiophenol, mercaptoethanol, polyphosphate, poly vinyl pyyrodine on the morphological and photophysical properties of ZnS nanocrystals has been reported [121-124]. These studies have revealed that there is decrease in the crystallite size and increase in the PL intensity with increase in the capping agent concentration.

Much work has been reported on the effect of capping agent concentration on the structural, morphological and photophysical properties of ZnS nanoparticles. Control over these properties make ZnS nanoparticles potential candidate in application such as photoconductors, optic modulators, electro-optic modulators, panel displays, electroluminescent devices, sensors, lasers, photocatalysts, infrared windows and non-linear optical devices etc. However, the effect of capping agent concentration on the reflective properties has not been reported for its use as a reflective pigment.

3.2 Introduction to chemical precipitation

Synthesis of nanocrystalline semiconductors by the colloidal route is based upon the controlled precipitation reaction yielding highly dilute suspensions of mono-dispersed colloidal particles. Chemical precipitation is a unit process in which a settleable or filterable solid (precipitate) is formed by the chemical joining of two or more inorganic dissolved chemical species [125]. It may be natural or induced. Whether natural or induced, it depends upon initial concentrations of the participating ions and their solubility, reaction temperature, pH of the solution etc [124]. An important stage of the precipitation process is the onset of nucleation and growth [126]. Chemical precipitation is used for synthesis of pigments, removing salts from water in water treatment, in classical qualitative inorganic analysis etc [127].

3.3 Synthesis and reaction mechanism of ZnS nanoparticles

Chemical precipitation technique has been used to synthesize uncapped and capped ZnS nanoparticles in aqueous solution at room temperature. Fig. 3.1 shows the schematic illustration of the chemical precipitation technique.

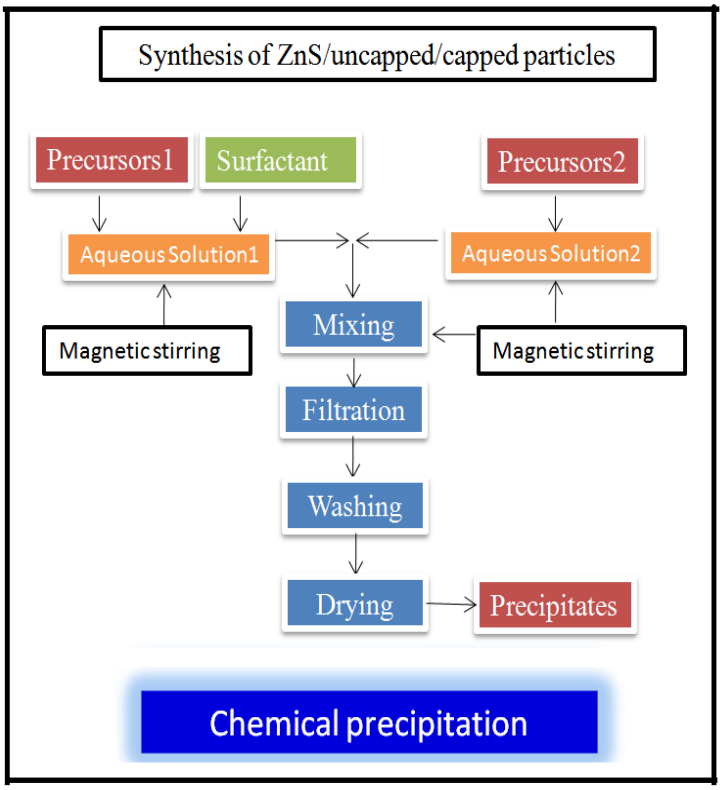

Figure 3.1 Schematic illustration of chemical precipitation technique to synthesize ZnS nanoparticles

Analytical grade chemicals such as zinc acetate ($C_4H_6O_4Zn.\ 2H_2O$), sodium sulfide (Na_2S), ethanol (C_2H_5OH), and 1-thioglycerol ($C_3H_8O_2S$) were used without any further purification.

In a typical procedure, the aqueous solution of sodium sulfide (0.5 M) was added drop-wise into zinc acetate (0.5 M) with constant stirring. Different concentrations by volume (0 - 1.00%) of thioglycerol, as a surfactant, were added to cap ZnS particles. The

precipitates of ZnS, capped with thioglycerol, were centrifuged and washed several times using distilled water and ethanol. Then the products were dried in vacuum oven at a temperature of about 60^{o}C. The dried flakes were crushed in agate pestle and mortar till very fine powder was obtained. This powder was collected in airtight containers and was used for further characterization. Similarly synthesis of ZnS with other capping agents such as thiophenol and mercaptoethanol was carried out (Table 3.1).

Reaction mechanism: The nanocrystals growth through colloidal chemistry is a classical model. It describes the resultant nanocrystals by the formation of tiny crystalline nuclei in a supersaturated solution followed by crystal growth. The later processes were performed by mass supply of precursor monomers and by surface energy equilibrium on which addition or removal of the individual monomers at sites depends. Within a colloid solution system, the larger particles grow at the dissolution of the smaller ones as shown in Fig. 3.2. This mechanism is termed as Ostwald ripening, which is generally believed to be the main route of crystal growth [128]. This thermodynamically-driven spontaneous process occurs because larger particles are more energetically favored than smaller particles [129]. This stems from the fact that molecules on the surface of a particle are energetically less stable than the ones already well ordered and packed in the interior. Large particles with their lower surface to volume ratio, results in a lower energy state (lower surface energy). As the system tries to lower its overall energy, molecules on the surface of a small (energetically unfavorable) particle tends to detach and diffuse through solution and then attach to the surface of the larger particle. Therefore, the number of smaller particles continues to shrink, while larger particles continue to grow.

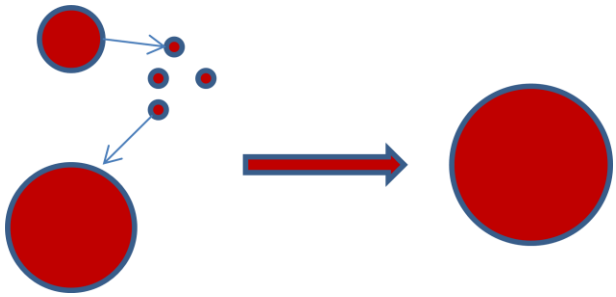

Figure 3.2 Basic schematic of the Ostwald ripening process

An integral part of any synthesis procedure to prepare nanocrystallites is the use of stabilising agents. These have to be present during growth to prevent aggregation and precipitation of the nanocrystallites. When the stabilising molecules are attached to the nanocrystallite surface as a monolayer through covalent, dative, or ionic bonds they are referred to as capping groups **[**130]. These capping groups mediate nanocrystalline growth, sterically stabilise nanocrystals in solution and passivate surface electronic states in semiconductor nanocrystals. This surface capping is analogous to the binding of ligands in a more traditional coordination chemistry. Synthetic organic techniques allow the tail and head groups to be independently tailored through well-established chemical substitutions.

Following is the reaction mechanism for the synthesis process of ZnS nanoparticles:

$$n(C_4H_6O_4Zn.2H_2O) + n(Na_2S) \rightarrow (ZnS)_n$$

$$TG + (ZnS)_n \rightarrow TG(ZnS)_n$$

Zinc acetate and sodium sulfide dissociate into their respective ions when dissolved in de-ionized water. Nucleation growth of ZnS nanoparticles starts due to reaction between Zn^{2+} and S^{2-} ions. The growth mechanism can be explained on the basis of Ostwald ripening. The chemical potential of the smaller nanoparticles is higher as that of the larger ones. Due to this, the large nanoparticles grow at the expense of the smaller ones. To avoid further growth, nanoparticles are capped with thioglycerol which acts as a

barrier by inducing steric hindrance [131], and consequently uniform shape, size, and stable nanoparticles are achieved. The schematic illustration for the synthesis of ZnS nanoparticles capped with thioglycerol has been shown in Fig. 3.3.

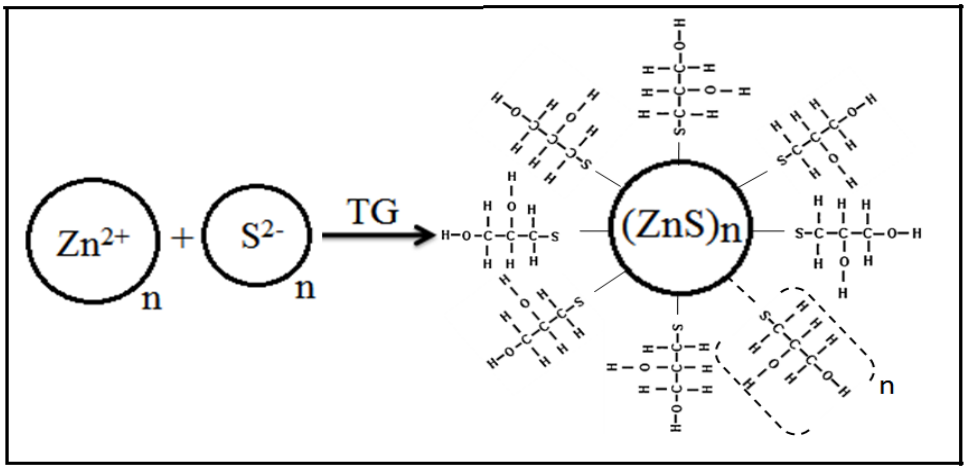

Figure 3.3 Preparative scheme of the surface-functionalized ZnS nanoparticles–polymer nanocomposites via in situ bulk polymerization

Table 3.1 List of the synthesized samples with different capping agent

Sample Type	Capping agent	Capping concentration (By volume %)
ZnS	None	None
ZnS	Thiophenol	0.25, 0.50, 0.75, and 1.00
ZnS	Mercaptoethanol	0.25, 0.50, 0.75, and 1.00
ZnS	Thioglycerol	0.25, 0.50, 0.75, and 1.00

Reflectance has been checked for all the samples and it comes out to be maximum for samples capped with thioglycerol (Chapter 4, section 4.6).

Therefore, in the present thesis work thioglycerol has been used for the passivation of ZnS surface.

3.4 Synthesis of TiO_2

Nowadays, the scientific studies in material engineering are focused on application oriented research. It has been found that TiO_2 is commercially very important reflective pigment because of its maximum light scattering with virtually no absorption. Anatase and rutile phase TiO_2 particles are manufactured in the chemical industry as white pigments. Rutile phase TiO_2 is characterized by the high thermodynamic stability, packing fraction and refractive index. The pigment properties of rutile phase TiO_2 are better than that of anatase phase. Bulk particles of TiO_2 are mainly manufactured by two processes: i.e., sulfate process and chloride process. In the former, processing is very complicated and the later one requires complicated instruments [132]. Both of the processes are costly, time consuming and demand high reaction temperature. The particles obtained with these processes are non-uniform in shape and size as well as contain impurities [86].

Nanocrystalline TiO_2 particles from the point of view of applications have very good structural, optical, electrical and chemical properties. The morphology of TiO_2 nanoparticles significantly affects these properties, so a great effort has been made in the development of innovative processes for obtaining the nanosized particles. Several methods and technologies have been developed in recent years for obtaining nanosized particles, such as solvolthermal, microemulsion, colloidal, thermal plasma, hydrolysis, coprecipitation, combustion, thermo-hydrolysis, micelle and inverse micelle, sol, hydrothermal, direct oxidation, chemical vapor deposition, physical vapor deposition, sono-chemical, microwave method, sol-gel [49, 50] .

Fine spherical TiO_2 nanoparticles with high specific surface area were prepared by hydrolyzing titanium tetraisopropoxide with water [133]. Synthesis of TiO_2 particles in the range of 20-60 nm from the thermal decomposition of titanium isopropoxide in supercritical alcohol at 573K and 10MPa have been reported [134]. Influence of preparation variable, such as reaction temperature and time, precursor's molar ratio on TiO_2 particle size and morphology has been reported [135]. Anuradha et al. reported the comparison of the efficiency of three different synthetic routes viz. sol–gel method involving templating, mechano-chemical, synthesis and combustion synthesis for the production of nanostructured TiO_2. In their study, nanostructured TiO_2 with an average particle size of ~ 14 nm is produced by the sol–gel method whereas in the mechano-chemical the formation of nanocrystalline TiO_2 with an average particle size of ~ 20 nm and combustion synthesis resulted in the formation of nanocrystalline TiO_2 with an average particle size of less than ~ 50 nm [136]. Wang et al. investigated the preparation of nanocrystalline TiO_2 powder by solution combustion method, optimizing the process condition by employing Taguchi robust design method [137].

Among the various synthesis techniques, the sol-gel technique has received more attention due to ease of controlling various material parameters such as particle morphology, surface area, average nanocrystallite size, crystallinity and phase structure, which significantly affects the reflective properties of nanocrystalline TiO_2. It has been reported that the nanocrystalline metal oxide could be synthesized with different average size, morphology and phase structure by varying the sol-gel processing parameters such as ratio of number of moles of water to alkoxide precursor as well as with calcination temperature. Sol-gel method offers low cost and large scale production of TiO_2 nanoparticles.

Study of reflective properties of titania nanoparticles have been reported by many researchers. Karvinen synthesised and characterised the optical properties of titania nanoparticles and reported their reflectance in the range of 97-99%, in the visible region

[48]. Mechanism of reflectance by an isolated particle can be studied by Mie theory [138]. Reflectance depends upon the refractive index, band gap, shape, size, and surface characteristics of the particles [138, 139]

3.5 Introduction to sol-gel

The sol-gel process is a versatile solution process for making metal oxide, ceramic and glass materials. The sol-gel process, as the name implies, involves the evolution of inorganic networks through the formation of a colloidal suspension (sol) and gelation of the sol to form a network in a continuous liquid phase (gel). A sol is dispersion of the solid with diameter of 1-1000 nm in a liquid where only the Brownian motions keeps particles in suspension [140]. While gel is a state where both liquid and solid are dispersed in each other, which presents a solid network filled with liquid components. The precursors for synthesizing these colloids consist of a metal or metalloid element surrounded by various reactive ligands. Metal alkoxides are most popular because they react readily with water. The starting material is processed to form a dispersible oxide and forms a sol in contact with water or dilute acid. Removal of the liquid from the sol yields the gel and the sol to gel transition controls the particle size and shape. Calcination of the gel produces oxide. At the functional group level, three reactions are generally used to describe the sol-gel process: hydrolysis, alcohol condensation, and water condensation. However, the characteristics and properties of a particular sol-gel inorganic network are related to a number of factors that affect the rate of hydrolysis and condensation reactions, such as, pH, temperature and time of reaction, reagent concentrations, catalyst nature and concentration, H_2O/MO molar ratio (L), aging temperature and time, and drying [49]. Thus, by controlling these factors, it is possible to vary the structural and optical properties of the sol-gel-derived inorganic network over wide ranges.

3.6 Synthesis and reaction mechanism of TiO_2 nanoparticles

Sol-gel technique has been used to synthesize TiO_2 nanoparticles at room temperature [67]. Fig. 3.4 shows the schematic illustration of the sol-gel technique.

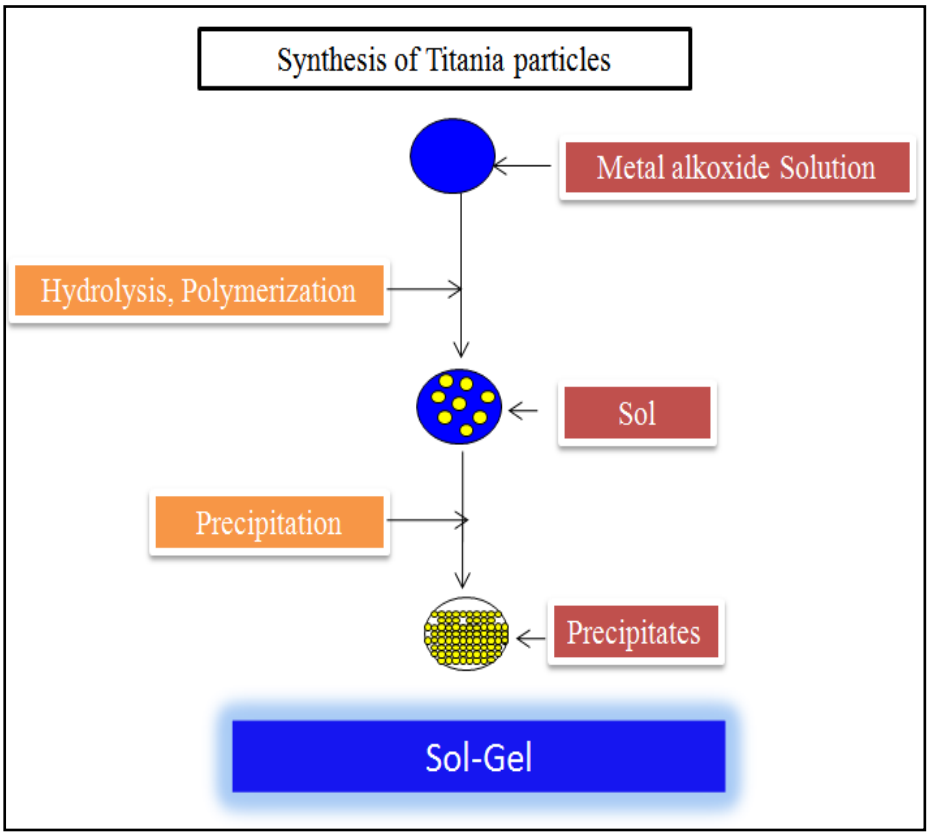

Figure 3.4 Schematic illustration of Sol-gel technique to synthesize TiO_2 nanoparticles

Titanium isopropoxide $Ti\{OCH(CH_3)_2\}_4$, anhydrous 2-propanol (C_3H_8O) and distilled water were used, without any further purification.

In a typical experiment, titania isopropoxide was dissolved in 100 ml of anhydrous 2-propanol (0.4 M). A measured quantity of distilled water was mixed with 100 ml of anhydrous 2-propanol to prepare a second solution. Both the solutions were covered and stirred for 45 minutes using magnetic stirrer. With the help of a burette, the water solution was added drop-wise to the first solution under constant magnetic stirring

for another 6 hours. As a result of hydrolysis of titania isopropoxide, the color of solution changed from transparent to white indicating the formation of precipitates. Different solutions were prepared by varying the L (ratio of molar concentration of water to that of alkoxide precursor) within the range of 20 -50.

The reaction of hydrolysis of the titania isopropoxide proceeds as follows:

$$Ti(C_3H_7O)_4 + (2+n)H_2O \rightarrow TiO_2.nH_2O + 4C_3H_7OH$$

The precipitates were filtered and dried in an oven at 60°C for 8 hours; after crushing in pestle and mortar, powder of titania was obtained. The dried powder was then calcined at 350°C, 550°C, 750°C and 900°C for 15 minutes to remove the solvent completely as well as to crystallize the amorphous titania powder.

Reaction mechanism: In a typical sol-gel process, a colloidal suspension (sol) is formed from the hydrolysis and polymerization reaction of the precursors, which are usually inorganic metal salts or metal organic compounds such as metal alkoxide. A wet gel is formed on further drying. Three main reactions occur during the sol-gel process: hydrolysis, alcohol condensation and water condensation [140].

The reactions are as follows:

$$Ti - OR + H_2O \rightarrow Ti - OH + R - OH \qquad \text{Hydrolysis}$$

$$Ti - OH + RO - Ti \rightarrow Ti - O - Ti + R - OH \qquad \text{Alcohol condensation}$$

$$Ti - OH + HO - Ti \rightarrow Ti - O - Ti + H_2O \qquad \text{Water condensation}$$

These processes normally proceed via an acid-catalyzed hydrolysis of titania isopropoxide. The development of Ti-O-Ti chains is favoured with low content of water, low hydrolysis rates and excess titania isopropoxide in the reaction mixture. Three

dimensional polymeric skeletons with close packing results from the development of Ti-O-Ti chains. The formation of $Ti(OH)_4$ is favoured with high hydrolysis rates for medium amount of water. The presence of large amount of Ti-OH and insufficient development of three-dimensional polymeric skeletons lead to loosely packed first order particles. From the study on the growth kinetic of TiO_2 nanoparticles using titania isopropoxide as a precursor it is found that the rate constant for coarsening increases with temperature. Second particles are formed by epitaxial self-assembly of primary particles at longer times and higher temperature, and the number of particles per secondary particles increases. The average TiO_2 nanoparticles radius increases with Lifshitz Slyozov-Wagneer model for coarsening [50].

3.7 Preparation of coating materials

Coating materials were prepared by dispersing ZnS/TiO_2 nanoparticles and acrylic binder (VISYCRYL- 8350, purchased from N. R. Chemicals Pvt. Ltd, India) in de-ionized water, using planetary ball mill. Fig. 3.5 shows the the scheme for preparation of the coating material.

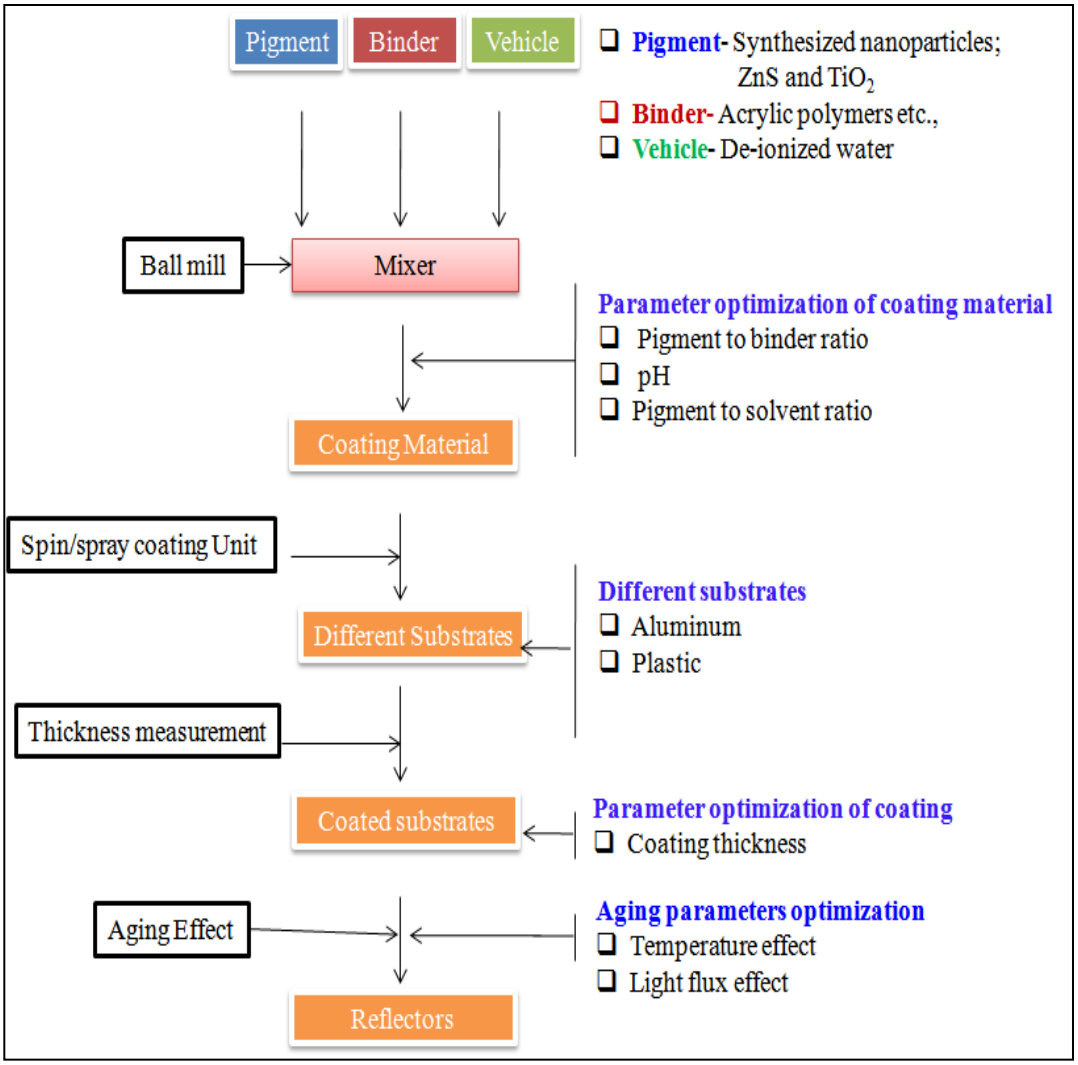

Figure 3.5 Preparation of coating material and reflectors

For the preparation of coating material, acrylic has been chosen as a binding material. Acrylic has gained a strong foothold in the coatings due to its higher flexibility, easy adhesion and resistance to ultraviolet degradation as compared to the other emulsions and latex [141]. The amount of acrylic in the coating material is adjusted so as not to affect the thermal and mechanical properties of the reflective coating. Another parameter, which is important in the preparation of coating materials, is pH. The adjustment of pH is important in order to maintain stable pigment dispersion, reduce biological growth and, in general, to optimise the performance of coating material during

storage and application. In the present studies, the pH of the coating material has been adjusted in-between 6 to 8.

(a) Coating material based on ZnS nanoparticles: Coating materials were prepared by dispersing ZnS nanoparticles capped with 0.5 ml of thioglycerol in a de-ionized water solution of organic binder with different pigment to binder weight ratios (Table 3.2). In typical experiment, 2.0 g of ZnS/thioglycerol nanoparticles, 0.24 g of product VISYCRYL- 8350, and 4.0 g of de-ionized water were mixed using PM 100 Planetary Ball Mill, for 5 minutes at 800-1000 rpm. The pH of the coating material was adjusted to 6 to 7 depending on the type of substrate on which it is applied, i.e., aluminium or plastic.

Table 3.2 Preparation of different coating materials with different pigment to binder weight ratio

Coating material	Pigment to binder weight ratio (%)	Pigment to solvent weight ratio (gm)
ZnS: A	8.3:1 (12%)	1:2
ZnS: B	7.1:1 (14%)	1:2
ZnS: C	6.1: 1 (16%)	1:2

(b) Coating material based on TiO_2 nanoparticles: Coating materials were prepared by dispersing TiO_2 nanoparticles in de-ionized water solution of organic binder with different pigment to binder weight ratios (Table 3.3). Particularly, 2.0 g of TiO_2, 0.24 g of product VISYCRYL- 8350, and 4.0 gm of de-ionized water were mixed using PM 100 Planetary Ball Mill, for 5 minutes at 800-1000 rpm. The pH of the coating material was adjusted to 6 to 8 depending on the type of substrate on which it is applied, i.e., aluminium or plastic.

Table 3.3 Preparation of different coating materials with different pigment to binder weight ratio

Coating material	Pigment to binder weight ratio (%)	Pigment to solvent weight ratio (gm)
TiO_2 :A	8.3:1 (12%)	1:2
TiO_2 :B	7.1:1 (14%)	1:2
TiO_2 :C	6.1: 1 (16%)	1:2

3.8 Development of reflectors

(a) **For aluminium substrate:** The scheme for the development of reflectors is also shown in Figure 3.5. The aluminium sheets, each of size (2cm x 2cm) and thickness, 0.25 mm, were mechanically cleaned by sand paper, thereafter ultrasonically in ethanol, and then dried in an oven at 60°C. The cleaning of the sheets is very important to ensure that the coating material meets the required quality standards for appearance, adhesion and corrosion resistance [23]. These sheets were spray coated with the coating material having different pigment to binder weight ratio (Table 3.2 and Table 3.3) and with different thicknesses. For better resistance to corrosion and adhesion of coating material to the substrate, a thin layer of acrylic polymer was applied on the sheets before spraying the coating material. Layer by layer coating was done, to develop reflectors. During this process, it was ensured that the second layer of the coating material was applied before the glossy appearance of the first layer disappeared.

(b) **For plastic substrate:** Plastic sheet (2cm x 2cm), having thickness of 1 mm was used as substrate, mechanically sanded, cleaned using detergent, rinsed with de-ionized water and isopropyl alcohol [23]. These sheets were spray coated with the coating material with different thicknesses. Before applying the coating material, a thin layer of binder was applied to the substrate for better adhesion. The coating was done by spreading one layer over the other to develop reflectors; care was taken to apply the second layer before the glossy appearance of the first layer disappeared.

Chapter 4

Results and discussion

Proper analysis of the results is the most important factor for their successful discussion. For the proper analysis, the results must be supported by the physics behind them. It is equally important to see that the results are supported or refuted by the hypothesis/phenomenon. This chapter deals with structural, morphological and optical characterization of synthesized ZnS and TiO_2 nanoparticles using XRD, SEM, TEM, FTIR, PL, UV-Vis, DRS along with optical characterization of their reflective coatings using DRS. To check the durability of the reflective coatings, the reflectors have been exposed to different temperatures as well as illuminations and their diffuse reflectance has been investigated.

4.1 Phase detection and structural analysis of ZnS

Fig. 4.1 shows the XRD patterns of synthesized uncapped and thioglycerol capped ZnS nanoparticles. The three prominent peaks are observed at 2θ values of 29.03, 48.06, and 56.11. Lattice planes corresponding to these peaks have been identified by applying extinction rules [142]. As given in Table 4.1, the peaks have been found to correspond to the ZnS planes (111), (220) and (311).

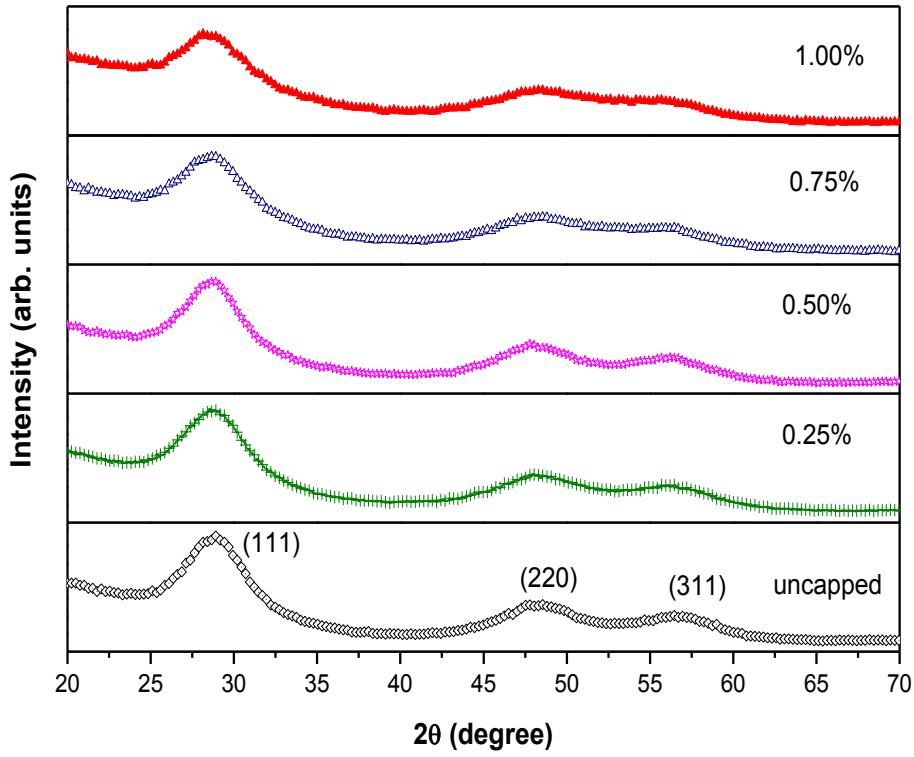

Figure 4.1 XRD pattern of ZnS nanoparticles capped with different concentration of thioglycerol

On comparison with the standard sample (JCPDS card #050566), 2θ values as well as hkl plane of synthesized ZnS particles were found to be in fairly good agreement; confirming the zinc blende crystal phase. The zinc blende phase of ZnS is thermodynamically favorable at low temperatures [119]. The broad diffraction peaks indicate that the product is composed of many tiny crystallites. The broadening in the diffraction peaks is due to size and strain effect. Ignoring the lattice strain in the nanocrystallites, owing to their negligible value (0.07) (Equ.2.6), the crystallite size of ZnS nanoparticles has been calculated using Debye Scherrer's equation (2.2).

The crystallite size has been determined from the full width at half maximum (FWHM) of the most intense peak (Fig. 4.1) shown in Table 4.2. FWHM has been

calculated using Lorentz best fit curve (R^2 > 0.98) method. No diffraction peaks from other crystalline forms were detected, indicating the high purity of the synthesized ZnS.

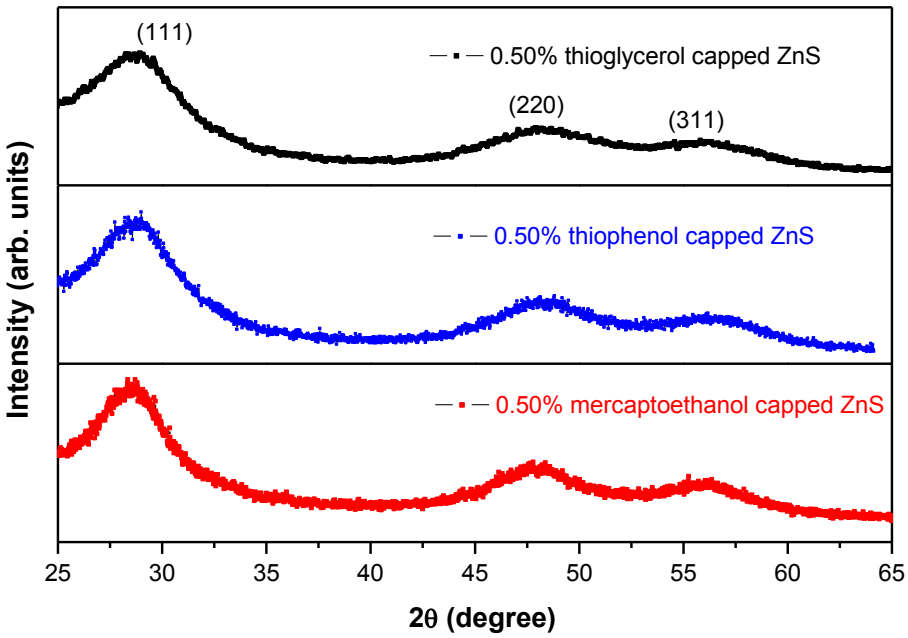

Figure 4.2 XRD pattern of ZnS nanoparticles capped with different capping agents

As observed in Table 4.2, the capping concentration affects the crystallite size of the synthesized particles. It has been reported that the nature of capping agent also affects the crystallite size of particles [124, 114] and to observe that effect, ZnS particles capped with thiophenol, mercaptoethanol and thioglycerol were synthesized. Fig. 4.2 shows the XRD patterns of ZnS particles capped with three different capping agents. It reveals that ZnS particles exhibit characteristic peaks of zinc blende crystal phase (29.03, 48.06, and 56.11) (JCPDS card #050566). The crystallite size as explained above has been determined and shown in Table 4.3. ZnS particles capped with 0.50% of thioglycerol shows the smallest crystallite size as observed in Table 4.3.

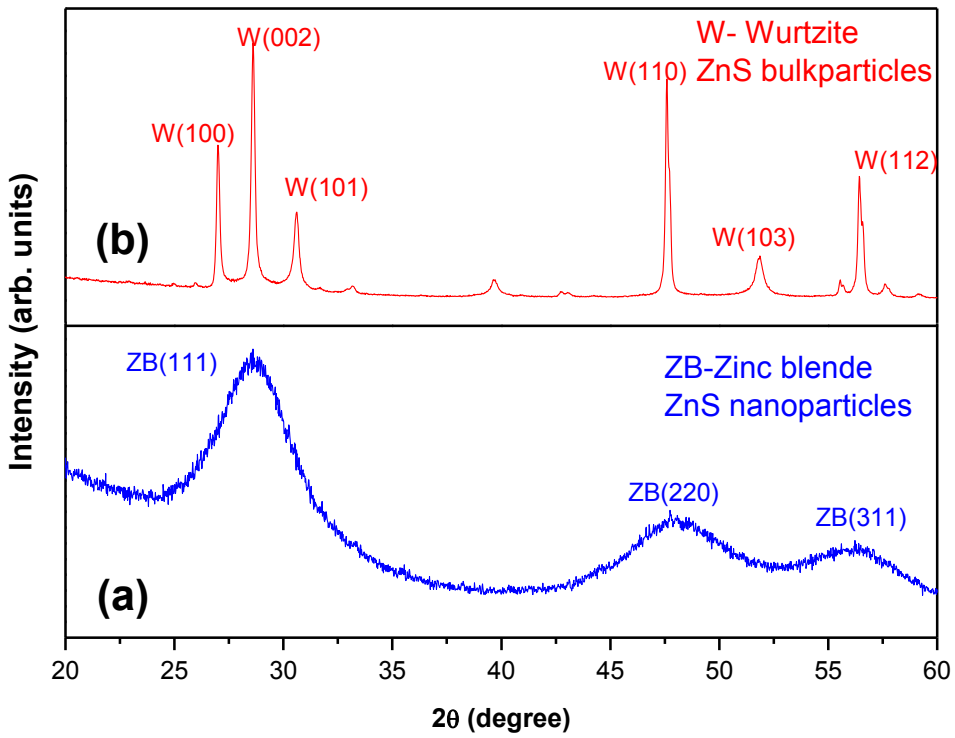

Figure 4.3 XRD pattern of (a) thioglycerol capped ZnS nanoparticles (b) bulk ZnS particles

X-ray diffraction patterns of synthesized ZnS nanoparticles capped with thioglycerol and bulk ZnS particles are shown in Fig. 4.3. This reveals that synthesized ZnS nanoparticles (Fig. 4.3(a)) exhibit a cubic-zinc blende crystal structure, which is the stable phase at room temperature. The three diffraction peaks correspond to (111), (220) and (311) planes of the cubic crystal ZnS, respectively. Due to the size effect, the XRD peaks broaden and their widths become larger as the crystals become smaller. The crystallite size of the synthesized sample (calculated from XRD) was 10.67 nm. The wurtzite structure of the bulk ZnS sample was clearly visible in the X-ray diffraction pattern (Fig. 4.3(b)). In Fig. 4.3(b), the wurtzite (100) and (101) peaks are next to the zinc blende (111). It is known that the corresponding bulk zinc blende-to-wurtzite phase transition temperature is 1020°C [143]. It has been observed that synthesis of ZnS

nanoparticles by chemical precipitation technique at room temperature, lead to formation of zinc blende crystal structure.

Table 4.1 Determination of lattice structure of ZnS from X-ray diffraction

2θ	$\sin\theta$	$\sin^2\theta$	$\sin^2\theta/\sin^2\theta_{min}$	Normalized ratios	Lattice planes
29.03	0.251	0.063	1.00	3	(111)
48.03	0.407	0.166	2.63	$7.89 \approx 8$	(220)
56.11	0.470	0.220	3.49	$10.57 \approx 11$	(311)

Table 4.2 Nanoparticle-crystallite size variation with capping concentrations

Sample name	Sample/capping concentration (By volume %)	Crystallite size (nm)
(a)	ZnS uncapped	17.20
(b)	ZnS : 0.25	16.95
(c)	ZnS : 0.50	15.85
(d)	ZnS : 0.75	16.66
(e)	ZnS : 1.00	17.05

Table 4.3 Nanoparticle-crystallite size variation with different capping agents

Sample name	Samples (By 0.50% volume)	Crystallite size (nm)
(a)	ZnS : thioglycerol	10.67
(b)	ZnS: thiophenol	11.01
(c)	ZnS: mercaptoethanol	14.84

4.2 Microstructural analysis of ZnS

The size and morphology of ZnS nanoparticles were investigated by TEM. Different capping agents were utilized to control the size and morphology of nanomaterials in various physical and chemical processes [124]. In the present study, the thioglycerol was used to control the size and morphology of ZnS by chemical precipitation method at room temperature.

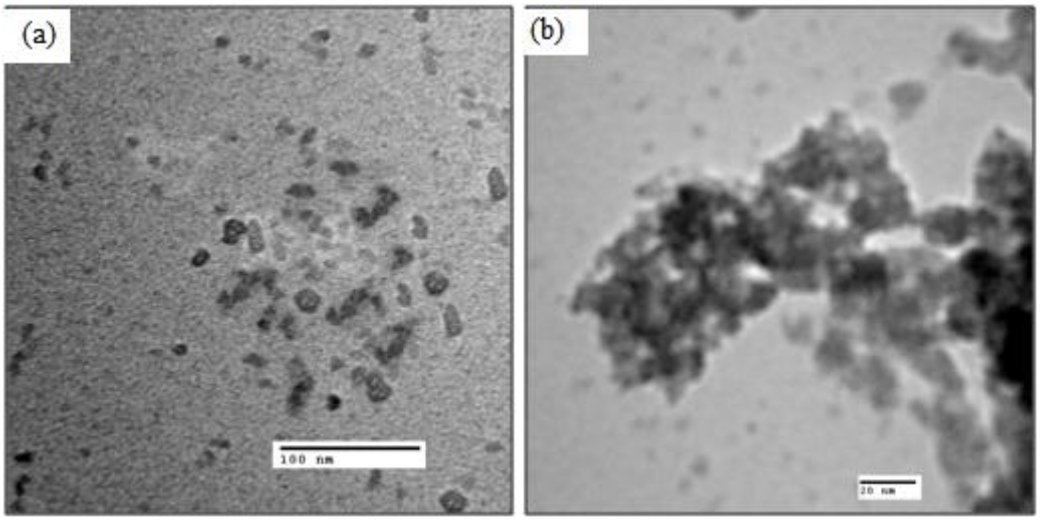

Figure 4.4 TEM micrographs of uncapped ZnS nanoparticles (a) low magnification (b) high magnification

Fig. 4.4(a) shows the distribution of ZnS nanoparticles with different shapes and sizes. Fig. 4.4(b) shows the high magnification TEM micrograph of uncapped ZnS nanoparticles. It reveals that the uncapped particles get aggregated and coalesce non-uniformly due to their high surface energy in the absence of surfactant. This result indicates that, initially, loose cores were formed due to the relatively high reactant concentration at the beginning of the reaction. When a larger number of crystallites are simultaneously generated at the beginning of the reaction, they would tend to aggregate together due to Vander Waals forces [119]. These crystallites grow gradually at the expense of the inner cores via Ostwald ripening, resulting in the formation of the final agglomerated particles. The whole process can be called a 'cluster-by-cluster' growth mode that is different from the 'atom-by-atom' growth mode happening to most of the crystals [114]. The average diameters of these particles were found to be in the range 20 - 30 nm.

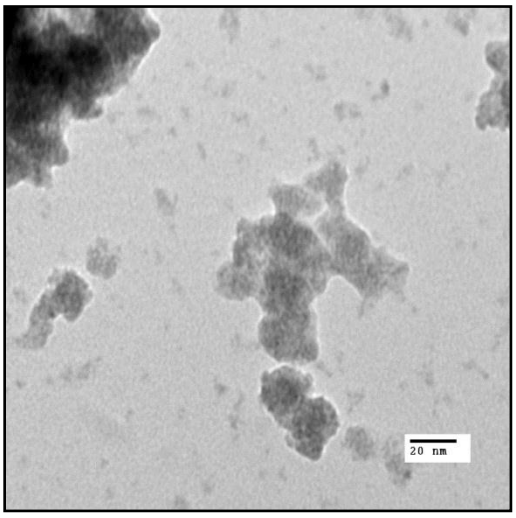

Figure 4.5 TEM micrographs of 0.25% thioglycerol capped ZnS nanoparticles with high magnification

Fig. 4.5 shows the TEM micrographs of 0.25% thioglycerol capped ZnS nanoparticles. It was observed that the nanoparticles were agglomerated and distributed

nonuniformly. This might be due the low concentration of capping agent. The average diameters of these particles were found to be in the range of 20 - 30 nm.

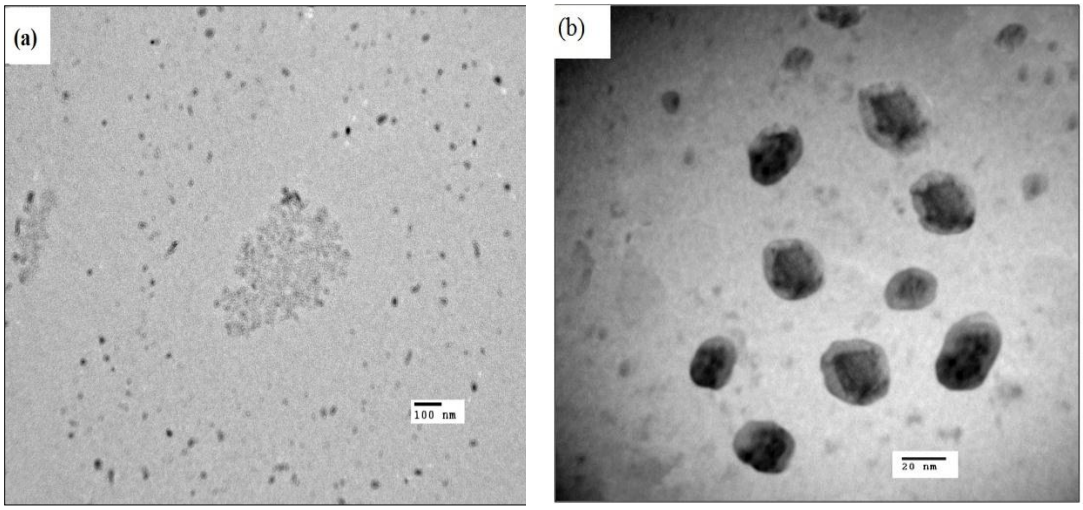

Figure 4.6 TEM micrographs of 0.50% thioglycerol capped ZnS nanoparticles with (a) low magnification (b) high magnification

Fig. 4.6(a) shows the TEM micrographs of 0.50% thioglycerol capped ZnS nanoparticles with low magnification. It reveals that surface passivation of the ZnS nanoparticles with 0.50% thioglycerol leads to high degree of mono-dispersity as well as spherical symmetry. The nanoparticles so obtained were nearly spherical with size, 15 - 28 nm, comprising of core of 15 - 20 nm size and shell (thioglycerol layer) thickness of 5 - 8 nm (Fig. 4.6(b)). Such core/shell type structures may change the optical properties of the materials [145].

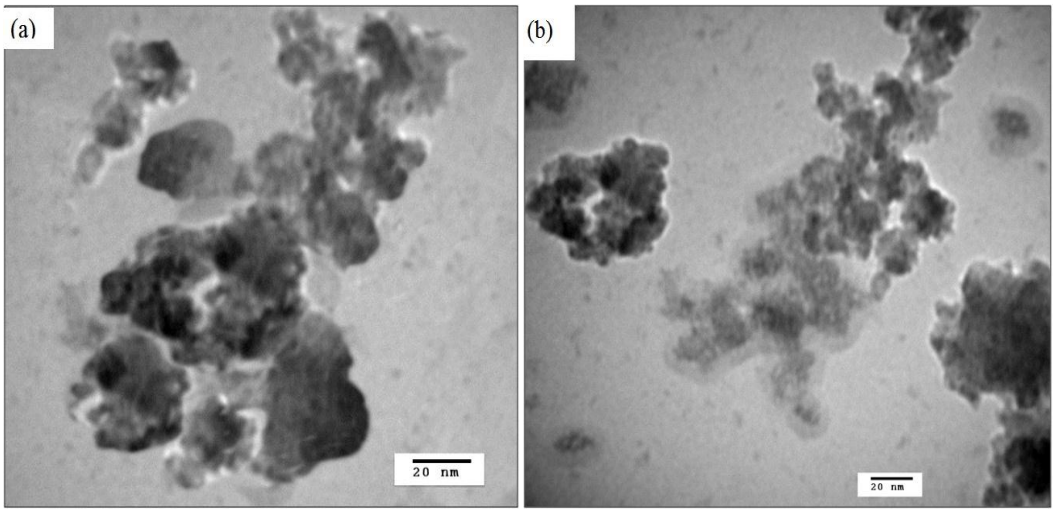

Figure 4.7 TEM micrographs of ZnS nanoparticles capped with (a) 0.75% thioglycerol (b) 1.00% thioglycerol

Fig. 4.7(a) and (b) show the TEM micrographs of ZnS nanoparticles capped with 0.75% and 1.00% of thioglycerol. The increase in surfactant concentration i.e. 0.50% to 0.75% or from 0.75% to 1.00%, results in agglomeration of the ZnS nanoparticles. The average diameters of these particles were found to be 20 - 30 nm.

The nanostructure observed from TEM shows that capping affects the size as well morphology of the particles. Uncapped particles get aggregated and coalesce non-uniformly. With increase in the capping concentration of thioglycerol, 0 to 0.50%, ZnS nanoparticles show a high degree of mono-dispersity as well as spherical symmetry. With further increase in the capping concentration, the particles are again aggregated and coalesce. Therefore, the kinetic-controlled mechanism is easily affected by the concentration of thioglycerol.

4.3 FTIR analysis of ZnS

Fourier transform infrared spectroscopy is a powerful tool for identifying different types of chemical bonds in a molecule by producing an infrared absorption spectrum that

is like a molecular fingerprint. FTIR spectroscopy was carried out for uncapped and capped ZnS nanoparticles with different concentration of thioglycerol and the presence of thioglycerol groups on the surface of ZnS nanoparticles was examined.

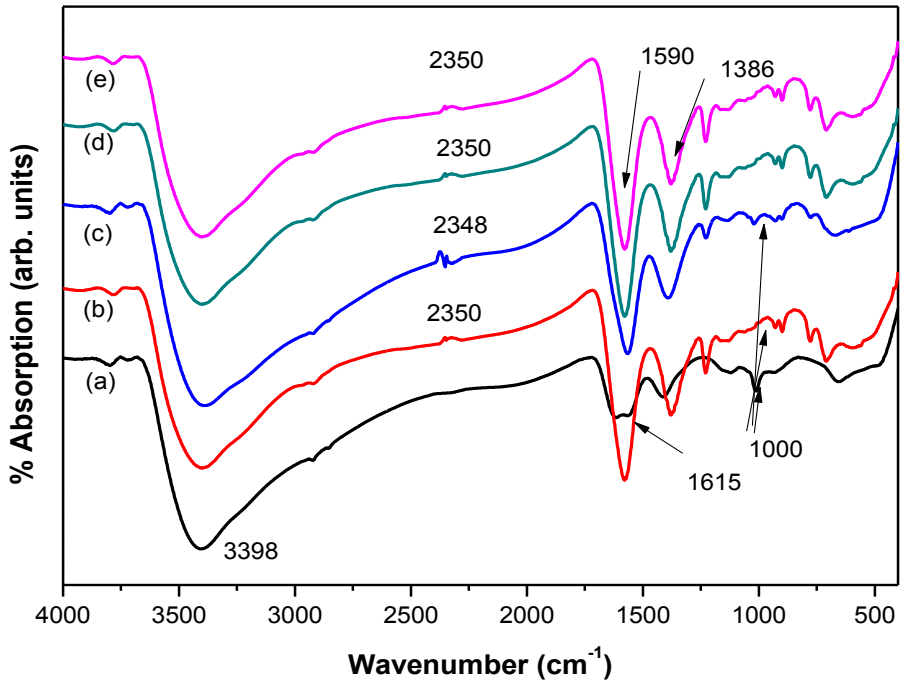

Figure 4.8 FTIR spectra of (a) uncapped (b) 0.25% (c) 0.50% (d) 0.75% (e) 1.00 % ml thioglycerol capped ZnS nanoparticles

Fig. 4.8 shows the FTIR spectra for uncapped and capped ZnS nanoparticles. A broad intermolecular hydrogen bonded O–H stretch occurs around 3398 cm^{-1} in the curve (a) to (e); all FTIR spectra were carried out by mixing ZnS nanoparticles with KBr, hence there is some adsorbed water vapor due to hygroscopic nature of KBr. The features ranging from 3520 to 3200 cm^{-1} are due to free hydroxyl band (O–H). A weak band around 2350 cm^{-1} was observed for the capped ZnS nanoparticles. This weak band in the

high frequency region, results from the fundamental absorption of S-H group. The S-H stretching band is characteristically weak and may go undetectable in the most of the cases [146]. The peaks in the wide range from 2000 to 1300 cm^{-1} can be assigned to O-H group, as no other functional group from aliphatic chains falls in this region. The peak around 1615 cm^{-1} for uncapped ZnS is due to H-O-H vibration. It shows that water in the sample was not evaporated completely. This value is identical to that for pure liquid water, as reported earlier [147]. A high absorption peak near 1590 cm^{-1} might be due to the presence of carboxylate ion. This peak shows that the acetate group from the zinc acetate precursor used for zinc ions, have been retained in the synthesized nanoparticles. The weak band appearing at 1386 cm^{-1} may be attributed to O-H bending in carboxylic acids. It might be due to O-H in-plane bending vibrations in alcohols. The group of peaks around 1000 cm^{-1} is indicative of sulfate groups [146]. The peaks in the range of 400-600 cm^{-1} can be assigned to S-S bonds in case of capped nanoparticles. As the peak of stretching band around 2350 cm^{-1} of S-H is very weak and most of S-H bonds break and this leads to formation of S-S bonds in the 400 to 600 cm^{-1} region.

From the FTIR data, the description of the surface of nanoparticles has been derived. The observation of S-H group in the spectra for sample (b) to (e) indicates that thioglycerol is bound electrostatically to the surface of zinc atoms, without formation of covalent thiol bonds to the surface of sulfur atoms.

4.4 Absorbance analysis of ZnS

Particle size and size distribution are critical in maximizing enhancement in quantum-confined systems. The particle size affects the magnitude of the shift in absorption (change in bandgap), while the distribution affects the strength of the quantum effect at a given wavelength. These properties can be controlled with the help of surface passivation of nanoparticles by varying the capping agent concentration. Fig. 4.9 shows the optical absorption spectra of ZnS nanoparticles capped with different concentration of

thioglycerol. The nature of transition (explained in section 2.3.6.3) is determined by using the relation (2.11) [104]:

$$\alpha = \frac{A}{h\nu\left[h\nu - E_g\right]^n} \qquad (2.11)$$

Where $h\nu$ is the photon energy; Eg the band gap energy; A and n are constants. These transitions are very important to study the reflective behavior of any reflective material. According to band theory a specific minimum energy is required to excite electrons across the energy gap from the valence band to the conduction band. This has important consequences for color. If the substance has a large band gap (> 3eV), then, no light in the visible spectrum is absorbed. These substances transmit incident light, and are colorless in their pure forms; in their powdered form, the light reflects back and they appear as white.

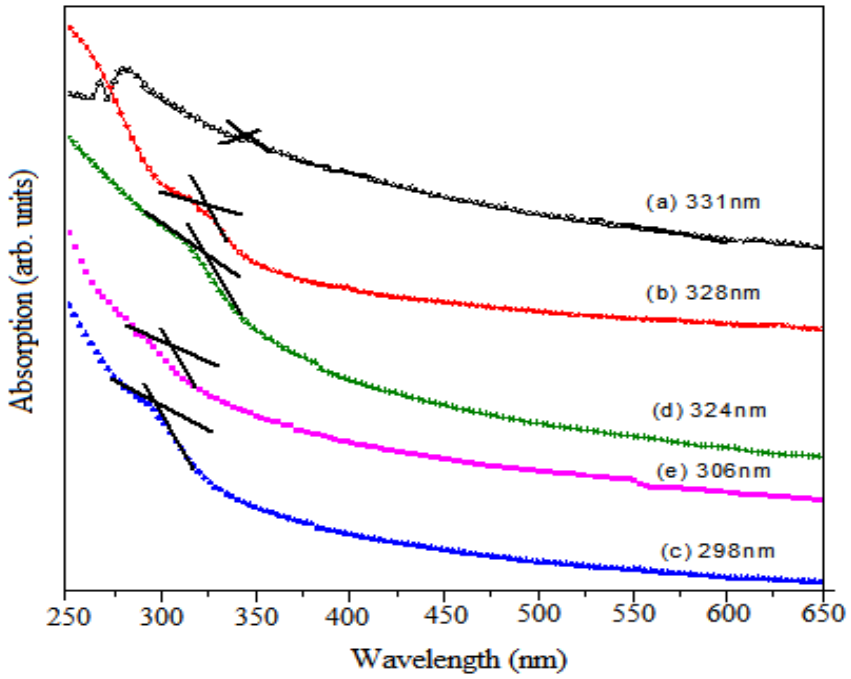

Figure 4.9 UV-Vis absorption spectra of ZnS nanoparticles (a) uncapped, and thioglycerol capped (b) 0.25% (c) 0.50% (d) 0.75% (e) 1.00%

The optical absorption spectra of ZnS nanoparticles (Fig. 4.9) show blue-shift in the absorption edges for ZnS nanoparticles vis a vis the bulk ZnS particles (Eg = 3.68 eV), indicating the ZnS particles are in the range of the nanometer region. The band gap energy values of uncapped and capped nanoparticles (Table 4.4) were also found to be higher than those of the bulk ZnS particles, as calculated from the UV-visible absorption spectra (Fig. 4.9) [124]. With increase in the capping concentration, 0 - 0.50 %, the energy band gap increases. But, for further increase in capping concentration, 0.75 - 1.00%, the energy band gap decreases. This blue shift is due to the quantum confinement effects [129].

Table 4.4 Determination of band gap energy of ZnS nanoparticles

Sample name	Sample/capping concentration (By volume %)	Band gap energy (eV)
(a)	ZnS uncapped	3.74
(b)	ZnS : 0.25	3.78
(c)	ZnS : 0.50	4.16
(d)	ZnS : 0.75	3.82
(e)	ZnS : 1.00	4.05

4.5 Photoluminescence analysis of ZnS

Fig. 4.10 shows the PL spectra of uncapped and capped ZnS nanoparticles at an excitation wavelength of 370 nm. A broad luminescent peak at about 426 nm is observed for all the samples. This blue emission band is associated with the recombination of free charge carriers at defect sites, possibly at the surface of nanostructures and it is attributed to S^{2-} ion vacancies [148]. PL spectrum also exhibits peaks centered at 485 and 515 nm because of band-edge emission and interstitial zinc vacancy related defects [149].

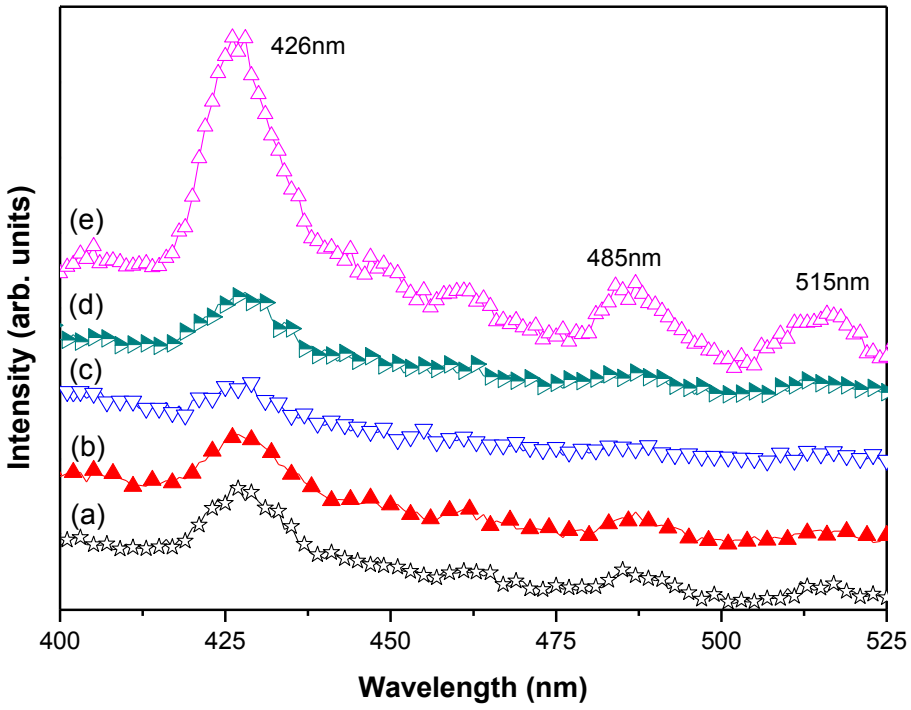

Figure 4.10 Room temperature photoluminescence emission spectra of ZnS nanoparticles (a) uncapped, and thioglycerol capped (b) 0.25% (c) 0.50% (d) 0.75% (e) 1.00%, at an excitation wavelength of 370 nm

Passivation of ZnS surface with thioglycerol does not leads to any significant change to luminescent bands. The mechanism of luminescence in semiconductors is shown in Fig 4.11. When a photon of energy higher than the band gap of the material is absorbed, an electron-hole pair is created. On a very short timescale the energy is thermalized so that the energy separation between the electron and the hole becomes approximately equal to the energy of the gap. Then the pair radiatively recombines, giving rise to the emission of a photon (luminescence) [150].

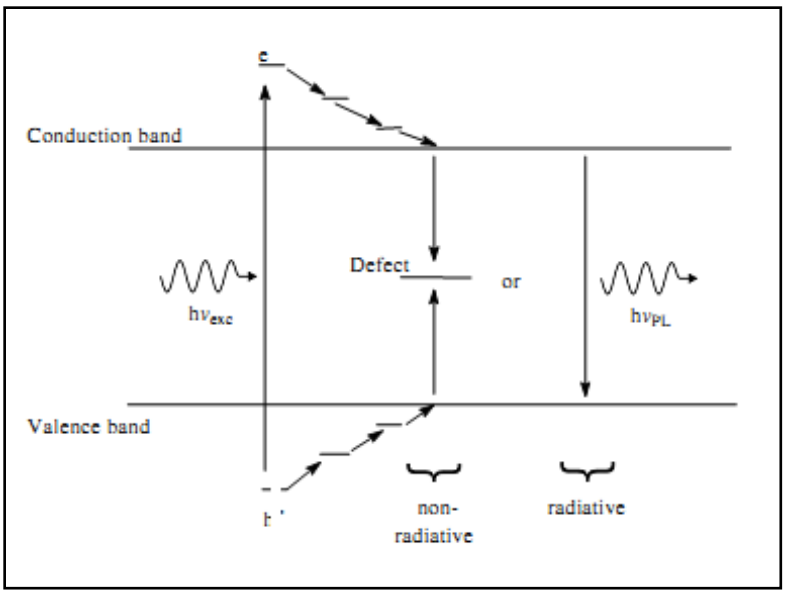

Figure 4.11 Diagram showing luminescence in semiconductors

The yield of photoluminescence is governed by competition between radiative and non-radiative recombination. The sources of non-radiative recombination are defects in the material (e.g. impurities and disorder sites in a crystal or dangling bonds on the surface). Therefore, the defects are said to quench the photoluminescence [151]. When the size is reduced to the nanometer scale the probability of non-radiative recombination decreases (if we assume that the density of defects due to impurities remain same). This is because the probability for the carriers to find a defect in the core is getting smaller. On the other hand, the number of surface atoms relative to the number of volume atoms increases with decreasing particle size. As a result, dangling bonds become more pronounced for nanoparticles. Since the dangling bonds represent traps for the carriers, the surfaces of nanoparticles must be completely passivated to avoid quenching the photoluminescence. For ZnS nanoparticles this can be achieved by passivating its surface with organic ligand such as thioglycerol.

4.6 Diffuse reflectance analysis of ZnS nanoparticles

Diffuse reflectance spectroscopy in the visible region is an effective and extensively used technique for the study and characterization of various reflective properties of materials and coatings as well as for determining color of materials and coatings.

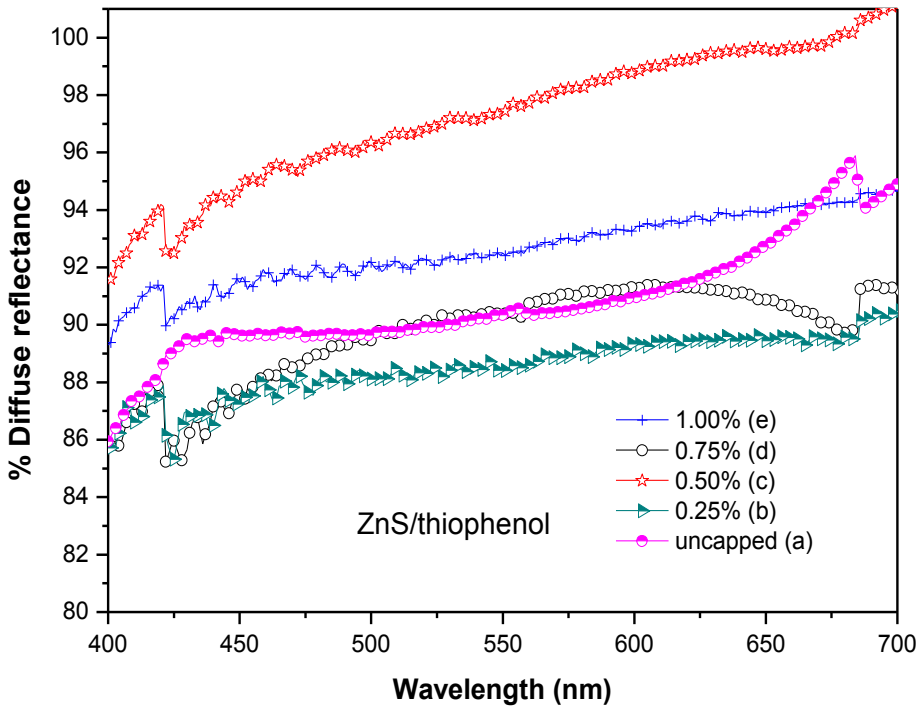

Figure 4.12 Diffuse reflectance spectra of ZnS nanoparticles (a) uncapped, and thiophenol capped (b) 0.25% (c) 0.50% (d) 0.75% (e) 1.00 %

The diffuse reflectance spectra of both uncapped and thiophenol capped ZnS nanoparticles are shown in Fig. 4.12. On increasing the capping concentration from 0 to 0.50 %, the diffuse reflectance increases, whereas, it decreases on further increase in concentration from 0.50 to 1.00%. These results show attainment of maximum diffuse reflectance (91.50 – 100%) for 0.50% thiophenol capped ZnS nanoparticles in the visible region. A small kink centered at 426 nm is observed in the diffuse reflectance spectra for

all the samples. This kink is due to the luminescent emission band associated with the recombination of free charge carriers at defect sites, attributed to S^{2-} ion vacancies as explained in PL analysis. The kink centered at 685 nm corresponds to the reflection from second order reflection of the fundamental intrinsic emission peak at 338 nm [152]. Another very consistent feature of the diffuse reflectance spectra of ZnS nanoparticles, shown in Fig. 4.12, is the decrease in reflectance with decreasing wavelength in the visible spectrum. This indicates that the ZnS nanoparticles have a high absorption coefficient in the near ultraviolet and blue of the visible region.

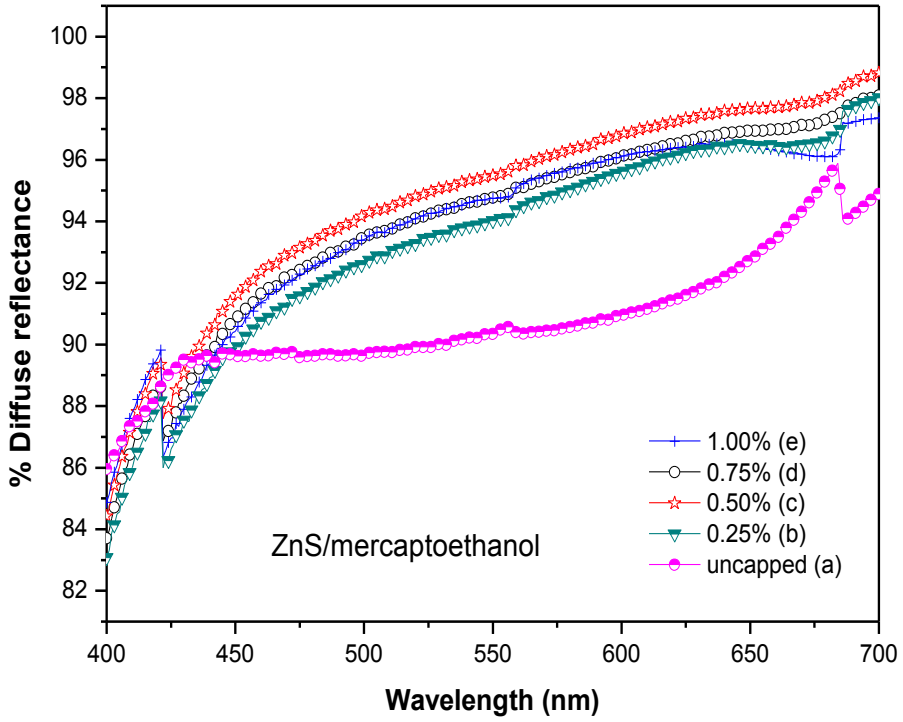

Figure 4.13 Diffuse reflectance spectra of ZnS nanoparticles (a) uncapped, and mercaptoethanol capped (b) 0.25% (c) 0.50% (d) 0.75% (e) 1.00 %

Fig. 4.13 shows the diffuse reflectance spectra of uncapped and mercaptoethanol capped ZnS. As explained in case of thiophenol, similar variation in the diffuse reflectance has been observed. On increasing the mercaptoethanol concentration from 0

to 0.50 %, the diffuse reflectance increases, whereas, it decreases on further increase in concentration from 0.50 to 1.00%. ZnS nanoparticles capped with 0.50% of mercaptoethanol shows the attainment of maximum diffuse reflectance (84.64 – 98.69%), however, this is less than the ZnS nanoparticles capped with 0.50% of thiophenol which shows diffuse reflectance in the range 91.50 – 100%. As explained, the kinks centered at 426 and 685 nm were also observed in this case.

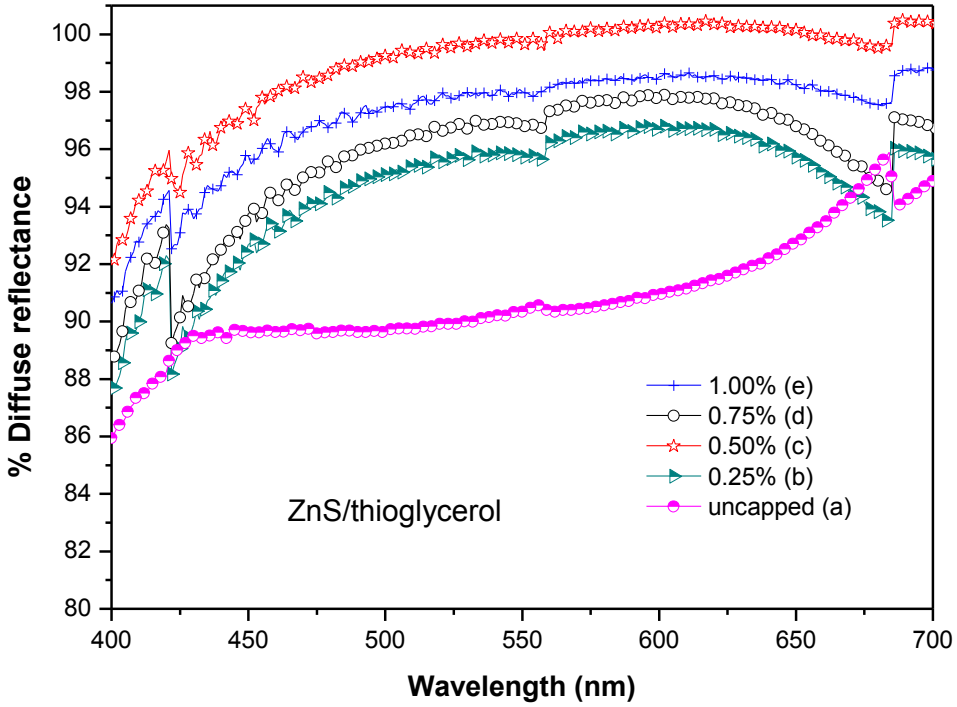

Figure 4.14 Diffuse reflectance spectra of ZnS nanoparticles (a) uncapped, and thioglycerol capped (b) 0.25% (c) 0.50% (d) 0.75% (e) 1.00 %

Fig. 4.14 shows the diffuse reflectance spectra of uncapped and thioglycerol capped ZnS. On increasing the thioglycerol concentration from 0 to 0.50 %, the diffuse reflectance increases, whereas, it decreases on further increase in concentration from 0.50 to 1.00%. ZnS nanoparticles capped with 0.50% of thioglycerol shows the attainment of maximum diffuse reflectance (92.16 - 100%). Kinks centered at 426 and 685 nm were also observed in this case.

The uncapped ZnS nanoparticles form a powder layer acting as a thin film. The light incident on it undergoes destructive interference and that is why the reflected light intensity has been found to be low in this case [153]. On capping ZnS nanoparticles (refractive index (n) = 2.37) with capping agent like thioglycerol (n = 1.6) mercaptoethanol (n = 1.4) and thiophenol (n = 1.6), the coating behaves like a homogeneous and isotropic film because of uniform shape and size of the particles (Fig. 4.6a and b). Consequently, this results in specular reflections and the reflected light interferes constructively, which explains the increase in the intensity of the reflected light with capping concentration (0 to 0.50%). With further increase in the capping concentration from 0.50 to 1.00%, the shape and size of the particles no longer remain uniform because of agglomeration (Fig. 4.7a and b). Therefore, the capping (surface passivation) results in uneven surface, thereby decreasing reflectance.

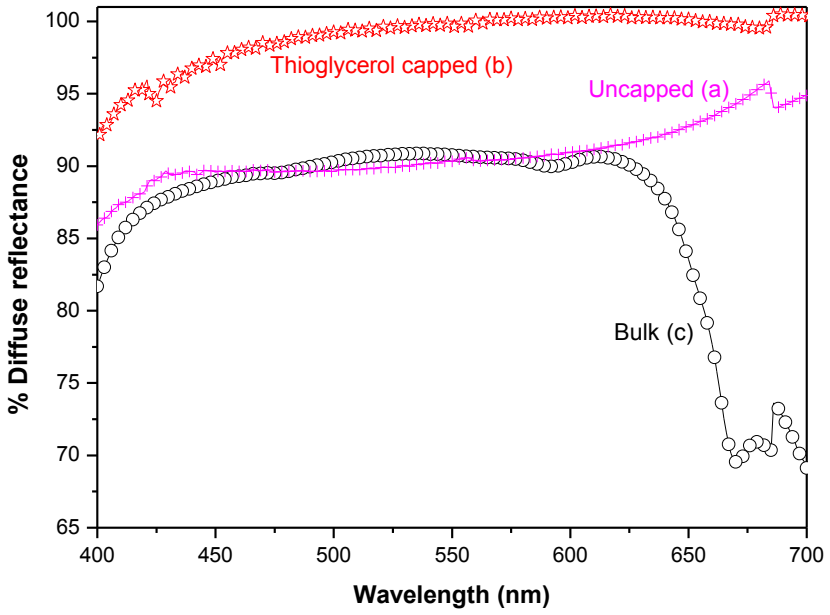

Figure 4.15 Diffuse reflectance spectra of ZnS (a) uncapped nanoparticles, (b) 0.50% thioglycerol capped nanoparticles (c) bulk particles

Fig. 4.15 shows the diffuse reflectance spectra of uncapped and thioglycerol capped ZnS nanoparticles as well as commercially available bulk ZnS particles. As observed from the spectra, the reflectance of bulk ZnS particles decreases sharply after 625 nm (Fig. 4.15) and it has been well reported in the literature [39]. In industry, bulk ZnS is prepared by reacting its respective mineral ores and the particles, so obtained, are non-uniform in shape and size, and not stable in visible light; gets decolorized. To achieve stability against decolorization bulk ZnS is doped with cobalt; due to which absorption is produced in the visible region (625 - 700 nm). Therefore bulk ZnS cannot be employed as reflective pigment in the industry. Fig. 4.15 also reveals that reflectance of bulk ZnS is less than the uncapped as well capped nanoparticles.

From the present diffuse reflectance study it has been concluded that capping effects the reflective propertied of ZnS nanoparticles. On comparing the diffuse reflectance of thiophenol, mercaptoethanol and thioglycerol capped ZnS nanoparticles; it has been observed that 0.50% thioglycerol capped ZnS nanoparticles shows the maximum diffuse reflectance (92.16 - 100%). Owing to the uniform and high reflectance throughout the visible region of capped ZnS nanoparticles as compared to the bulk ZnS particles, these nanoparticles are potential candidates for the preparation of reflective coatings.

4.7 Diffuse reflectance analysis of reflectors developed using ZnS nanoparticle-based coatings

ZnS nanoparticles capped with 0.50% thioglycerol show maximum diffuse reflectance and therefore, have been employed as reflective pigment for the preparation of coating materials. This coating material has been applied to aluminium/plastic substrates to develop reflectors.

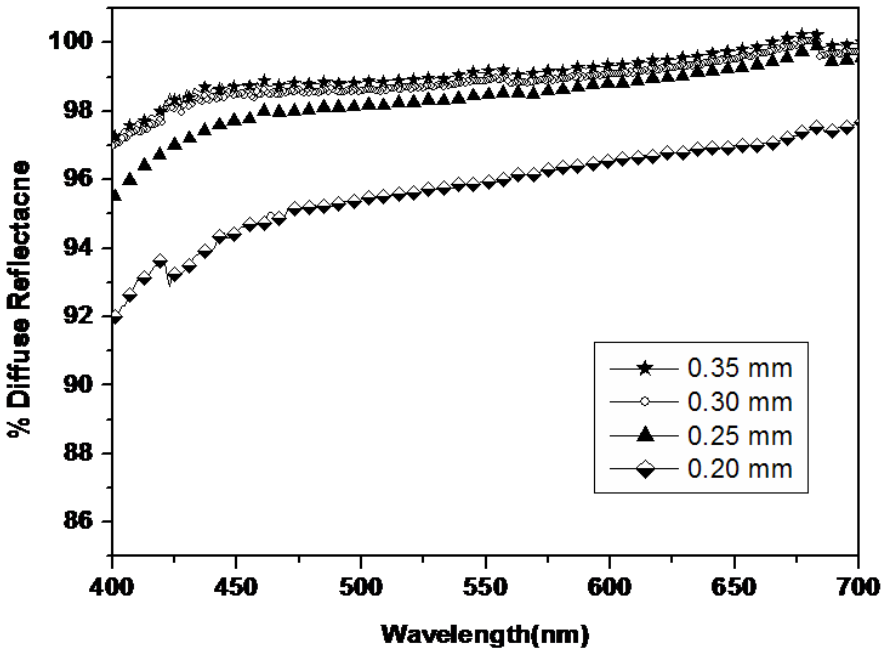

Figure 4.16 Diffuse reflectance spectra of the developed reflectors (aluminium as substrate) having different coating thicknesses

Fig. 4.16 shows the diffuse reflectance of reflectors coated with 0.20, 0.25, 0.30 and 0.35 mm, thicknesses. As seen from Fig. 4.16, the reflectance increases with the increase in the coating thickness. For 0.20, 0.25 and 0.30 mm of coating thicknesses, the diffuse reflectance varies respectively from the 92 - 98 %, 95 - 99% and 97% - 100%. With further increase in thickness, i.e., from 0.30 mm to 0.35 mm, there is not much increase in the reflectance.

Thickness of the coating has been found to influence its reflectance, hiding capability and overall cost. With increasing thickness, the reflectance increases because greater the film thickness, greater is the number of pigment particles on the substrate, which contributes to higher reflectance. Hiding power is an optical property used to describe the light scattering efficiency of a coating and measures its ability to obscure the background of the contrasting color. ZnS/thioglycerol nanoparticles offer good hiding capability to the substrate as compared to the other coating materials applied up to the

same thickness [154] and hence reduce the cost of coating significantly. The small kink at 425 nm in the curve is the luminescence peak related to sulfur (S^{2-}) anion vacancy, but this brings only about 0.5% change in the reflectance.

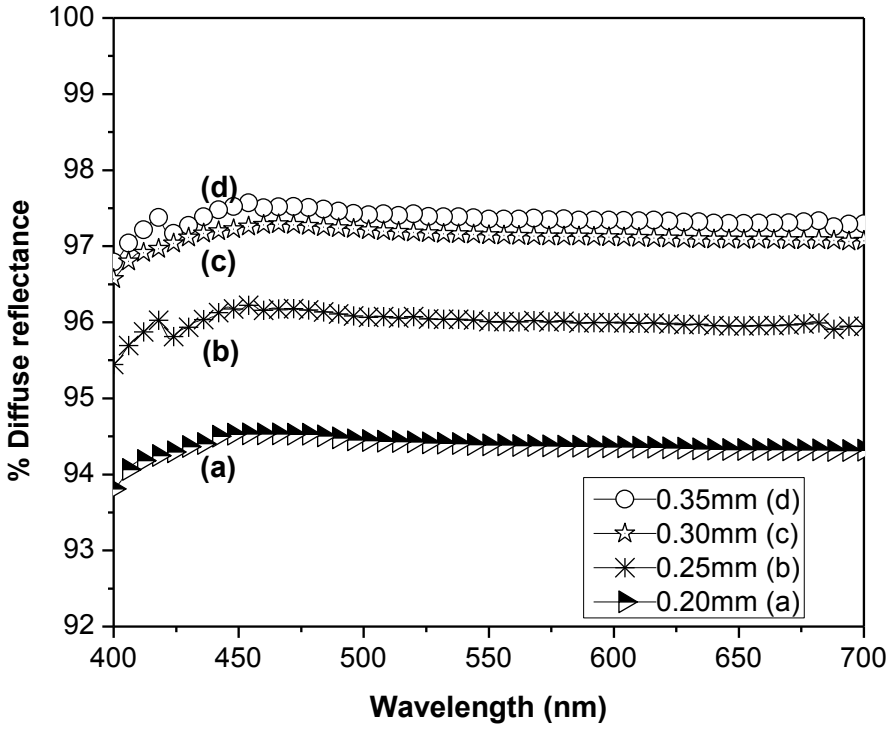

Fig. 4.17 Diffuse reflectance spectra of the developed reflectors (plastic as substrate) having different coating thicknesses

Fig. 4.17 shows the diffuse reflectance spectra of reflectors (plastic as substrate) having different coating thicknesses. It reveals that with increase in coating thickness, the reflectance increases. For coating thickness, 0.20, 0.25, and 0.30 mm, the diffuse reflectance has been found to be, respectively, 93.5 - 94.5%, 95.5 - 96.5%, and 96.5 - 97.5%. With further increase in coating thickness from 0.30 to 0.35 mm, the change in reflectance is not appreciable. The coating thickness, 0.30 mm, is the optimum coating thickness. At the optimum coating thickness, above the critical volume pigment

concentration, no substantial difference in the behaviour and appearance of the coating is observed, which plays an important role in determining reflectance.

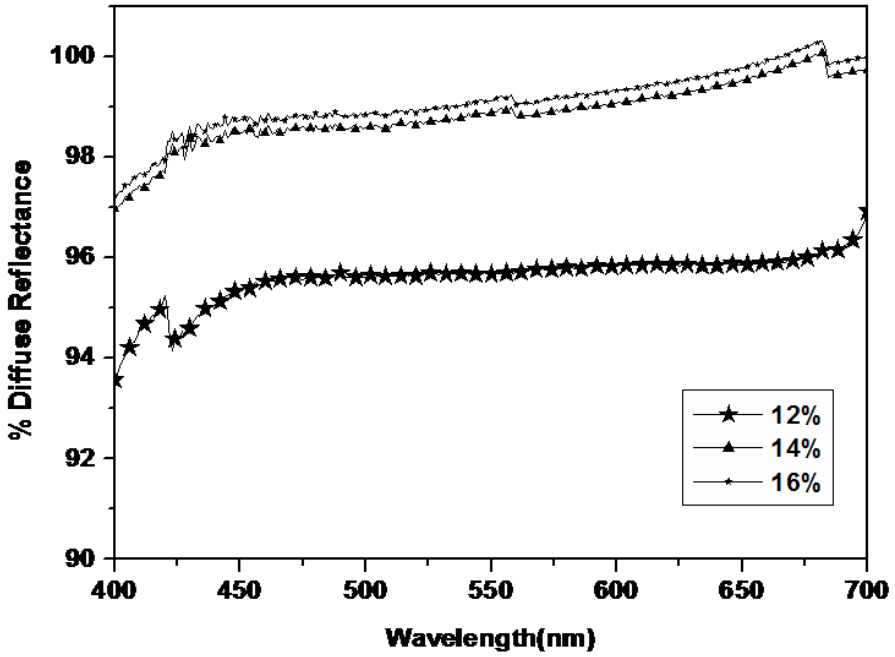

Figure 4.18 Diffuse reflectance spectra of the developed reflectors (aluminium as substrate) having different binder ratio

The concentration of the binder, VISYCRYL- 8350, containing acrylic polymer has been varied to study its effect on the reflectance spectra of the coating. Fig. 4.18 shows the reflectance spectra of the developed reflector (aluminium as substrate) coated with different concentrations of binder. The binder amount is adjusted in such a way so as not to affect the thermal and mechanical properties of the reflective coating. Coating formation occurs when the coating material is applied and the solvent evaporates; during this process, pigment and binder come together. As the solvent evaporates, capillary action draws the binder particles together, causing them to fuse and bind the pigment and binder into a continuous coating. As seen from Fig. 4.18, with the increase in the binder concentration, there is an increase in the diffuse reflectance of the coating. For binder concentration from 12% to 14%, the diffuse reflectance increases respectively from 93 -

96% to 97 - 100%. With further increase in the binder concentration, i.e., from 14% to 16%, there is not much increase in the reflectance.

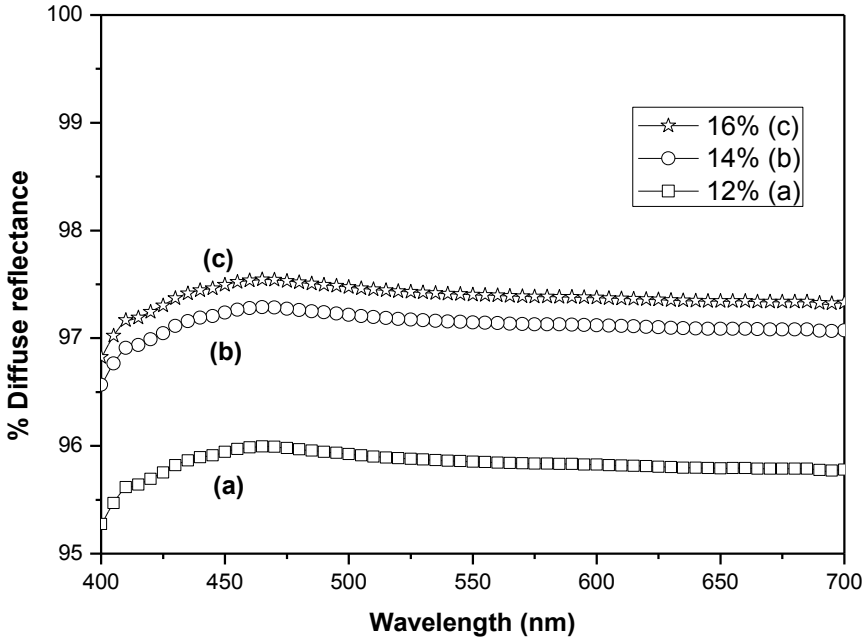

Figure 4.19 Diffuse reflectance spectra of the developed reflectors (plastic as substrate) having different binder ratio

Fig. 4.19 shows the reflectance spectra of the developed reflectors (plastic as substrate) coated with different concentrations of binder. As seen from Fig. 4.19, with the increase in the binder concentration, there is an increase in the diffuse reflectance of the coating. For binder concentration from 12% to 14%, the diffuse reflectance increases respectively from 95.29 - 95.78% to 96.63 - 97.06%. With further increase in the binder concentration, i.e., from 14% to 16%, there is not much increase in the reflectance. With higher binder concentration, there is a strong capillary action between the binder particles, causing them to fuse together and bind the ZnS/thioglycerol nanoparticles into a continuous film.

There are two more factors which contribute to diffuse reflectance; one is micro surface roughness and the other, optical roughness. In case of micro surface roughness, a coating has tilted surface facets, whereas the optical roughness is because of the way the particles are distributed; if there is a wide particle distribution, it is called high optical roughness, and in case of narrow particle distribution, it is called low optical roughness. The micro surface roughness causes light to go in different directions and causes anisotropy. In case of high optical roughness and low optical roughness, respectively, diffuse and specular reflectance is produced. For high reflective coatings, the micro surface roughness as well as optical roughness is always adjusted to be as small as possible. In the present work, small micro surface roughness is achieved by applying consecutive thin layers of the coatings and small optical roughness is achieved by using higher pigment to binder ratio.

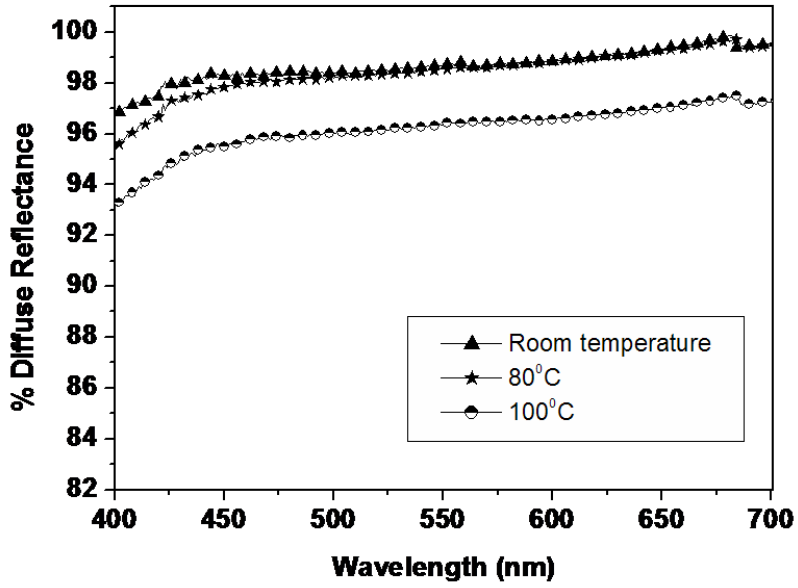

Figure 4.20 Diffuse reflectance spectra of the developed reflectors (aluminium as substrate) exposed to different temperature

Fig. 4.20 and 4.21 show the diffuse reflectance of reflectors (aluminium as substrate) which have been heated respectively at 80^{o}C and 100^{o}C and exposed respectively to 10,000 lux and 15,000 lux for 50 hour to check the durability of the

coating. Durability is a term applied to the various changes in appearance and functional values of the reflective coatings; it also includes all aspects of exterior serviceability, such as: retention of reflectance, gloss, color, adhesion and film integrating. The initial effect is usually caused by degradation of the binder on exposure to temperature and illumination. On heating the reflector for 50 hour at 100^{o}C and 80^{o}C, the diffuse reflectance has been found to decrease respectively by 5% and 1%, which is due to the binder degradation. Depending upon the binder and particular application, this temperature range can be optimized.

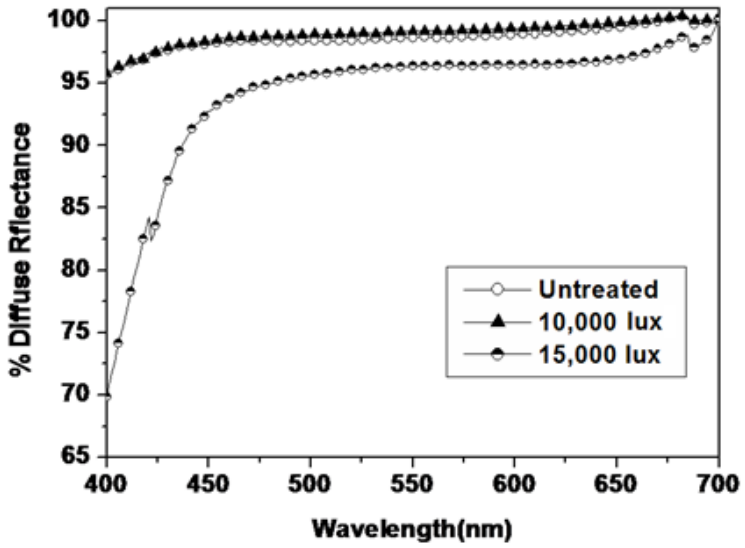

Figure 4.21 Diffuse reflectance spectra of the developed reflectors (aluminium as substrate) exposed to light of different lux

Less than 1% change in diffuse reflectance has been observed on illuminating the reflectors by visible light of intensity 10,000 lux for 50 hour (Fig. 4.21). However, on using 15,000 lux illumination, a drastic decrease from 95% to 70% in the reflectance has been observed at about 400 nm region, whereas reflectance for the other wavelengths has been altered by about 5%. This drastic decrease is due to the generation of surface defects in ZnS/thioglycerol pigments caused by strong illumination; also the blue region at 400

nm, being closer to the high energy ultra-violet region, degrades the pigments [155, 156]. However, the coating has been found to be stable up to 10,000 lux illumination.

Flexibility and thermal stability of the coating has been checked to ensure the durability of the reflector (Plastic as substrate). Coating must be flexible enough so as not to develop crack or split with shrinkage of substrate due change in temperature. A simple method to check the flexibility of the coating has been applied by changing the working temperature from 30 to 45^{o}C, which showed, respectively, 5.0% and 10.5% decrease in the substrate surface area without any crack or split being developed in the coating. And on heating at 50^{o}C, the coating developed crack. Thus, the developed reflectors have been found to be flexible and thermally stable up to 45^{o}C.

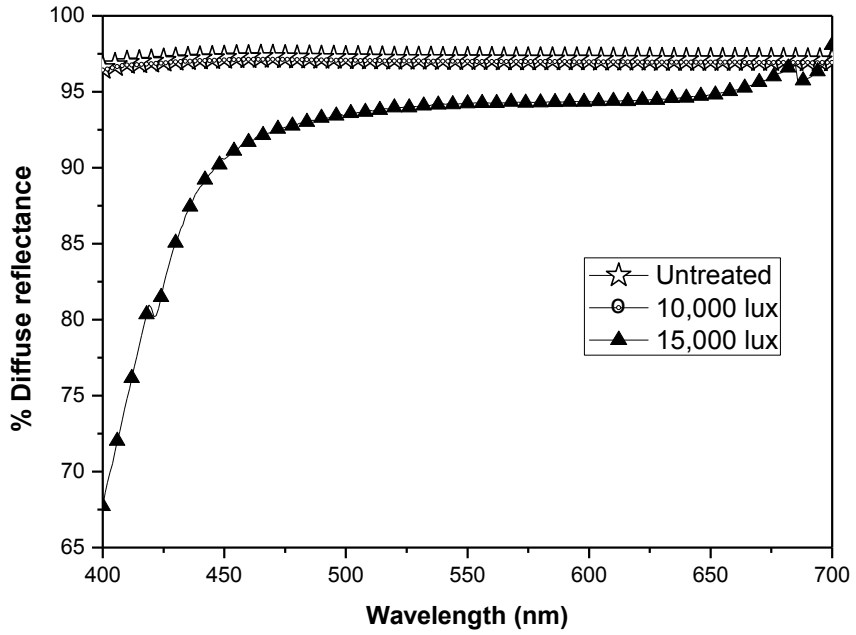

Figure 4.22 Diffuse reflectance spectra of the developed reflectors (plastic as substrate) exposed to light of different lux

Fig. 4.22 illustrates the diffuse reflectance of reflectors (plastic as substrate), exposed respectively to 10,000 lux and 15,000 lux for 50 hour to test the durability of the

coating. As shown in the Fig. 4.22, less than 0.5% change in diffuse reflectance has been observed on illuminating the reflectors by visible light of intensity 10,000 lux. However, on increasing the illumination to 15,000 lux, a drastic decrease from 94.43% to 67.50% in the reflectance has been recorded at about 400 nm region, whereas reflectance for the other wavelengths has been altered by about 5%. Hence, reflectors are found to stable up to 10,000 lux.

Table 4.5 shows the comparison of different properties of reflectors developed with aluminium and plastic substrate using ZnS nanoparticle-based coatings. With aluminium substrate, the reflectors show more than 97% diffuse reflectance. Further, it has been observed that on changing the substrate from aluminium to plastic, the diffuse reflectance and optical stability do not show any appreciable change. However, the reflectors with aluminium substrate have been found to be thermally stable up to 80^{o}C and those with plastic substrate, only up to 45^{o}C.

Table 4.5 Comparison of different properties of reflectors developed with aluminium and plastic substrate using ZnS nanoparticle-based coating

Property	Aluminium substrate	Plastic substrate
Optimum coating thickness (mm)	0.30	0.30
Optimum pigment to binder ratio	14	14
Maximum diffuse reflectance	97% - 100%	96.5 - 97.5%
Thermal stability (^{o}C)	80	45
Optical stability (lux)	10,000	10,000

As observed form the Table 4.5, for the ZnS nanoparticle-based coating material, optimum coating thickness, optimum pigment to binder ratio and optical stability is found to be same for both the substrates, however thermal stability is found to different.

4.8 Phase detection and structural analysis of TiO_2

XRD is essential for the determination of the crystal structure, crystallinity and crystal grain size. Fig. 4.23 is the X-ray diffraction (XRD) pattern of the uncalcined titania powder, indicating its amorphous nature. The amorphous phase could be hydrous TiO_2, i.e., $TiO_2.nH_2O$.

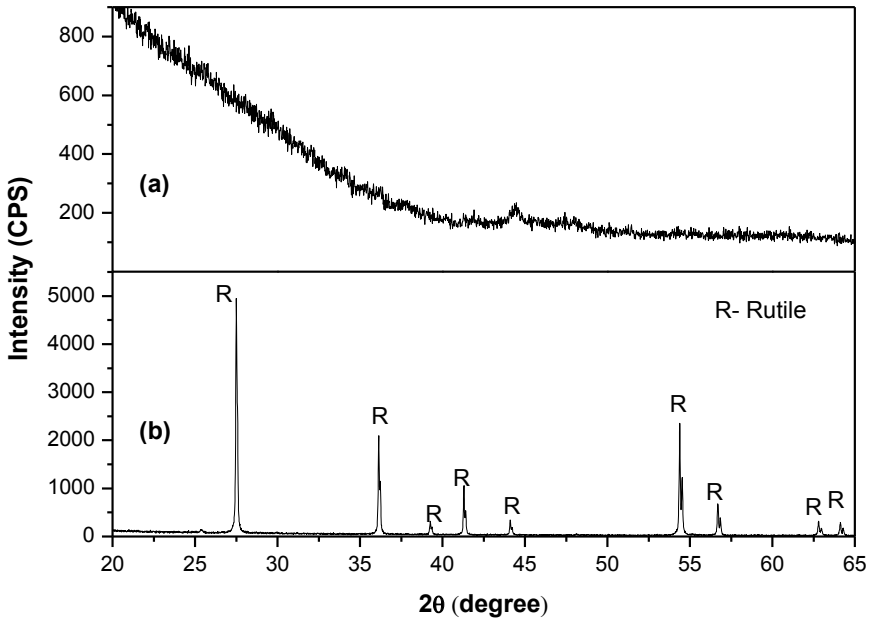

Figure 4.23 XRD pattern of TiO_2 powder (a) uncalcined (b) calcined at 900°C

The XRD pattern of TiO_2 powder calcined at 900°C is shown in Fig. 4.22(b). The peaks indexed to the reflection from (110), (101), (200), (111), (210), (211), (220), (002),

and (310) planes, at 2θ values 27.54°, 36.04°, 39.20°, 41.12°, 44.14°, 54.33°, 56.89°, 62.82°, and 64.17° correspond to rutile phase of TiO_2 (JCPDS card #860148). The crystallite size of the calcined TiO_2, calculated using Debye Scherrer's equation (2.2) comes out to be 77.50 nm. The full width at half maximum (FWHM) has been calculated from the most intense peak (Fig. 4.23(b)), using Lorentz function ($R^2 > 0.98$). Lorentzian function excellently fitted the experimentally line profile of the sample.

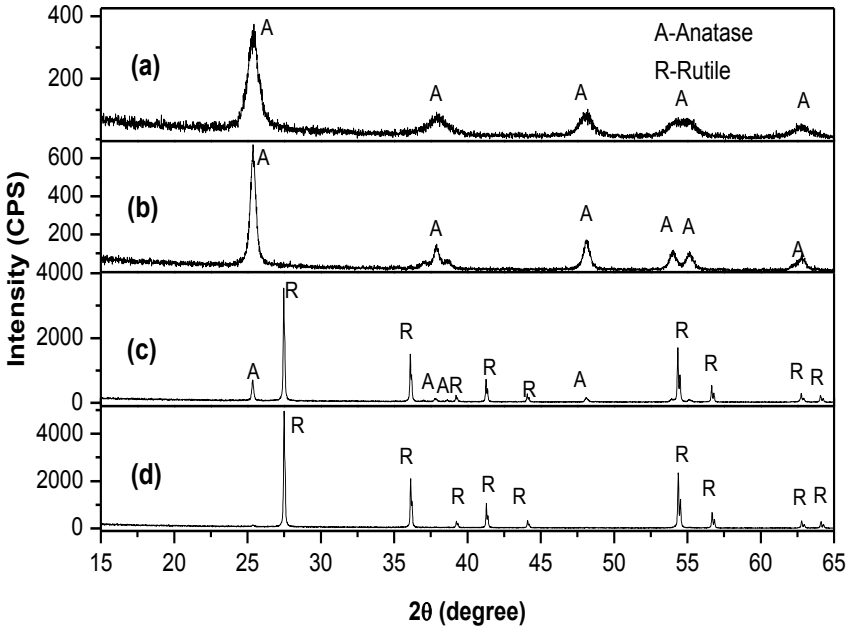

Figure 4.24 X-ray diffraction patterns of TiO_2 nanoparticles calcined at (a) 350°C (b) 550°C (c) 750°C (d) 900°C

The XRD patterns of TiO_2 powder calcined at different temperatures are shown in Fig. 4.24 The peaks indexed to the reflection from (110), (101), (200), (111), (210),

(211), (220), (002), and (310) planes, at 2θ values 27.54°, 36.04°, 39.20°, 41.12°, 44.14°, 54.33°, 56.89°, 62.82°, and 64.17° correspond to rutile phase of TiO_2 (JCPDS card #860148) as well as, the reflection from (101), (004), (200), (105), (211) and (204) planes, at 2θ values 25.44°, 38.02°, 48.19°, 53.94°, 54.98°, and 63.06° correspond to anatase phase of TiO_2 (JCPDS card #861157). Fig. 4.24(a) and (b) reveals that samples calcined at 350°C and 550°C exhibit characteristic peaks of only anatase phase, while the sample calcined at 750°C exhibit peaks of both anatase and rutile phase. Examination of the kinetics of the anatase to rutile phase transformation involves the assessment of the relative quantities of anatase and rutile weight fraction at 750°C. The weight fraction (W_R) of rutile phase content calcined at 750°C (Fig. 4.24(c)) was calculated from the equation (2.7)

$$W_R = \frac{1}{(1 + I_A / 0.886 I_R)}$$

where I_A and I_R are the intensity of most intense peaks of anatase and rutile phase respectively. Substituting the values of I_A and I_R from Fig. 4.24(c), W_R for rutile phase is 83%. Mixed-phases (rutile–anatase) of TiO_2 have been reported to exhibit enhanced photoactivity relative to single-phase titania [157]. It is considered widely that this is the result of improved charge carrier separation, possibly through the trapping of electrons in rutile and the consequent reduction in electron–hole recombination [158]**.**

With the further increase in the calcination temperature, i.e., 750°C to 900°C the formation of complete rutile phase has been observed. From the XRD patterns (Fig. 4.24 (c, d)), it is clear that with increase in calcination temperature, the peak broadening decreases and phase transformation from anatase to rutile registers incline. The anatase to rutile transformation is reconstructive, which means that the transformation involves the breaking and reforming of bonds [159]. This is in contrast to the displacive

transformation, in which the original bonds are distorted but retained. The reconstructive anatase to rutile transformation involves a contraction of the c-axis and an overall volume contraction of 8% [160]. This volume contraction explains the higher density of rutile relative to anatase. For the transformation of anatase to rutile phase a sufficient amount of thermal energy is required to facilitate the rearrangement of atoms. It has been reported that for typical bulk TiO_2 powders this energy requirement is obtained at 600-700°C in air in the absence of any dopants or impurities. However, the reported transition temperature varies in the range 400-1200°C, owing to the use of different methods of determining the transition temperatures, raw materials and processing techniques. The anatase to rutile transformation is not instantaneous; it is time-dependent because it is reconstructive. This transformation temperature can be enhanced or impeded by influencing the rearrangement of the atoms in the anatase and rutile lattices. It has been reported that the most important factor affecting the phase transformation is the presence and amount of oxygen defects in the titania lattice [161]. Ease of rearrangement and transformation are enhanced by relaxation of the large oxygen sublattice through the increased presence of oxygen vacancies [162].

Table 4.6 shows the crystallite sizes of the samples calcined at different temperatures, calculated using Debye Scherrer's equation (2.2). Crystallite size is determined by measuring the broadening of a particular peak in the diffraction pattern associated with a particular planar reflection from within the crystal unit cell. It is inversely related to the full width at half maximum (FWHM) of an individual peak; narrower the peak, larger the crystallite size. The periodicity of the individual crystallite domain reinforces the diffraction of the X-ray beam, resulting in a tall narrow peak. If the crystals are randomly arranged or have low degrees of periodicity, the result is a broader peak [50]. This is normally the case for nanomaterial assemblies. Thus, it is apparent that the FWHM of the diffraction peak is related to the size of the nanomaterials. The FWHM has been calculated from the most intense peak (Fig. 4.23), using Lorentz best fit curve

(R^2 > 0.98). It is clear from Table 4.6 that with increase in the calcination temperature, the crystallite size increases.

Table 4.6 Nanoparticle-crystallite size variation with calcination temperatures

Sr. No.	Sample & Calcination temperature (°C)	Crystallite size (nm)
(a)	TiO_2: 350	29.31
(b)	TiO_2: 550	49.16
(c)	TiO_2: 750	73.25
(d)	TiO_2: 900	77.50

Fig. 4.25 shows the X-ray diffraction pattern of TiO_2 nanoparticles calcined at 900^oC with different L values. All the peak are well matched with rutile phase of TiO_2 (JCPDS card #860148).

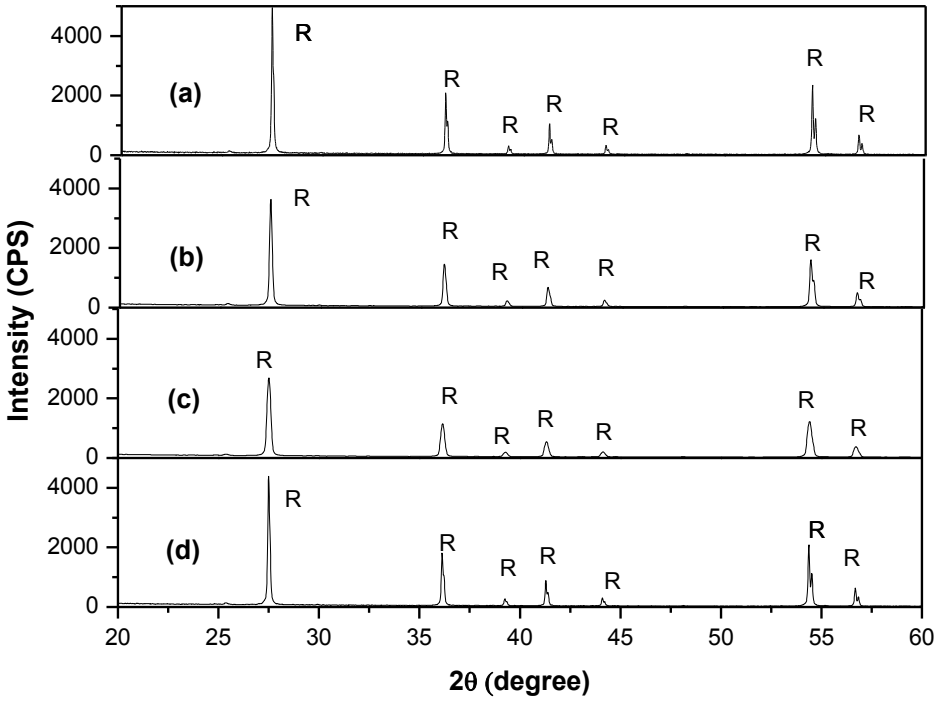

Figure 4.25 X-ray diffraction patterns of TiO_2 nanoparticles calcined at 900^oC with different L values (a) 20 (b) 30 (c) 40 (d) 50

As observed from the XRD pattern, with increase in the L value i.e., from 20 to 40, there is an increase in the peak broadening but with further increase in the L value from 40 to 50, depreciation takes place. Table 4.7 shows the crystallite sizes of the samples calcined at 900^oC, with different L values calculated using Debye Scherrer's equation (2.2). Fig 4.26 shows the graphical variation of crystallite size with L values for TiO_2 nanoparticles calcined at 900^oC. As observed from the Fig. 4.26, with increase in the L values from 20 to 40, there is decrease in the crystallite size and with further increase in the L values from 40 to 50, the crystallite size increases.

Table 4.7 Nanoparticle-crystallite size variation with L values

Sr. No.	L values	Crystallite size (nm)
(a)	20	77.50
(b)	30	74.20
(c)	40	70.34
(d)	50	78.31

For the formation of TiO_2 nanoparticles the net reaction as explained in chapter 3 is shown below

Hydrolysis:

$$Ti - OR + H_2O \rightarrow Ti - OH + R - OH$$

Alcohol and water condensation:

$$(Ti - OH)n + (RO - Ti)n \rightarrow n(Ti - O - Ti) + n(R - OH) + n\,H_2O$$

As clear from the above reactions, the nucleation rate of TiO_2 particles increases with increasing L, and as a result, the average nanocrystallite size and the average nanoparticle size should decrease with increasing L (Table 4.6). In addition to this, with increasing L, although the, hydrolysis reaction in the above equation is driven in the forward direction, the condensation reaction driven in the reverse direction, which suggests more dissolution of TiO_2 particles, which effectively reduce the average size of nucleated TiO_2 particles. However, due to the formation of large number of nuclei with increasing L, the growth rate of the TiO_2 nanocrystallites also increases [67].

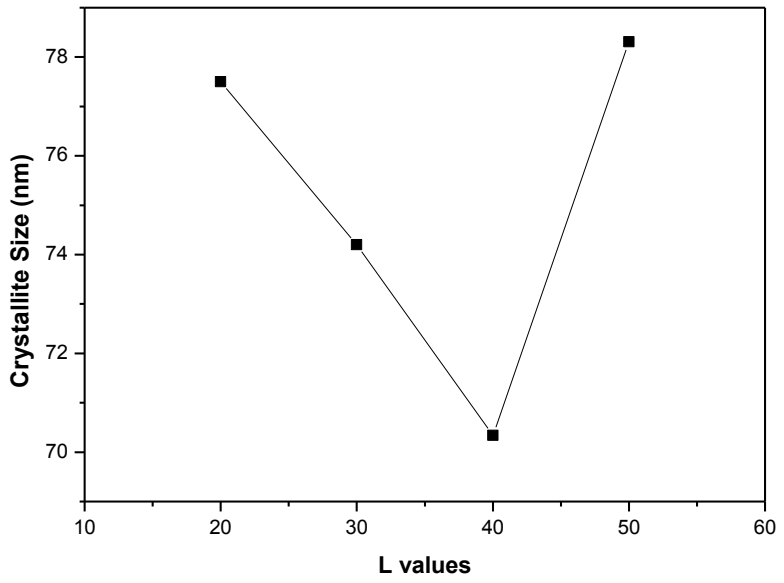

Figure 4.26 Nanoparticles crystallite size variation with L values

4.9 Microstructural analysis of TiO_2

The size and morphology of TiO_2 nanoparticles was investigated by TEM. The values of H_2O/titanium (L) precursor and calcination temperatures are significant parameters in controlling TiO_2 particle size and size distribution. In the present study, both the parameters were utilized to control the morphology of TiO_2 nanoparticles. Fig. 4.26 shows the TEM micrographs of uncalcined TiO_2. It reveals that the uncalcined particles get aggregated and coalesce non-uniformly because of cohesive force of TiO_2 nanoparticles.

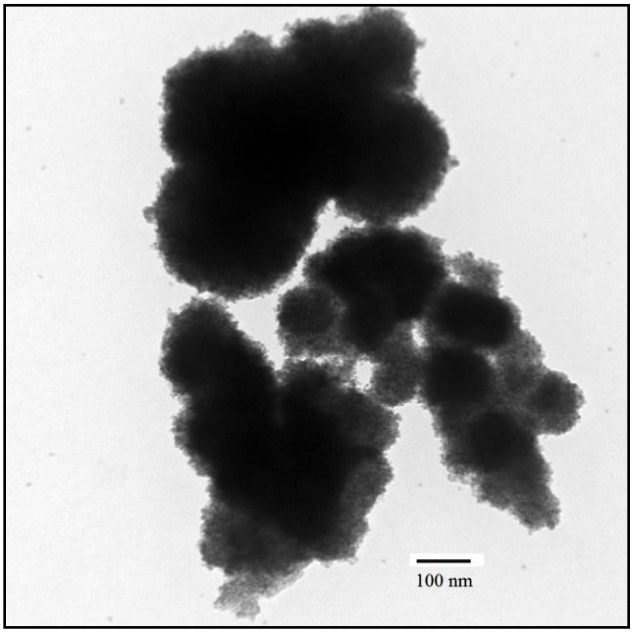

Figure 4.27 TEM micrograph of uncalcined TiO_2 nanoparticles

Amorphous TiO_2 nanoparticles have been transformed into anatase when heated at temperature from 350°C to 550°C (XRD study). Fig. 4.28 shows the TEM micrographs of TiO_2 nanoparticles calcined at 350°C and 550°C. According to the micrographs, the particles are found to be uniformly distributed and nearly spherical. This might be due to the decrease in the cohesive force of TiO_2 nanoparticles with the increase of the average diameter of TiO_2 nanoparticles [163]. With the increase in the calcination temperature from 350°C to 550°C, the particle size increases (Table 4.8)

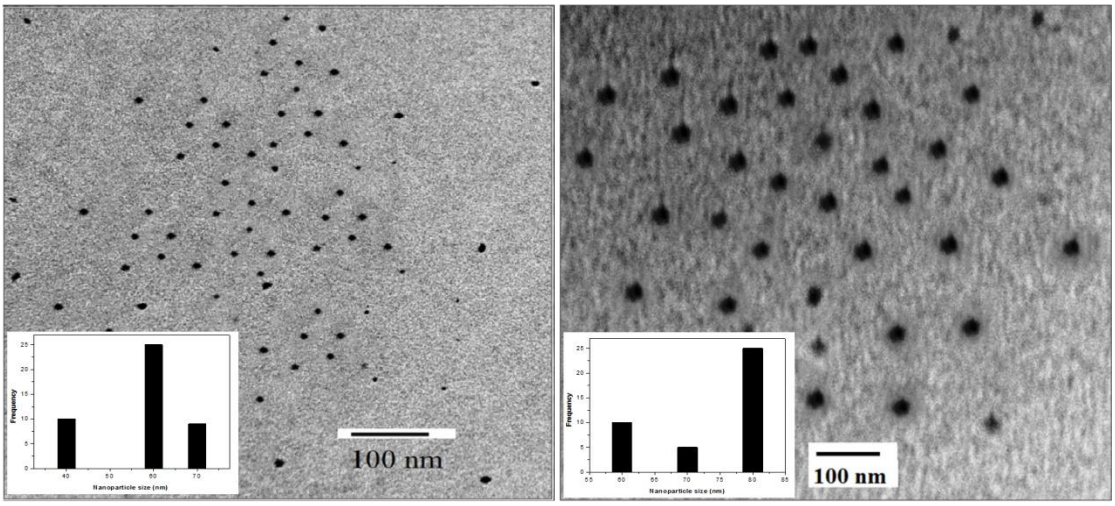

Figure 4.28 TEM micrographs of TiO_2 nanoparticles calcined at (a) 350°C (b) 550°C

Fig. 4.29 shows the TEM micrographs of TiO_2 nanoparticles calcined at 750°C and 900°C. The particles are found to be uniformly distributed and nearly spherical. With increase in the calcination temperature from 750°C to 900°C, the particle size increases (Table 4.8).

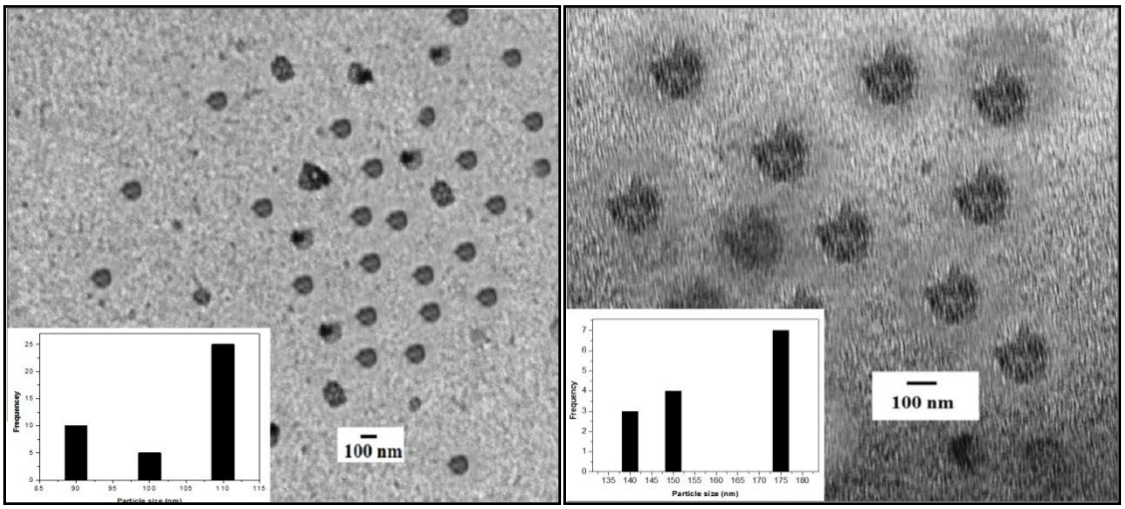

Figure 4.29 TEM micrographs of TiO_2 nanoparticles calcined at (a) 750°C (b) 900°C

The average size (Table 4.8) of calcined particles has been calculated from TEM micrographs by plotting histograms. Significant rutile grain growth is exhibited as the

anatase to rutile transition proceeds. Rutile grains coarsen at the expense of neighboring anatase during coalescence until the large rutile grains begin to impinge on each other [164]. This increase in grain size causes a decrease in surface area leading to decrease in photocatalytic activity and increase in the photostability of TiO_2 nanoparticles. It can be observed (Table 4.8) that the heat treatment of the nanopowders largely affects the domain size, as calculated through TEM micrographs, it increased from 60 nm for the as-synthesized nanopowders up to 175 nm for the TiO_2 treated at 900°C.

Table 4.8 Particle size variation with calcination temperature

Sr. No.	Sample & Calcination temperature (°C)	Particle size (nm)
(a)	TiO_2: 350	60
(b)	TiO_2: 550	80
(c)	TiO_2: 750	110
(d)	TiO_2: 900	175

4.10 Absorbance analysis of TiO_2

Fig. 4.30 shows the absorption spectra of the TiO_2 nanoparticles calcined at different temperatures. The spectra reveal that with increase in calcination temperature; the absorption edge gets shifted to higher wavelength (red shift).

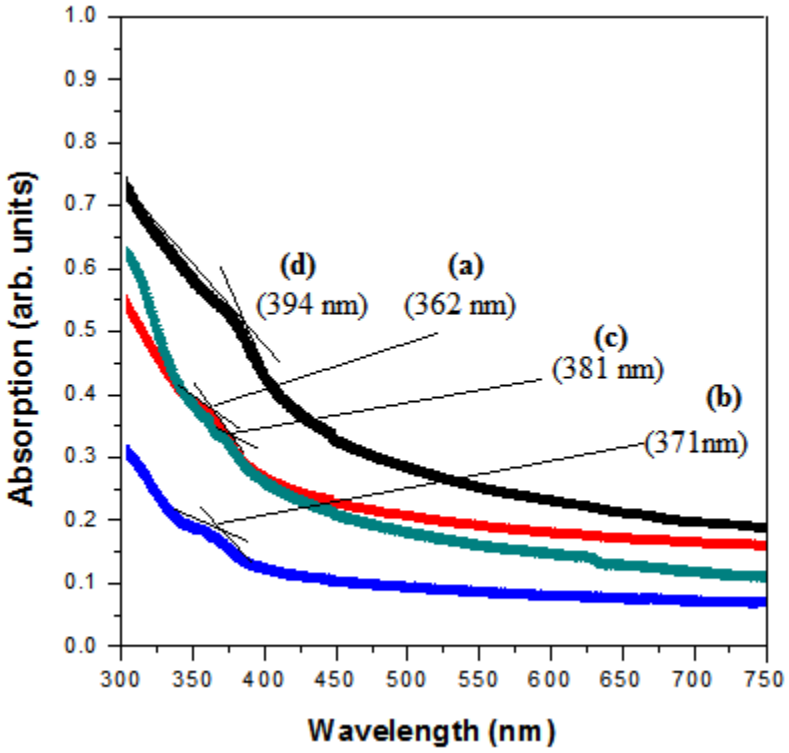

Figure 4.30 UV-Vis absorption spectra of TiO_2 nanoparticles calcined at (a) 350°C (b) 550°C (c) 750°C (d) 900°C

The band gap energies (E_g) of TiO_2 nanoparticles were calculated using the equation (2) [165, 124]

$$E_g = \frac{hc}{\lambda_{int}} \qquad (2)$$

where h is Planck's constant (4.135 x 10^{-15} eV.s); c, the velocity of light (3 x 10^8 m s^{-1}), and λ_{int}, the wavelength (in nm) corresponding to the intersection of extension of linear parts of the spectrum of y-axis and x-axis. From Fig. 4.30, the energy band gap values for TiO_2 nanoparticles calcined at different temperature were found to be in the range of 3.14 - 3.42 eV (Table 4.9). The crystallite size of rutile phase nanocrystalline TiO_2 increases with respect to calcination temperature (XRD study), leading to decrease in the energy band-gap values (Table 4.8). Small band-gap values are indicative of relatively

densely packed crystalline structures. It is well known that the band-gap of a semiconductor decreases with increase in the crystallite size of TiO_2 [76]. Generally, the color of a solid is determined by the position of its absorption edge; a shift of this absorption edge towards a higher wavelength can result in absorption in the visible region.

Table 4.9 Determination of band gap energy of TiO_2 nanoparticles calcined at different temperatures

Sr. No.	Sample & Calcination temperature (°C)	Band gap energy (eV)
(a)	TiO_2: 350	3.42
(b)	TiO_2: 550	3.34
(c)	TiO_2: 750	3.25
(d)	TiO_2: 900	3.14

4.11 Photoluminescence analysis of TiO_2

PL emission spectra have been widely used to investigate the efficiency of charge carrier trapping and migration, and to understand the fate of electron-hole pairs in semiconductors [166] Fig. 4.30 shows the PL spectra of TiO_2 nanoparticles calcined at different temperatures, at an excitation wavelength of 370 nm. As seen from the spectra, a broad peak at 431 nm is observed for all the samples, irrespective of the different calcination temperature. This emission band originated from charge recombination at the shallow-trap surface state [167]**.** These surface states originate from the oxygen vacancies which act as radiative centers.

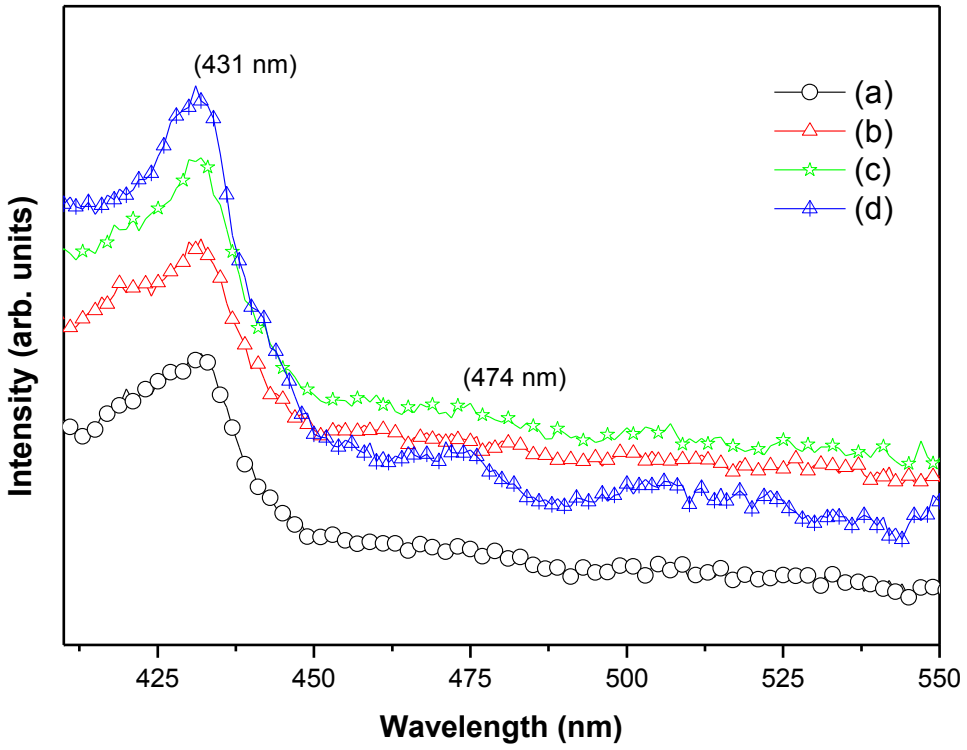

Figure 4.31 Room temperature photoluminescence emission spectra of TiO_2 nanoparticles calcined at (a) 350°C (b) 550°C (c) 750°C (d) 900°C, at an excitation wavelength of 370 nm

The peak around 474 nm for TiO_2 nanoparticles is due to the oxygen vacancy with two trapped electrons, i.e., F centers [169]. These defect states play an important role in determining the reflective properties and photocatalytic properties of TiO_2 nanoparticles. In the manufacturing process of titanium dioxide pigment, it is aimed to obtain a product with the highest photostability and lowest photocatalytic activity [170, 171]. This can be realized in various ways, and the techniques can be divided into two fundamental groups. The first group comprises of the methods that prevent the migration of electrons and holes to the surface of TiO_2, and the second group comprises of the methods that prevent the formation of radicals as a result of reaction due to the electrons and holes located on the particle surface. The photocatalytic properties of TiO_2 can be

diminished by creating defects in its crystalline lattice to introduce traps for the electrons and holes generated under the influence of radiation. Hence, the peaks at 431 and 474 nm act as luminescent centers which help to improve the photostability of TiO_2.

4.12 Diffuse reflectance analysis of TiO_2 nanoparticles

Diffuse reflectance spectroscopy in the visible region is an effective and extensively used technique for the study and characterization of various reflective properties of materials and coatings as well as for determining color of materials and coatings.

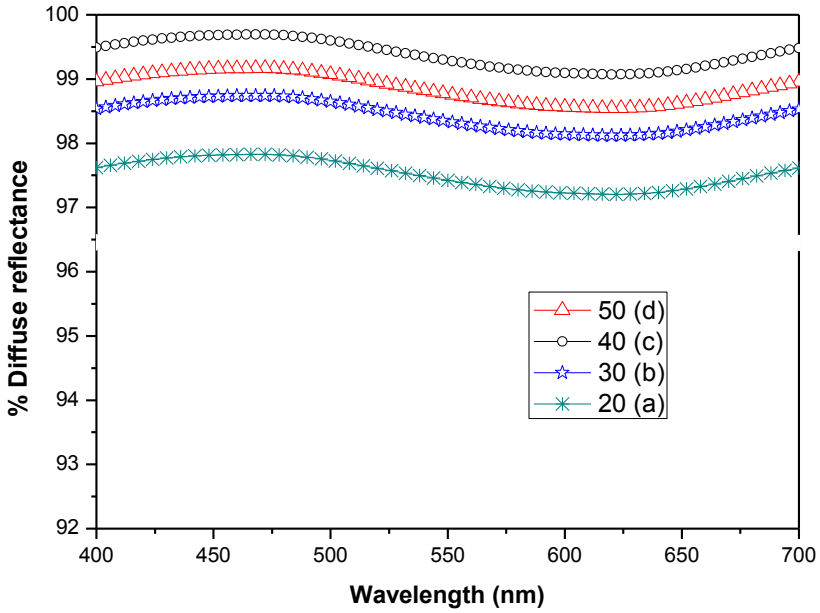

Figure 4.32 Diffuse reflectance spectra of TiO_2 nanoparticles calcined at 900^{o}C with different L values (a) 20 (b) 30 (c) 40 (d) 50

The diffuse reflectance spectra for TiO_2 nanoparticles calcined at 900^{o}C with different L values are shown in Fig. 4.32. On increasing L from 20 to 40, the diffuse reflectance increases, whereas, it decreases on further increasing L from 40 to 50. These results show attainment of maximum diffuse reflectance (99.50 - 99.60%) with L value of

40 for TiO_2 nanoparticles. As observed from XRD study, with increase in L Value (20 - 40), the crystallite size decreases, hence, large is the surface area of particles to scatter light. With further increase in the L value (40 -50), crystallite size increases which leads to decrease in the surface area and reduces the scattering form the particles. Hence, TiO_2 nanoparticles with L value 40, shows the maximum diffuse reflectance (99.50 - 99.60%). These are potential candidates for the preparation of reflective coatings.

4.13 Diffuse reflectance analysis of developed reflectors based on TiO_2 nanoparticle-based coatings

Rutile phase TiO_2 nanoparticles with L value 40 shows maximum diffuse reflectance and therefore have been employed as reflective pigment for the preparation of coating materials. This coating material has been applied to aluminium/plastic substrates to develop reflectors.

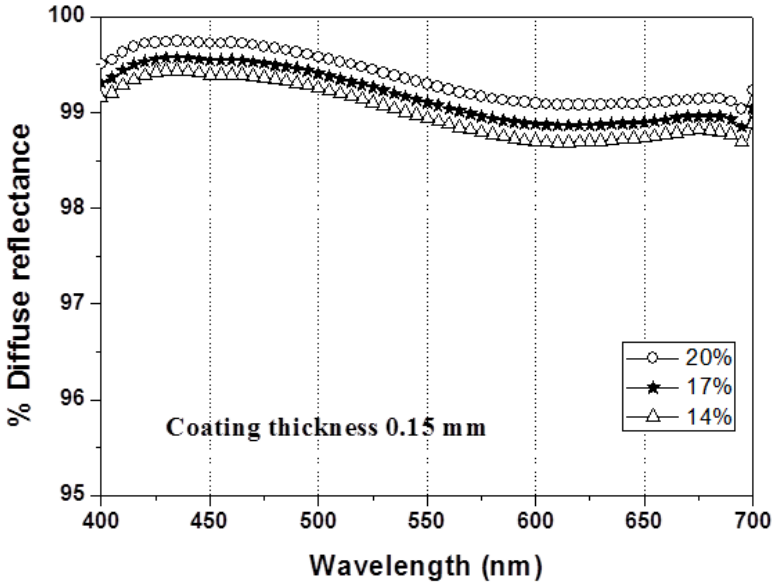

Figure 4.33 Diffuse reflectance spectra of the developed reflectors (aluminium as substrate) having binder weight ratio

Fig. 4.33 shows the diffuse reflectance of developed reflectors (aluminium as substrate) coated with titania nanoparticle-based coating material containing respectively 14, 17 and 20% pigment to binder weight ratio. The diffuse reflectance has been found to be between 99.13 - 98.71% for 14% weight ratio, 99.29 - 98.88% for 17% weight ratio, and 99.52 - 99.01% for 20% weight ratio, which register insignificant overall enhancement in diffuse reflectance of about 0.4%. Further, the diffuse reflectance has been found to be maximum around 450 nm and minimum around 600 nm in the visible spectrum range.

It has been found that coating material, with less than 14% weight ratio is unable to form stable coating layer and gets easily detached from the aluminium sheet. On the other hand, the coating with more than 20% weight ratio, develops cracks; this might be due to the large surface tension of the coating [171].

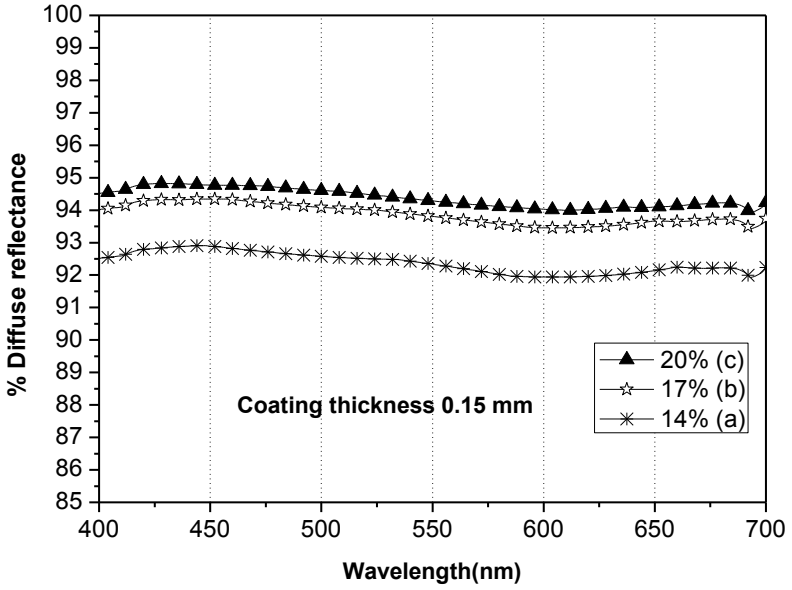

Figure 4.34 Diffuse reflectance spectra of the developed reflectors (plastic as substrate) having binder weight ratio

Fig. 4.34 shows the reflectance spectra of the developed reflectors (plastic as substrate) coated with different concentrations of binder. As seen from 4.34, with the increase in the binder concentration, there is an increase in the diffuse reflectance of the coating. For binder concentration from 14 to 17%, the diffuse reflectance increases respectively from 92.56 - 92.40% to 94.05 - 93.88%. With further increase in the binder concentration, i.e., from 17% to 20%, there is not much increase in the reflectance. With higher binder concentration, there is a strong capillary action between the binder particles, causing them to fuse together and bind TiO_2 nanoparticles into a continuous film.

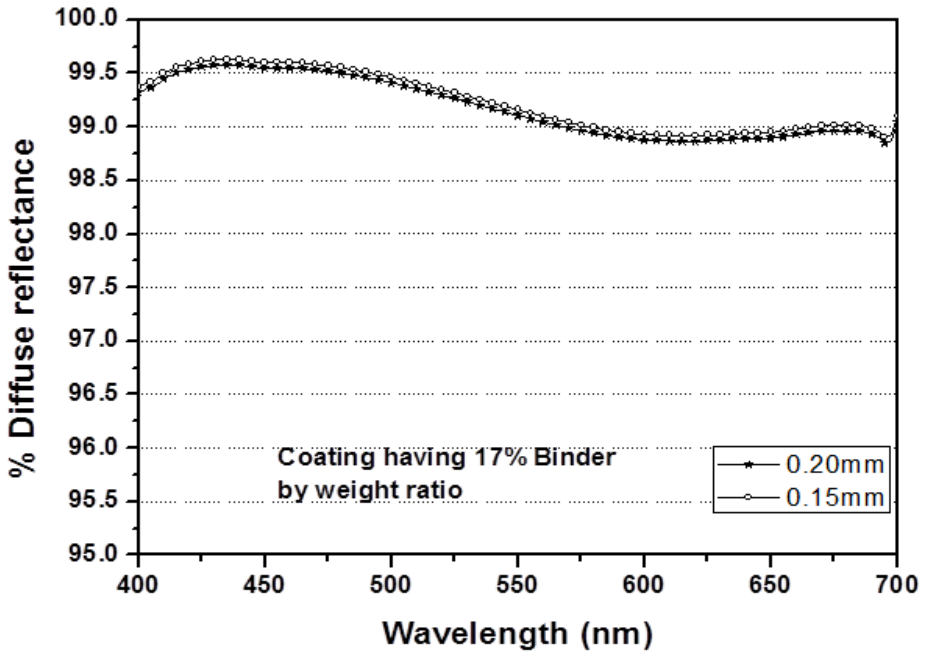

Figure 4.35 Diffuse reflectance spectra of the developed reflectors (aluminium as substrate) having different coating thicknesses

The thickness of a coating is an important factor which cannot be overlooked. It affects the overall reflectance, hiding capability, cost, performance and evaluation of the product throughout its life cycle. Fig. 4.35 shows the diffuse reflectance of reflectors coated up to 0.15, and 0.20 mm. It reveals that with the increase in the coating thickness

there is not much increase in the diffuse reflectance. For coating thickness of 0.15 and 0.20 mm, the diffuse reflectance varies respectively from 99.29 - 98.88% and 99.31 - 98.92%, i.e., there is about 0.05% increase in the reflectance, which practically is insignificant and therefore, there is no motivation for going beyond 0.15 mm thickness. From the present experimental studies, it has also been found that the coating thickness less than 0.15 mm can hardly hide the surface of aluminium sheet. Therefore, we can conclude, as per our findings, 0.15 mm thickness is the optimum one.

In general, with increase in the coating thickness, the reflectance increases because greater the film thickness, greater the number of particles on the substrate, which contributes to the higher reflectance. But, there is a particular limit to the concentration of particles in a coating after which there is no increase or little increase in the reflectance (Fig. 4.35). This limit is determined by critical pigment volume concentration (CPVC) (Chapter 1, Section 1.10.3).

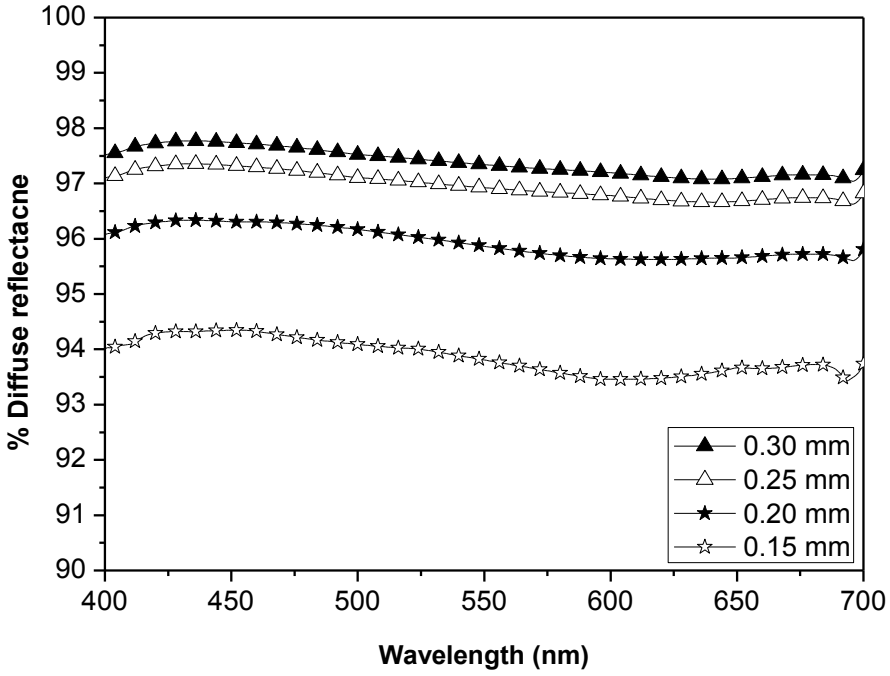

Figure 4.36 Diffuse reflectance spectra of the developed reflectors (plastic as substrate) having different coating thicknesses

Fig. 4.36 shows the diffuse reflectance of the reflectors (plastic as substrate) with various coating thicknesses. The diffuse reflectance has been found to vary from 94.01 - 93.66%, 96.10 - 95.88%, and 97.12 - 96.91%, respectively, for coating thickness 0.15, 0.20, and 0.25 mm showing that the increase in reflectance is due to high coating thickness; as higher the number of nanoparticles on the substrate more the reflectance. With further increase in thickness, i.e., from 0.25 to 0.30 mm, there is practically no change in the reflectance Thus, the coating thickness, 0.25 mm, has been found to be the optimum one. At the optimum coating thickness, the critical volume pigment concentration plays an important role in determining reflectance.

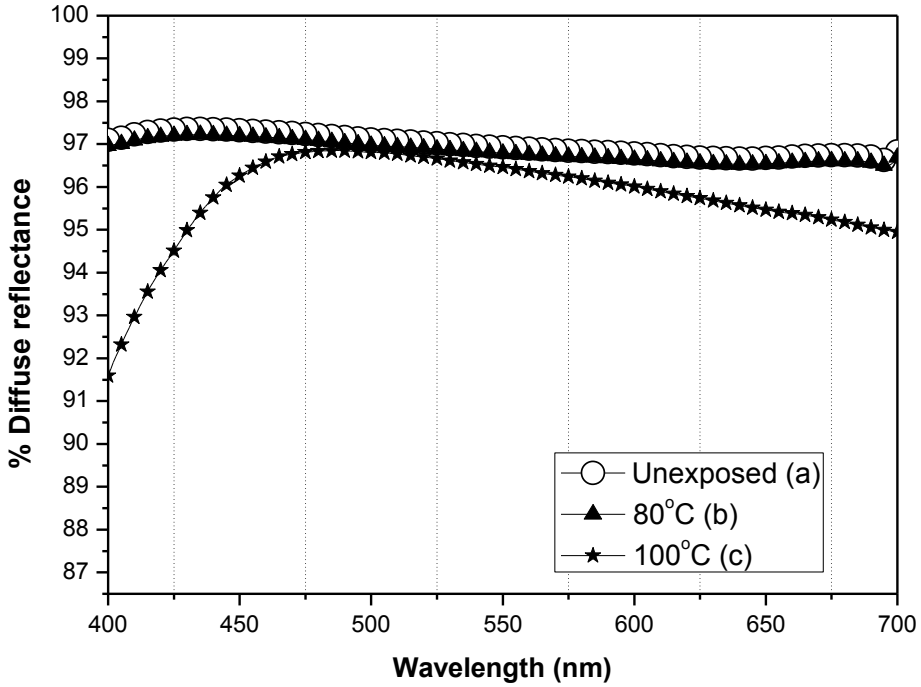

Figure 4.37 Diffuse reflectance spectra of the developed reflectors (aluminium as substrate) exposed to different temperature

Fig. 4.37 shows the diffuse reflectance of reflectors (aluminium as substrate) which have been heated respectively at 80^{o}C and 100^{o}C for 50 hour to check the durability of the coating. As observed form the spectra, there have been no change in diffuse reflectance on heating the reflector at 80^{o}C. However, on heating the reflector at 100^{o}C, a decrease from 97.26% to 91.58% (about 6%) in the reflectance has been observed at about 400 nm region, whereas reflectance for the other wavelengths have been altered by about 3%. The initial effect is usually caused by degradation of the binder on exposure to temperature. Depending upon the binder and particular application, this temperature range can be optimized.

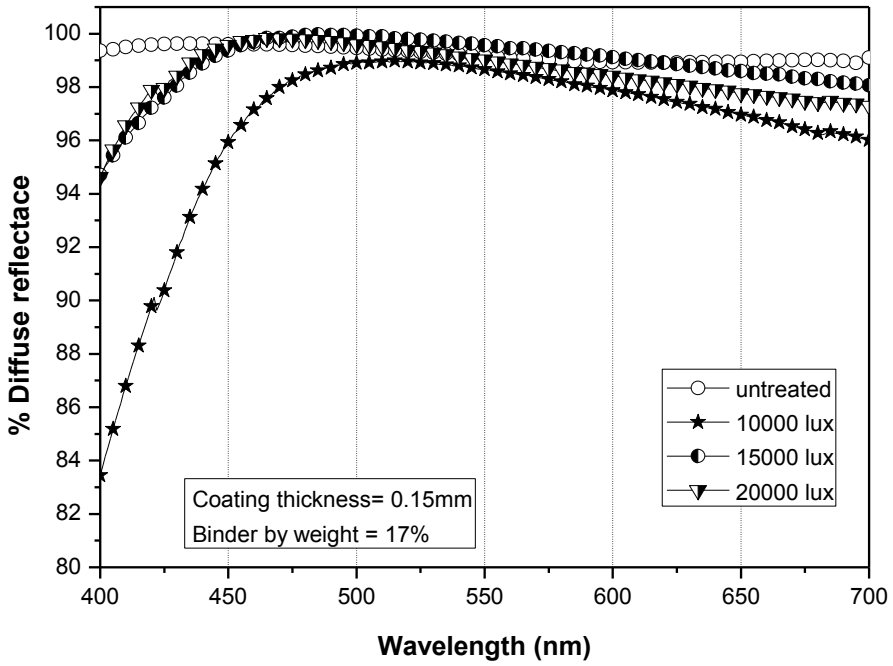

Figure 4.38 Diffuse reflectance spectra of the developed reflectors (aluminium as substrate) exposed to light of different lux

Fig. 4.38 and Table 4.10 show diffuse reflectance of various reflectors (aluminium as substrate) under different illumination conditions. In the case of exposure up to 15,000 lux, the diffuse reflectance has been found to decrease by about 5% in the range of 400 - 450 nm, and 450 nm onwards, it falls hardly by 3%. On the other hand, when the reflectors are exposed to 20,000 lux, the decrease is more than 15% in the range 400 - 500 nm, and in 500 - 700 nm region shows a fall of about 4%. Thus, the diffuse reflectance decreases faster near the lower wavelength end and this fall multiplies on increasing illumination. The reflectors can be said to be stable from 450 nm onwards, in the visible spectrum, when exposed to different levels of illumination.

This drastic decrease, in case of 20,000 lux exposure, might be due to the generation of surface defects in TiO_2 nanoparticles and degradation of the binder caused by strong illumination [155, 156].

Table 4.10 Diffuse reflectance spectra of the developed reflectors exposed to light of different lux.

Sr. No.	**Light illumination (lux)**	**% Diffuse reflectance at wavelength (nm)**					
		400	425	450	500	600	700
1	Unexposed	99.29	99.61	99.60	99.46	98.93	98.88
2	10,000	94.70	97.61	99.36	99.92	99.11	98.06
3	15,000	94.63	97.97	99.58	99.60	98.41	97.29
4	20,000	83.45	90.37	95.93	98.91	97.88	96.02

Flexibility and thermal stability of the coating has been checked to ensure the durability of the reflector (Plastic as substrate). The flexibility of the coating has been checked by changing the working temperature from 30 to 45^{o}C, which showed, respectively, 5.0% and 10% decrease in the substrate surface area without any crack or split being developed in the coating. And on heating at 50^{o}C, the coating developed crack. Thus, the developed reflectors have been found to be flexible and thermally stable up to 45^{o}C.

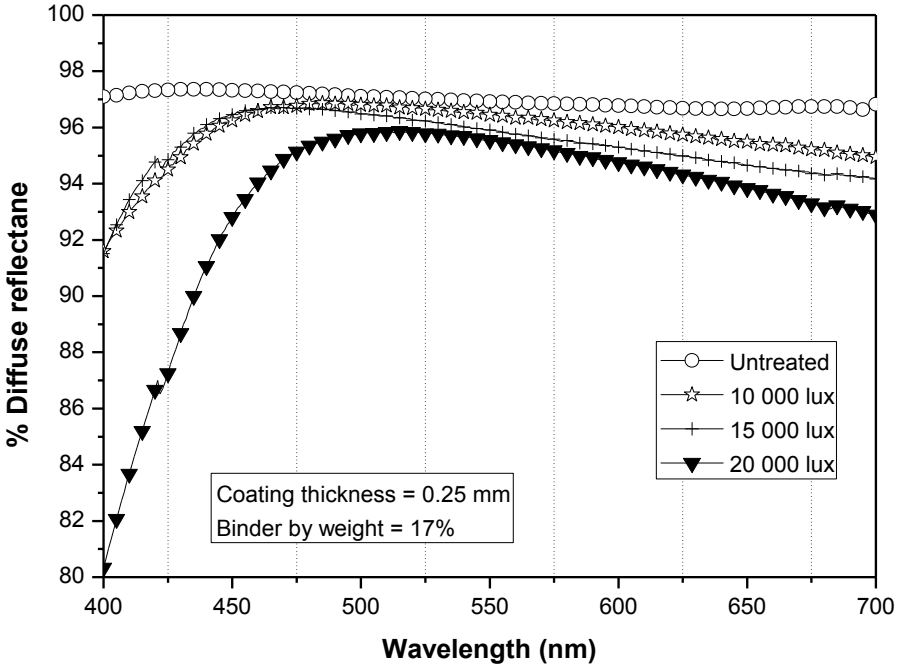

Figure 4.39 Diffuse reflectance spectra of the developed reflectors (plastic as substrate) exposed to light of different lux

Fig. 4.39 show diffuse reflectance of different reflectors (plastic as substrate) under different illumination conditions. In case of exposure up to 15,000 lux, the diffuse reflectance has been found to decrease by about 6% in the range of 400 - 450 nm, and 450 nm onwards, it falls hardly by 3%. On the other hand, when the reflectors are exposed to 20,000 lux, the decrease is more than 18% in the range 400 - 500 nm, and in 500 - 700 nm range, shows a fall of about 4%. Thus, the diffuse reflectance decreases faster near the lower wavelength end and this fall multiplies on increasing illumination. The reflectors can be said to be stable from 450 nm onwards, in the visible spectrum, when exposed to different levels of illumination.

Table 4.11 shows the comparison of different properties of reflectors developed with aluminium and plastic substrate using TiO_2 nanoparticle-based coatings. With aluminium substrate, the reflectors show more than 98% diffuse reflectance. Further, it has been observed that on changing the substrate from aluminium to plastic, the diffuse reflectance decreases about 2% and optical stability do not show any appreciable change. The reflectors with aluminium substrate have been found to be thermally stable up to 80^{o}C and those with plastic substrate, only up to 45^{o}C.

Table 4.11 Comparison of different properties of reflector developed with aluminium and plastic substrate using TiO_2 nanoparticle-based coating

Property	Aluminium substrate	Plastic substrate
Optimum coating thickness (mm)	0.15	0.25
Optimum pigment to binder ratio	17	17
Maximum diffuse reflectance	99.29 - 98.88%	97.12 – 96.91%
Thermal stability (^{o}C)	80	45
Optical stability (lux)	15,000	15,000

As observed form the Table 4.11, for the TiO_2 nanoparticle-based coating material, optimum coating thickness, optimum pigment to binder ratio and optical stability is found to be same for both the substrates, however thermal stability is found to different.

Chapter 5

Conclusions

This Chapter deals with the overall views and winding up of the output of the research work. The research work done has been divided into three main parts: 1. Synthesis and characterization of ZnS and TiO_2 nanoparticles; 2. Preparation of coating materials from the synthesized nanoparticles; 3. Development of reflectors and measurement of their diffuse reflectance.

1. ZnS and TiO_2 nanoparticles were successfully synthesized respectively using chemical precipitation technique and sol-gel technique. Both of these techniques have given reproducible results and homogeneous products. From the industrial point of view, these techniques are simple, give high yield and require low working temperature.

    - Morphological characterization of ZnS nanoparticles reveals that ZnS particles having size 15 - 30 nm and made up of primary crystallites of about 15 - 18 nm. With the help of optical absorption spectra, the band gap of uncapped and thioglycerol capped ZnS nanoparticles have been found to be in the range of 3.74 - 4.05 eV. Surface passivation of ZnS by surfactant molecules has been studied using FTIR, which reveals that thioglycerol is bound electrostatically to the surface of zinc atoms without any formation of covalent thiol bonds. PL spectra of ZnS nanoparticles recorded at room temperature depict broad blue emission peak centered at ~ 426 nm. That the capping affects the reflective propertied of ZnS nanoparticles has been ascertained using the diffuse reflectance study. On comparing the diffuse reflectance of thiophenol, mercaptoethanol and thioglycerol capped ZnS nanoparticles, the 0.50% thioglycerol capped ZnS nanoparticles has been found to show the maximum diffuse reflectance (92.16 - 100%); moreover,

these nanoparticles show enhanced reflectance as compared to uncapped (85 - 95%) and bulk (82 - 70%) particles in the visible region.

- XRD study of synthesized TiO_2 nanoparticles, calcined at different temperatures, reveals the formation of different phases. Crystallite size, calculated from XRD patterns, has been found to be in the range of 29 - 78 nm, which is in good agreement with the particle size calculated from the TEM images. With increase in the calcination temperature from 350 - 900^oC, the band gap value decreases from 3.42 - 3.14 eV. PL spectra of TiO_2 nanoparticles calcined at different temperatures (350 - 900°C) show a broad luminescent peak at ~ 431 nm. The diffuse reflectance study establishes that the ratio of H_2O/MO (L value) affects the reflective properties of TiO_2 nanoparticles. The rutile-phase TiO_2 nanoparticles, with L value 40, show maximum diffuse reflectance, 99.50 - 99.60%.

  To sum up the above, ZnS nanoparticles capped with 0.5 % of thioglycerol and TiO_2 nanoparticles having rutile-phase (L= 40) show diffuse reflectance, respectively 92.16 - 100% and 99.50 - 99.60%, which are much higher than their bulk counterparts. This increase in reflectance is precisely because of the fact that the reduction of particle size to nanoscale increases their band gap. Their reflectance has been found to be further enhanced on controlling: first, the particle size, second, their uniformity, and finally their shape and mono-dispersity.

2. These nanoparticles have been used to develop highly reflecting coatings. The coating materials were prepared using the nanoparticles by optimizing their various parameters such as pigment to binder ratio, pH, and pigment to solvent ratio.

- The concentration of the binder was varied in order to study its effect on the reflectance spectra of the coatings. The binder amount was adjusted so as not to affect the thermal properties of the reflective coatings.
- The preparation process of the coating material reveals that pH affects the wetability of the coating material; for better adhesion of the coating material to the substrate, mechanical sanding of substrates plays an important role.

3. Reflectors were developed by applying these coating materials separately to aluminium and plastic substrates with different coating thicknesses and different pigment to binder ratio. On optimizing the pigment to binder ratio, it was observed that with higher binder concentration, there results a strong capillary action between the binder particles causing them to fuse together and bind the nanoparticles into a continuous film. In general, aluminium is used as a substrate for the development of reflectors.

   - A comparison of different properties of the reflectors developed with aluminium and plastic substrates using ZnS and TiO_2 nanoparticle-based coating was done. And, it was found that the ZnS based reflectors have diffuse reflectance 97 - 100% (for aluminium substrate) and 96.50 - 97.50 % (for plastic substrate), and, the TiO_2 based reflectors, 99.29 - 98.88 % (for aluminium substrate) and 97.12 - 96.91 % (for plastic substrate). Switching the aluminium substrate with the plastic one, no appreciable change in the diffuse reflectance and the optical stability has been noticed. Further, the aluminium substrate has been found to be thermally more stable (up to 80^oC) than the plastic substrate (up to 45^oC).
   - For the given coating material, optimum pigment to binder ratio is found to be same for both the substrates, which is due to the uniform morphology of the nanoparticles and the adjustment of pH of the coating materials;
   - Using both the substrates, the optimum coating thickness for ZnS nanoparticle-based reflectors has been found to be the same. In case of TiO_2 nanoparticle-based

reflectors, the coating thickness, as compared to ZnS, is different for different substrates.

- For a given substrate, the thermal stability is found to be same for both the coating materials. In the aluminium based reflectors, binder degradation was observed after 80^{o}C; however, no change in the surface area of the substrate was observed. In case of plastic based reflectors, large change in the surface area (>10%) has been observed on heating them to 45^{o}C and, beyond which they were found to develop cracks.
- For same coating material and different substrates, the optical stability has been observed to be same. Optical stability depends up on the properties of synthesized nanoparticles as well as the binder. On illuminating the ZnS and TiO_2 based reflectors, the reflectance has been observed to show degradation respectively after 10,000 and 15,000 lux, due to the generation of surface defects.

The reflectors (for visible region) developed with ZnS nanoparticle-based coatings have been found to be unique in the sense that no work has ever been reported for the development of such reflectors using nano-particle-based or bulk particle-based coatings. Under the present research work, the reflectors developed using TiO_2 nanoparticle-based coatings have been found to register much higher diffuse reflectance than those reported earlier using bulk TiO_2 particle-based coatings.

Chapter 6

Future work

The surface science of ZnS and TiO_2 nanoparticles and their coatings is an emerging field with a rapidly increasing interest towards enhancing their reflectivity. In future, work can be carried out to synthesize and study the reflective properties of hollow and core-shell ZnS and TiO_2 nanoparticles as well as their reflective coatings. It is the multiple reflections from hollow and core-shell nanoparticles that will enhance their reflectivity.

Further work can be carried out to improve the efficiency of luminaries which is expressed in terms of Light Output Ratio (LOR). The LOR is the measure of the quantity of light which is emitted from the luminaire, as compared to the quantity of light generated by the lamp, which is mainly dependent on the design of the luminaire. It involves the application of ZnS and TiO_2 nanoparticle-based high reflective coatings as well as improving the design of luminaire.

Another, parameter that can be studied in future is the durability of coating which includes effect of temperature, illumination, weather conditions, self cleaning etc.

References

1. Hosokawa M, Nogi K, Naito, Yokoyama, "Nanoparticle technology handbook", Elsevier, UK (2010).
2. Fang Y, Agrawala D, Skandan G, Jain M, "Fabrication of translucent MgO ceramics using nanopowders", Materials Letters, 58 p.551 (2004).
3. Sharma JP, Sekhon SS, "Relative role of plasticizer and nano size fumed silica on the conductivity behaviour of PEO-NH_4PF_6 polymer electrolytes", Indian Journal of Engineering & Materials Sciences, 12 p.557 (2005).
4. Naidu V, Kumar MA, Ahamed SKA, Prakash C, "Mg Sm Ferrite for Nano structured E-Shaped Patch Antenna studies", International Journal of Computer Applications, 30 p.45 (2011).
5. Jeong DY, Lee Sh, Song HC, Choi KH, Cho JH, "Hydrothermal synthesis and microwave sintering of $(K_{0.5}Na_{0.5})NbO_3$ ceramics", Journal of the Korean Physical Society, 58 p.663 (2011).
6. Kopelman R, Clark H, Barker S, "Optical sensor for the detection of nitric oxide", US Patent No. 6 636 652 B1 (2003).
7. Beausoleil RG, Kuekes PJ, Williams RS, "Autonomous evanescent optical nanosensor", US Patent No. 7 233 711 B1 (2007).
8. Lieber CM, H. Park H, Wei Q, Cui Y, "Nanosensors", US Patent No.7 256 652 B2 (2007).
9. O'Connell DG, "Cell tray", US Patent No. 7 190 449 B2 (2007).
10. O'Connell DG, O'Connell-Rodwell C, "Precision optical interacellular near field imaging/spectroscopy technology", US Patent No. 7 129 454 B2 (2006).
11. Hearley AK, Redmond SD, "Solid-state hydrogen storage systems", US Patent No. 7 279 222 B2 (2007).

12. Majumdar A, Shakouri A, Sands TD, Yang P, Mao SS, Russo RE, Fieck H, Weber ER, Kind H, Haung M, Yan H, Wu Y, Fan R, "Nanowires, nanostructures and devices fabricated therefrom", US Patent No. 6 888 205 B2 (2005).
13. Allhoff F, Lin P, Moore D, "What is nanotechnology and why does it matter", 3rd ed., John Wiley & Sons, Ltd. (2010).
14. Yeo LY, Friend JR, "Electrospinning carbon nanotube polymer composite nanofibers", Journal of Experimental Nanoscience, 1 p.177 (2006).
15. Lu Y, Zhang Z, Emanetoglu NW, Inouye M, Mircochnitchenko O, "Multifunctional biosensors based on ZnO nanostructures", US Patent No. 6 914 279 B2l (2005).
16. Moore M, Glattly J, Mcnally WF, Summit C, "Bandage with a hydrophilic form containing silver and a hemastatic agent", US Patent No. 0 228 123 A1 (2008).
17. http://www.understandingnano.com/batteries.html
18. http://www.understandingnano.com/sensor.html
19. Ramer DP, Watson HE, Ritter MP, Ezling BL, Schmitt MG, Rains JC, "Apparatus for projecting electromagnetic radiation with a tailored intensity distribution", US Patent No. 5 967 652 (1999).
20. Brown M, "High reflective paint for high-intensity optical applications", US Patent No. 6 974 498 B2 (2005).
21. http://nzic.org.nz/ChemProcesses/polymers/10D.pdf
22. http://www.coastalclassiccreations.com/index.php?option=com_content&view=article&id=29&Itemid=83
23. Talbert R, "Paint Technology Handbook", Taylor & Francis Group, USA (2008).
24. http://www.makepaint.tk/2009/03/resin-binder.html

25. Abelli M, Bastiani FD, Romagnoli, “Reflective paint and a method for its use”, US Patent No. 0 013 900 A1 (2004).
26. http://www.makepaint.tk/2009/07/solvents.html
27. Brock T, Groteklaes M, Mischke P “European coatings handbook”, Th. Schager, hannove, Germany (2000).
28. http://www.makepaint.tk/2009/07/additives-paint-component.html
29. http://www.makepaint.tk/2009/07/extenders.html
30. http://physics.wikia.com/wiki/Reflection
31. http://www.trfic.msu.edu/data_portal/Landsat7doc/landsatch6.html
32. http://knol.google.com/k/lighting-and-its-measurement#
33. http://www.siggraph.org/education/materials/HyperGraph/illumin/diffuse_reflection.html
34. Fleming RJ, McGrath JM, Lyons CS, “Retroreflective articles having polymer multilayer reflective coatings”, US Patent No. 6 243 201 B1 (2001).
35. Philips ED, “Reboundable optical structure”, US Patent No. 0 220 217 A1 (2008).
36. Smith ML, Holzrichter EJ, Lewarchik RJ, “Hard, flexible, and durable architectural coating”, US Patent No. 5 262 494 (1993).
37. Kohta S, Sugiyama Y, “Light reflective material”, US Patent No. 5 991 080 (1999).
38. http://www.naturalpigments.com/education/article.asp?ArticleID=8
39. Buxbaum G, Pfaff G, “Industrial Inorganic Pigments”, Wiley-VCH, Strauss GmbH, Morlenbach (2005).
40. http://hyperphysics.phy-astr.gsu.edu/hbase/atmos/blusky.html
41. Harlan AD, Eide AC, “Effect of particle shape of white pigments on opacity, acicular zinc sulfide in the form of wurtzite”, Industrial And Engineering Chemistry, 32 p.537 (1940).

42. http://www.specialchem4coatings.com/tc/color-handbook/index.aspx?id=opacity
43. Dubs CW, “High reflectance coatings”, IEEE Transactions on Nuclear Science, p.729 (1966).
44. http://goliath.ecnext.com/coms2/gi_0199-3893581/Critical-Pigment-Volume-Concentration-measurements.html
45. http://www.thefreelibrary.com/Critical+Pigment+Volume+Concentration+measurements+...+a+very+fast...-a0130971554
46. http://findarticles.com/p/articles/mi_hb3226/is_14_2/ai_n29168133/
47. http://esonn.fr/esonn2010/xlectures/mangematin/Nano_Green_Building55ex.pdf
48. Karvinen SM, “The effects of trace element doping on the optical properties and photocatalytic activity of nanostructured titanium dioxide”, Industrial & Engineering Chemistry Research, 42 p.1035 (2003).
49. Macwan DP, Dave PN, Chaturvedi S, “A review on nano tio_2 sol gel type syntheses and its applications”, Journal of Materials Science, 46 p.3669 (2011).
50. Chen X, Mao SS, “Titanium dioxide nanomaterials: synthesis, properties, modifications, and applications”, Chemical Reviews, 107 p.2891 (2007).
51. Saravanan N, Teh GB, Yap SYP, Cheong KM, “Simple synthesis of ZnS nanoparticles in alkaline medium”, Journal of Materials Science: Materials in Electronics, 19 p.1206 (2008).
52. Pawar MJ, Nimkar SD, Nannukar PP, Tale AS, Deshmukh SB, Chaure SS, “Effect of Sn^{2+} doping on optical properties of thiourea capped ZnS nanoparticles”, Chalcogenide Letters, 7 p.139 (2010).
53. Das K, Sharma SN, Kumar M, De SK, “Morphology dependent luminescence properties of Co doped TiO_2 nanostructures”, The Journal of Physical Chemistry C, 113 p.14783 (2009).

54. Peng WQ, Qu SC, Cong GW, Wang ZG, “Synthesis and structures of morphology-controlled ZnO nano and microcrystals”, Crystal Growth & Design, 6 p.1518 (2006).
55. http://www.chm.davidson.edu/vce/crystals/ZincBlende.html
56. http://www.chm.davidson.edu/vce/crystals/ZincBlende.html
57. Akizuki M, “Slip structure of heated sphalerite”, The American Mineralogist, 55 p.1302 (1970).
58. http://www.ilpi.com/inorganic/structures/zincblende/
59. http://cnx.org/content/m16927/latest/
60. Kumar S, Verma NK, Singla ML, “Reflective properties of ZnS nanoparticle coatings”, Journal of Coating Technology and Research, 8 p.223 (2011).
61. Eastaugh N, Walsh V, Chaplin T, Siddall R, “The Pigment Compendium”, Elsevier Butterworth-Heinemann, Burlington (2004).
62. Heaton N, “Outlines of Paint Technology”, Charles Griffin & Co., London (1928).
63. Buxbaum, “Industrial Inorganic Pigments Buxbaum”, Wiley-VCH, USA (1998).
64. Diebold U, “Structure and properties of TiO_2 surfaces: a brief review”, Applied Physics A, 76 p.681 (2003).
65. Edwards HGM, Hassan NFK, Middleton PS, “Anatase- a pigment in ancient artwork or a modern usurper?”, Analytical and Bioanalytical Chemistry, 384 p.1356 (2006).
66. Dorian AHH, Charles CS, “Review of the anatase to rutile phase transformation”, Journal of Materials Science, 46 p.855 (2011).
67. Baiju KV, Shukla S, Sandhya KS, James J, Warrier KGK, “Photocatalytic activity of Sol-gel derived nanocrystalline titania”, The Journal of Physical Chemistry C, 111 p.7612 (2007).

68. Murrray JL, Wriedy HA, “The O-Ti (Oxygen –Titanium) system”, Bulletin of Alloy Phase Diagrams, 8 p.148 (1987).

69. Muscat J, Swamy V, Harrison NM, “First-principles calculations of the phase stability of TiO_2” Physical Review B, 65 p.224112 (2002).

70. Bandas C, Lazau C, Dabici A, Sfarloaga P, Vaszilcsin N, Tiponut V, Grozescu I, “Structural and morphological characterization of nanosized TiO_2 particles prepared by sol-gel method”, Journal of Optoelectronics and Advanced Materials, 13 p.399 (2011).

71. Tejos M, Buono-cuore GE, Diaz FR, Delvalle MA, Palomares J, “Direct photodeposition of nanostructured tio_2 thin films from b-diketonate complexes, and their photocatalytic behaviour”, Journal of the Chilean Chemical Society, 49 p.297 (2004).

72. http://www.chm.davidson.edu/vce/crystals/Rutile.html

73. Miessler G, Tarr D, “Inorganic Chemistry”, 3rd ed., Pearson Educatiion, Inc., USA (2008).

74. Mo SD, Ching WY, “Electronic and optical properties of three phases of titanium dioxide: Rutile, anatase, and brookite”, Physical Review B, 51 p.13023 (1995).

75. Ray AK, Tracey SM, McQuillin B, Hodgson SNB, “Optical studies on sol-gel derived titanium dioxide films”, IEE Proceedings - Science, Measurement and Technology, 147 p.301 (2000).

76. Tayade RJ, Surolia PK, Kulkarni RG, Jasra RV, “Photocatalytic degradation of dyes and organic contaminants in water using nanocrystalline anatase and rutile TiO_2”, Science and Technology of Advance Materials, 8 p.455 (2007).

77. Pedraza-Avella JA, Lopez R, Martinez-Ortega F, Paez-Mozo EA, Gomez R, “Effect of chromium doping on visible light absorption of nanosized titania sol-gel”, Journal of Nanoparticle Research, 5 p.95 (2009).

78. Kampfer WA, “Titanium Dioxide Pigment Handbook”, John Wiley, New York (1973).
79. http://serc.carleton.edu/research_education/geochemsheets/BraggsLaw.html
80. http://xrayweb.chem.ou.edu/notes/crystallography.html
81. http://www.bccmeteorites.com/XRD.PDF
82. http://www.mf.mpg.de/de/abteilungen/mittemeijer/english/commentary/Powder%20Diffraction%20in%20Mat.Sci.pdf
83. http://www.kstreetstudio.com/science/experiments/files/XRD-CSize1.pdf
84. He BB, “Two-dimensional X-ray diffraction”, John Wiley & Sons, Inc., New Jersey (2009).
85. Clearfield A, Reibenspies JH, Bhuvanesh N, “Principles and applications of powder diffraction”, John Wiley & Sons, Inc., USA (2008).
86. Grzmil B, Rabe M, Kic B, Lubkowski K, “Influence of phosphate, potassium, lithium, and aluminium on the anatase-rutile phase transformation”, Industrial & Engineering Chemistry Research, 46 p.1018 (2007).
87. http://www.xray.cz/xray/csca/kol2011/kurs/Dalsi-cteni/Connolly-2005/07-Errors-Sample-Prep.pdf
88. Leng Y, “Materials characterization introduction to microscopic and spectroscopic methods”, John Wiley & Sons, Inc., Singapore (2008).
89. Chattopadhyay KK, Banerjee AN, “Introduction to nanoscience and nanotechnology”, PHI Lerning Private Limited, New Delhi (2009).
90. Gabriel BL, “SEM: A user’s manual for materials science”, ASTM, USA (1985).
91. Echlin P, “Handbook of sample preparation for scanning electron microscopy and x-ray microanalysis”, Springer, UK (2009).
92. Williams DB, Carter CB, “Transmission electron microscopy a textbook for materials science”, Springer, USA (2009).

93. Reimer L, Kohl H, "Transmission electron microscopy physics of image formation", 5th ed., Springer, USA (2008).

94. Ayache J, Beaunier L, Boumendil J, Ehret G, Laub D, "Sample preparation handbook for transmission electron microscopy", Springer, New York (2010).

95. Rao DVS, Muraleedharan K, Humphreys CJ, "TEM specimen preparation techniques", Microscopy: Science, Technology, Applications and Education, A. Méndez-Vilas and J. Díaz, p.1232 (2010).

96. http://www.camo.com/rt/Resources/spectroscopy.html

97. http://www.siliconfareast.com/FTIR.htm

98. Christy AA, Ozaki Y, Gregoriou VG, "Modern Fourier Transform Infrared Spectroscopy", Elsevier, Netherlands (2001).

99. http://inventors.about.com/od/pstartinventions/a/Photoluminescen.htm

100. http://web.viu.ca/gill/uploads/Chem%20312/Chem%20312%20L11a%20Photoluminescence%20spectroscopy.pdf

101. http://www.harpercollege.edu/tm-ps/chm/100/dgodambe/thedisk/labtech/spec20.htm

102. http://www2.chemistry.msu.edu/faculty/reusch/VirtTxtJml/Spectrpy/UV-Vis/uvspec.htm

103. Upstone SL, "Ultraviolet/Visible Light Absorption Spectrophotometry in Clinical Chemistry", Encyclopedia of Analytical Chemistry, John Wiley & Sons Ltd, Chichester (2000).

104. Ubale AU, Sangawar VS, Kulkarni DK, ''Size dependent optical characteristics of chemically deposited nanostructured ZnS thin films.'' Bulletin of Material Science, 30 p.147 (2007).

105. Kar S, Chaudhuri S, "Synthesis and optical properties of single and bicrystalline ZnS nanoribbons", Chemical Physics Letters, 414 p.40 (2005).

106. http://www.uco.es/organiza/departamentos/decraf/pdf-edaf/DRS08.pdf

107. http://www.physics.hku.hk/~phys2227/file/Chap%202new.pdf

108. http://www.specac.com/userfiles/file/ReflectanceSpectroscopy.pdf

109. http://www.labsphere.com/data/userFiles/A Guide to Reflectance Coatings and Materials.pdf

110. Wu J, Shen W, Li H, Liu X, Gu P, "ZnS-Ag color filters for white LED display", Chinese Optics Letters 8 p.32 (2010).

111. Lu C, Cui Z, Li Z, Yang B, Shen J, "High refractive index thin films of ZnS/polythiourethane nanocomposites" Journal of Material Chemistry, 13 p.526 (2003).

112. Lee EE, Gunzburg MJ, Nguyen TL, Howlett GJ, Rothacker J, Nice EC, Ckayton HA, Mulvaney P, "Experimental determination of quantum dot size distributions, ligand packing densities, and bioconjugation using analytical ultracentrifugation", Nano Letters, 8 p.2883 (2008).

113. Li Y, Feng J, Daniels S, Pickett NL, O'Brien P, "A highly luminescent ZnS/CdSe/ZnS nanocrystals-tetrapeptide biolabeling agent", Journal of Nanoscience and Nanotechnology, 7 p.2301 (2007).

114. Mehta SK, Kumar S, Chaudhary S, Bhasin KK, Gradzielski M, "Evaluation of ZnS nanoparticles via facile CTAB aqueous micellar solutions route: A study on controlling parameter", Nanoscale Research Letter, 4 p.17 (2009).

115. Niasari MS, Davar F, Mazaheri M, "Synthesis and characterization of ZnS nanoclusters via hydrothermal processing from [bis(salicylidene)zinc(II)]", Journal of Alloys and Compounds, 470 p.502 (2009).

116. Anil MP, Shivram SG, "Preparation of zinc sulfide nanocrystallites from single-molecule precursors", Journal of Crystal Growth, 326 p.157 (2011).

117. Huang FH, Peng YR, Lin CF, "Synthesis and characterization of ZnS: Ag nanocrystals surface-capped with thiourea", Chemical Research in Chinese Universities, 22 p.675 (2011).

118. Maitya R, Maitia UN, Mitrab MK, Chattopadhyaya KK, "Synthesis and optical characterization of polymer-capped nanocrystalline ZnS thin films by chemical process", Physica E, 33 p.104 (2006).

119. Yang J, Peng JJ, Zou R, Peng F, Wang H, Yu H, Lee JY, "Mesoporous zinc-blende ZnS nanoparticles: synthesis, characterization and superior photocatalytic properties", Nanotechnoogy, 19 p.255603 (2008).

120. Rathore KS, Patidar D, Janu Y, Saxena NS, Sharma K, "Structural and optical charcterization of chemically synthesized ZnS nanoparticles," Chalcozenide letters, 5 p.105 (2008).

121. Mahamuni S, Khosravi AA, Kundu M, Kshirsagar A, Bedekar A, Avasare DB, Singh P, Kulkarni SK, "Thiophenol-capped ZnS quantum dots", Journal of Applied Physics, 73 p.5237 (2009).

122. Manzoor K, Vadera SR, Kumar N, Kutty TRN, "Energy transfer from organic surface adsorbate-polyvinyl pyrrolidone molecules to luminescent centers in ZnS nanocrystals", Solid state Communications, 129 p.469 (2004).

123. Sharma R, Chandra BP, Bisen DP, "Effect of molar concentration on optical absorption spectra of ZnS:Mn nanoparticles", E-Journal of Chemistry, 7 p.S23 (2008).

124. Sharma M, Kumar S, Pandey OP, "Study of energy transfer from capping agents to intrinsic vacancies/defects in passivated ZnS nanoparticles", Journal of Nanoparticle Research, 12 p.2666 (2010).

125. http://www.stormwaterbook.com/images/chapter8.pdf

126. Burda C, Chen X, Narayanan R, El-Shayed MA, "Chemistry and properties of nanocrystals of different shapes", Chemical Reviews, 105 p.1025 (2005).

127. http://en.wikademia.org/Precipitation_%28chemistry%29

128. Yao JH, Laradji M, "Dynamic of Ostwald ripening in the presence of surfactants", Physical review E, 47 p.2695 (1992).

129. Sattler KD, “Handbook of nanophysics: nanoparticles and quantum dots”, Taylor & Francis Group, USA (2011).

130. http://hdl.handle.net/10530/816

131. Houghton RP, “Metal complexes in organic chemistry”, Cambridge University Press (1979).

132. Cheng H, Ma J, Zhao Z, Qi L, “Hydrothermal preparation of uniform nanosized rutile and anatase particles”, Chemistry of Materials, 7 p.663 (1995).

133. Kumar KNP, Keizer K, Burggraaf AJ, Okubo T, Nagamoto H, “Synthesis and textural properties of unsupported and supported rutile (TiO_2) membranes”, Journal of Materials Chemistry, 3 p.923 (1993).

134. Courtecuisse VG, Chhor K, Bocquet JF, Pommier C, “Kinetic of the titanium isopropoxide decomposition in supercritical isopropyl alcohol”, Industrial & Engineering Chemistry Research, 35 p.2539 (1996).

135. Xia B, Li W, Zhang B, Xie Y, “Low temperature vapor-phase preparation of TiO2 nanopowders”, Journal of Materials Science, 34 p.3505 (1999).

136. Anuradha TV, Ranganathan S, “Nanocrystalline TiO_2 by three different synthetic approaches: A comparison”, Bulletin of Materials Science, 30 p.263 (2007).

137. Deorsola FA, Vallauri D, “Synthesis of TiO_2 nanoparticles through the gel combustion process”, Journal of Materials Science, 43 p.3274 (2008).

138. Ross WD, “Theoretical light-scattering power of TiO_2 microvoids”, Industrial & Engineering Chemistry Product Research and Development, 13 p.45 (1974).

139. http://naturalpigments.com/education/article.asp?ArticleID=5

140. Prasad K, Pinjari DV, Pandit AB, Mhaske ST, “Phase transformation of nanostructured titanium dioxide from anatase-to-rutile via combined ultrasound assisted sol-gel technique”, Ultrasonics Sonochemistry, 17 p.409 (2010).

141. Tracton AA, “Coating Materials and Surface coatings”, Taylor & Francis Group, USA (2007).

142. Kour R, Verma NK, Chakarvarti SK, "Morphological, structural and optical characterization of nickel nanostructures", Journal of materials Science, 42 p.5629 (2007).

143. Nguyen TT, Trinh XA, Nguyen LH, Pham TH, "Photoluminescence characteristics of as-synthesized and annealed ZnS:Cu,Al nanocrystals", Advances in Natural Sciences: Nanoscience and Nanotechnology, 2 p.035008 (2011).

144. Sartale SD, Sankapal BR, Steiner ML, Ennaoui A, "Preparation of nanocrystalline ZnS by a new chemical bath deposition route", Thin Solid Films, 480-481p.168 (2005).

145. Reiss P, Protiere M, Li L, "Core/shell semiconductor nanocrystals", Small, 5 p.154 (2009).

146. Silverstein RM, Basslwe RC, Morrill TC, "Spectrometric identification of organic compounds", 5th ed., John Willey & Sons, Singapore (1991).

147. Gilbert B, Huang F, Lin Z, Goodell C, Zhang H, Banfield JF, "Special phase transformation and crystal growth pathways observed in nanoparticles", ACS Nano Letters, 6 p.605 (2006).

148. Borse PH, Deshmukh N, Shinde RF, Date SK, Kulkarni SK, ''Luminescence quenching in ZnS nanoparticles due to Fe and Ni doping'', Journal of Materials Science, 34 p.6087 (1999).

149. Jindal Z, Verma NK, "Photoluminescent properties of ZnS:Mn nanoparticles with in-built surfactant", Journal of Materials Science, 43 p.6539 (2008).

150. Saleh BEA, Teich MC, "Fundamentals of photonics", 2nd ed., John Wiley & Sons, Hoboken, New Jersey (2007).

151. Becker WG, Bard AJ, "Photoluminescence and photoinduced oxygen adsorption of colloidal zinc sulfide dispersions", Journal of Physical Chemistry, 87 p.4888 (1983).

152. Benoit D, Bresse JF, Dack LV, Werner H, Wernisch J, “Microbeam and nanobeam analysis”, Springer, New York (1996).

153. Pedrotti FL, Pedrotti LM, Pedrotti SL, “Introduction to Optics”, 3rd ed., Addison-Wesley, America (2006).

154. Hayes GB, Melnyk TJ, “High reflective polyester coatings”, US Patent No. 7 393 591 B2 (2008).

155. Jaroenworaluck A, Sunsaneeyametha W, Kosachan N, Stevens R, ‘‘Characteristics of silica-coated TiO_2 and its uv absorption for sunscreen cosmetic applications’’, Surface and Interface Analysis, 38 p.473 (2006).

156. Mager M, ‘‘Composition comprising inorganic uv absorbers’’, US Patent No. 6 790 273 (2004).

157. Addamo M, Augugliaro V, Paola AD, Loepez EG, Loddo V, MarcıE G, Molinari R, Palmisano L, Schiavello M, “Preparation, characterization, and photoactivity of polycrystalline nanostructured TiO_2 catalysts”, Journal of Physical Chemistry B, 108 p.3303 (2004).

158. Fox MA, Dulay MT, “Hetrogeneous photocatalysis”, Chemical Reviwes, 93 p.341 (1993).

159. Batzill M, Morales EH, Diebold U, “Influence of nitrogen doping on the defect formation and surface properties of TiO_2 rutile and anatase”, Physical Review Letters, 96 p.26103 (2006).

160. Shannon RD, Pask JA, “Kinetics of the anatase-rutile transformation”, Journal of American Ceramic Society, 48 p.391 (1965).

161. Riyas S, Krishnan G, Mohandas PN, “Anatase–rutile transformation in doped titania under argon and hydrogen atmospheres”, Advancement in Applied Ceramics, 106 p.255 (2007).

162. Syarif DG, Miyashita A, Yamaki T, Sumita T, Choi Y, Itoh H, “Preparation of anatase and rutile thin films by controlling oxygen partial pressure”, Applied Surface Science, 193 p.287 (2002).

163. Matsuyama K, Mishima K, Hayashi K, Matsuyama H, "Microencapsulation of TiO_2 nanoparticles with polymer by rapid expansion of supercritical solution", Journal of Nanoparticle Research, 5 p.87 (2003).

164. Gouma PI, Mills MJ, "Anatase-to-rutile transformation in titania powders", Journal of American Chemical Society, 84 p.619 (2001).

165. Zachariah, Baiju KV, Shukla S, Deepa KS, James J, Warrier KGK, "Synergistic effect in photocatalysis as observed for mixed-phase nanocrystalline titania processed via sol-gel solvent mixing and calcination", Journal of Physical Chemistry C, 112 p.11345 (2008).

166. Cong Y, Zhang J, Chen F, Anpo M, He D "Preparation, photocatalytic activity, and mechanism of nano-TiO_2 co-doped with nitrogenand iron (iii)", Journal of Physical Chemistry C, 111 p.10618 (2007).

167. Yoon M, Seo M, Jeong C, Jang JH, Jeon KS, "Synthesis of liposome-templated titania nanodisks: optical properties and photocatalytic activities", Chemistry of Materials, 17 p.6069 (2005).

168. D. Li, H. Haneda, S. Hishita, N. Ohashi, "Visible-light-driven N−F−codoped TiO_2 photocatalysts. 1. synthesis by spray pyrolysis and surface characterization", Chemistry of Materials, 17 p.2596 (2005).

169. Ullmann F, "Encyclopedia of Industrial Chemistry", Wiley-VCH Verlag GmbH, Weinheim (2002).

170. Zaleska A, "Doped-TiO_2: a review", Recent patents on engineering, 2 p.157 (2008).

171. Sates D, Tracton AA, "Coatings technology handbook", 2nd ed., Marcel Dekker, Inc., New York (2001).